ARTICLES

Evidence for top quark production in $\bar{p}p$ collisions at $\sqrt{s} = 1.8$ TeV

F. Abe,[13] M. G. Albrow,[7] S. R. Amendolia,[23] D. Amidei,[16] J. Antos,[28] C. Anway-Wiese,[4]
G. Apollinari,[26] H. Areti,[7] P. Auchincloss,[25] M. Austern,[14] F. Azfar,[21] P. Azzi,[20] N. Bacchetta,[18]
W. Badgett,[16] M. W. Bailey,[24] J. Bao,[34] P. de Barbaro,[25] A. Barbaro-Galtieri,[14] V. E. Barnes,[24] B. A. Barnett,[12]
P. Bartalini,[23] G. Bauer,[15] T. Baumann,[9] F. Bedeschi,[23] S. Behrends,[2] S. Belforte,[23] G. Bellettini,[23]
J. Bellinger,[33] D. Benjamin,[32] J. Benlloch,[15] J. Bensinger,[2] D. Benton,[21] A. Beretvas,[7] J. P. Berge,[7]
S. Bertolucci,[8] A. Bhatti,[26] K. Biery,[11] M. Binkley,[7] F. Bird,[29] D. Bisello,[20] R. E. Blair,[1]
C. Blocker,[29] A. Bodek,[25] V. Bolognesi,[23] D. Bortoletto,[24] C. Boswell,[12] T. Boulos,[14] G. Brandenburg,[9]
E. Buckley-Geer,[7] H. S. Budd,[25] K. Burkett,[16] G. Busetto,[20] A. Byon-Wagner,[7] K. L. Byrum,[1] C. Campagnari,[7]
M. Campbell,[16] A. Caner,[7] W. Carithers,[14] D. Carlsmith,[33] A. Castro,[20] Y. Cen,[21] F. Cervelli,[23]
J. Chapman,[16] M.-T. Cheng,[28] G. Chiarelli,[8] T. Chikamatsu,[31] S. Cihangir,[7] A. G. Clark,[23] M. Cobal,[23]
M. Contreras,[5] J. Conway,[27] J. Cooper,[7] M. Cordelli,[8] D. P. Coupal,[29] D. Crane,[7] J. D. Cunningham,[2]
T. Daniels,[15] F. DeJongh,[7] S. Delchamps,[7] S. Dell'Agnello,[23] M. Dell'Orso,[23] L. Demortier,[26] B. Denby,[23]
M. Deninno,[3] P. F. Derwent,[16] T. Devlin,[27] M. Dickson,[25] S. Donati,[23] R. B. Drucker,[14] A. Dunn,[16]
K. Einsweiler,[14] J. E. Elias,[7] R. Ely,[14] E. Engels, Jr.,[22] S. Eno,[5] D. Errede,[10] S. Errede,[10]
Q. Fan,[25] B. Farhat,[15] I. Fiori,[3] B. Flaugher,[7] G. W. Foster,[7] M. Franklin,[9] M. Frautschi,[18]
J. Freeman,[7] J. Friedman,[15] H. Frisch,[5] A. Fry,[29] T. A. Fuess,[1] Y. Fukui,[13] S. Funaki,[31]
G. Gagliardi,[23] S. Galeotti,[23] M. Gallinaro,[20] A. F. Garfinkel,[24] S. Geer,[7] D. W. Gerdes,[16] P. Giannetti,[23]
N. Giokaris,[26] P. Giromini,[8] L. Gladney,[21] D. Glenzinski,[12] M. Gold,[18] J. Gonzalez,[21] A. Gordon,[9]
A. T. Goshaw,[6] K. Goulianos,[26] H. Grassmann,[6] A. Grewal,[21] G. Grieco,[23] L. Groer,[27] C. Grosso-Pilcher,[5]
C. Haber,[14] S. R. Hahn,[7] R. Hamilton,[9] R. Handler,[33] R. M. Hans,[34] K. Hara,[31] B. Harral,[21]
R. M. Harris,[7] S. A. Hauger,[6] J. Hauser,[4] C. Hawk,[27] J. Heinrich,[21] D. Hennessy,[6] R. Hollebeek,[21]
L. Holloway,[10] A. Hölscher,[11] S. Hong,[16] G. Houk,[21] P. Hu,[22] B. T. Huffman,[22] R. Hughes,[25]
P. Hurst,[9] J. Huston,[17] J. Huth,[9] J. Hylen,[7] M. Incagli,[23] J. Incandela,[7] H. Iso,[31]
H. Jensen,[7] C. P. Jessop,[9] U. Joshi,[7] R. W. Kadel,[14] E. Kajfasz,[7,*] T. Kamon,[30] T. Kaneko,[31]
D. A. Kardelis,[10] H. Kasha,[34] Y. Kato,[19] L. Keeble,[30] R. D. Kennedy,[27] R. Kephart,[7] P. Kesten,[14]
D. Kestenbaum,[9] R. M. Keup,[10] H. Keutelian,[7] F. Keyvan,[4] D. H. Kim,[7] H. S. Kim,[11] S. B. Kim,[16]
S. H. Kim,[31] Y. K. Kim,[14] L. Kirsch,[2] P. Koehn,[25] K. Kondo,[31] J. Konigsberg,[9] S. Kopp,[5]
K. Kordas,[11] W. Koska,[7] E. Kovacs,[7,*] W. Kowald,[6] M. Krasberg,[16] J. Kroll,[7] M. Kruse,[24]
S. E. Kuhlmann,[1] E. Kuns,[27] A. T. Laasanen,[24] S. Lammel,[4] J. I. Lamoureux,[33] T. LeCompte,[10] S. Leone,[23]
J. D. Lewis,[7] P. Limon,[7] M. Lindgren,[4] T. M. Liss,[10] N. Lockyer,[21] O. Long,[21] M. Loreti,[20]
E. H. Low,[21] J. Lu,[30] D. Lucchesi,[23] C. B. Luchini,[10] P. Lukens,[7] J. Lys,[14] P. Maas,[33]
K. Maeshima,[7] A. Maghakian,[26] P. Maksimovic,[15] M. Mangano,[23] J. Mansour,[17] M. Mariotti,[23] J. P. Marriner,[7]
A. Martin,[10] J. A. J. Matthews,[18] R. Mattingly,[2] P. McIntyre,[30] P. Melese,[26] A. Menzione,[23] E. Meschi,[23]
G. Michail,[9] S. Mikamo,[13] M. Miller,[5] R. Miller,[17] T. Mimashi,[31] S. Miscetti,[8] M. Mishina,[13]
H. Mitsushio,[31] S. Miyashita,[31] Y. Morita,[13] S. Moulding,[26] J. Mueller,[27] A. Mukherjee,[7] T. Muller,[4]
P. Musgrave,[11] L. F. Nakae,[29] I. Nakano,[31] C. Nelson,[7] D. Neuberger,[4] C. Newman-Holmes,[7] L. Nodulman,[1]
S. Ogawa,[31] S. H. Oh,[6] K. E. Ohl,[34] R. Oishi,[31] T. Okusawa,[19] C. Pagliarone,[23] R. Paoletti,[23]
V. Papadimitriou,[7] S. Park,[7] J. Patrick,[7] G. Pauletta,[23] M. Paulini,[14] L. Pescara,[20] M. D. Peters,[14]
T. J. Phillips,[6] G. Piacentino,[3] M. Pillai,[25] R. Plunkett,[7] L. Pondrom,[33] N. Produit,[14] J. Proudfoot,[1]
F. Ptohos,[9] G. Punzi,[23] K. Ragan,[11] F. Rimondi,[3] L. Ristori,[23] M. Roach-Bellino,[32] W. J. Robertson,[6]
T. Rodrigo,[7] J. Romano,[5] L. Rosenson,[15] W. K. Sakumoto,[25] D. Saltzberg,[5] A. Sansoni,[8] V. Scarpine,[30]
A. Schindler,[14] P. Schlabach,[9] E. E. Schmidt,[7] M. P. Schmidt,[34] O. Schneider,[14] G. F. Sciacca,[23] A. Scribano,[23]
S. Segler,[7] S. Seidel,[18] Y. Seiya,[31] G. Sganos,[11] A. Sgolacchia,[3] M. Shapiro,[14] N. M. Shaw,[24]
Q. Shen,[24] P. F. Shepard,[22] M. Shimojima,[31] M. Shochet,[5] J. Siegrist,[29] A. Sill,[7,*] P. Sinervo,[11]
P. Singh,[22] J. Skarha,[12] K. Sliwa,[32] D. A. Smith,[23] F. D. Snider,[12] L. Song,[7] T. Song,[16]
J. Spalding,[7] L. Spiegel,[7] P. Sphicas,[15] A. Spies,[12] L. Stanco,[20] J. Steele,[33] A. Stefanini,[23]
K. Strahl,[11] J. Strait,[7] D. Stuart,[7] G. Sullivan,[5] K. Sumorok,[15] R. L. Swartz, Jr.,[10] T. Takahashi,[19]
K. Takikawa,[31] F. Tartarelli,[23] W. Taylor,[11] Y. Teramoto,[19] S. Tether,[15] D. Theriot,[7] J. Thomas,[29]
T. L. Thomas,[18] R. Thun,[16] M. Timko,[32] P. Tipton,[25] A. Titov,[26] S. Tkaczyk,[7] K. Tollefson,[25] A. Tollestrup,[7]
J. Tonnison,[24] J. F. de Troconiz,[9] J. Tseng,[12] M. Turcotte,[29] N. Turini,[3] N. Uemura,[31] F. Ukegawa,[21]
G. Unal,[21] S. van den Brink,[22] S. Vejcik III,[16] R. Vidal,[7] M. Vondracek,[10] R. G. Wagner,[1] R. L. Wagner,[7]

---

*Visitors.

N. Wainer,[7] R. C. Walker,[25] G. Wang,[23] J. Wang,[5] M. J. Wang,[28] Q. F. Wang,[26] A. Warburton,[11]
G. Watts,[25] T. Watts,[27] R. Webb,[30] C. Wendt,[33] H. Wenzel,[14] W. C. Wester III,[14] T. Westhusing,[10]
A. B. Wicklund,[1] R. Wilkinson,[21] H. H. Williams,[21] P. Wilson,[5] B. L. Winer,[25] J. Wolinski,[30] D. Y. Wu,[16]
X. Wu,[23] J. Wyss,[20] A. Yagil,[7] W. Yao,[14] K. Yasuoka,[31] Y. Ye,[11] G. P. Yeh,[7]
P. Yeh,[28] M. Yin,[6] J. Yoh,[7] T. Yoshida,[19] D. Yovanovitch,[7] I. Yu,[34] J. C. Yun,[7]
A. Zanetti,[23] F. Zetti,[23] L. Zhang,[33] S. Zhang,[15] W. Zhang,[21] and S. Zucchelli[3]

(CDF Collaboration)

[1]*Argonne National Laboratory, Argonne, Illinois 60439*
[2]*Brandeis University, Waltham, Massachusetts 02254*
[3]*Istituto Nazionale di Fisica Nucleare, University of Bologna, I-40126 Bologna, Italy*
[4]*University of California at Los Angeles, Los Angeles, California 90024*
[5]*University of Chicago, Chicago, Illinois 60637*
[6]*Duke University, Durham, North Carolina 27708*
[7]*Fermi National Accelerator Laboratory, Batavia, Illinois 60510*
[8]*Laboratori Nazionali di Frascati, Istituto Nazionale di Fisica Nucleare, I-00044 Frascati, Italy*
[9]*Harvard University, Cambridge, Massachusetts 02138*
[10]*University of Illinois, Urbana, Illinois 61801*
[11]*Institute of Particle Physics, McGill University, Montreal, Canada H3A 2T8*
and University of Toronto, Toronto, Canada M5S 1A7
[12]*The Johns Hopkins University, Baltimore, Maryland 21218*
[13]*National Laboratory for High Energy Physics (KEK), Tsukuba, Ibaraki 305, Japan*
[14]*Lawrence Berkeley Laboratory, Berkeley, California 94720*
[15]*Massachusetts Institute of Technology, Cambridge, Massachusetts 02139*
[16]*University of Michigan, Ann Arbor, Michigan 48109*
[17]*Michigan State University, East Lansing, Michigan 48824*
[18]*University of New Mexico, Albuquerque, New Mexico 87131*
[19]*Osaka City University, Osaka 588, Japan*
[20]*Universita di Padova, Instituto Nazionale di Fisica Nucleare, Sezione di Padova, I-35131 Padova, Italy*
[21]*University of Pennsylvania, Philadelphia, Pennsylvania 19104*
[22]*University of Pittsburgh, Pittsburgh, Pennsylvania 15260*
[23]*Istituto Nazionale di Fisica Nucleare, University and Scuola Normale Superiore of Pisa, I-56100 Pisa, Italy*
[24]*Purdue University, West Lafayette, Indiana 47907*
[25]*University of Rochester, Rochester, New York 14627*
[26]*Rockefeller University, New York, New York 10021*
[27]*Rutgers University, Piscataway, New Jersey 08854*
[28]*Academia Sinica, Taiwan 11529, Republic of China*
[29]*Superconducting Super Collider Laboratory, Dallas, Texas 75237*
[30]*Texas A&M University, College Station, Texas 77843*
[31]*University of Tsukuba, Tsukuba, Ibaraki 305, Japan*
[32]*Tufts University, Medford, Massachusetts 02155*
[33]*University of Wisconsin, Madison, Wisconsin 53706*
[34]*Yale University, New Haven, Connecticut 06511*
(Received 25 April 1994)

We present the results of a search for the top quark in 19.3 pb^{-1} of $\bar{p}p$ collisions at $\sqrt{s} = 1.8$ TeV. The data were collected at the Fermilab Tevatron collider using the Collider Detector at Fermilab (CDF). The search includes standard model $t\bar{t}$ decays to final states $ee\nu\bar{\nu}$, $e\mu\nu\bar{\nu}$, and $\mu\mu\nu\bar{\nu}$ as well as $e + \nu + $jets or $\mu + \nu + $jets. In the $(e, \mu) + \nu + $jets channel we search for b quarks from t decays via secondary vertex identification and via semileptonic decays of the b and cascade c quarks. In the dilepton final states we find two events with a background of $0.56^{+0.25}_{-0.13}$ events. In the $e, \mu + \nu + $jets channel with a b identified via a secondary vertex, we find six events with a background of 2.3 ± 0.3. With a b identified via a semileptonic decay, we find seven events with a background of 3.1 ± 0.3. The secondary vertex and semileptonic-decay samples have three events in common. The probability that the observed yield is consistent with the background is estimated to be 0.26%. The statistics are too limited to firmly establish the existence of the top quark; however, a natural interpretation of the excess is that it is due to $t\bar{t}$ production. We present several cross-checks. Some support this hypothesis; others do not. Under the assumption that the excess yield over background is due to $t\bar{t}$, constrained fitting on a subset of the events yields a mass of $174 \pm 10^{+13}_{-12}$ GeV/c^2 for the top quark. The $t\bar{t}$ cross section, using this top quark mass to compute the acceptance, is measured to be $13.9^{+6.1}_{-4.8}$ pb.

PACS number(s): 14.65.Ha, 13.85.Ni, 13.85.Qk

I. INTRODUCTION

The standard model [1,2] has enjoyed outstanding success in particle physics for two decades, yet one of its key constituents, the top quark, has remained unobserved. The top quark is required in the standard model as the weak isospin partner of the b quark. The theory does not predict the mass of the top quark, but direct searches at the Tevatron collider at Fermilab have placed a lower limit on its mass of 91 GeV/c^2 [3] at the 95% confidence level. The limit was recently extended to 131 GeV/c^2 [4]. These searches assume the top quark decays predominantly to a W boson and a b quark. Limits independent of the decay mode come from measurements of the width of the W boson and require $M_{top} > 62$ GeV/c^2 at 95% C.L. [5,6]. Global fits to precision electroweak measurements yield a favored mass of $M_{top} = 177^{+11+18}_{-11-19}$ GeV/c^2 [7].

In $\bar{p}p$ collisions top quarks are expected to be produced in pairs by both gluon-gluon fusion and $q\bar{q}$ annihilation. Above a top mass of about 100 GeV/c^2, $q\bar{q}$ annihilation is expected to be the dominant production source. Cross sections have been calculated within QCD at next-to-leading order (NLO) [8]. Recent work has extended those results with the inclusion of classes of higher-order diagrams dominated by the emission of multiple soft gluons [9]. The resulting cross section ranges from 38.9 pb at a top-quark mass of 120 GeV/c^2 to 4.2 pb at a mass of 180 GeV/c^2, and has been tabulated in Ref. [10], which also includes a study of the systematic uncertainties of this calculation. We do not explicitly include in this search single top production via W-gluon fusion [11], which is expected to occur at a significantly reduced rate relative to $t\bar{t}$ production and is expected to produce forward jets that are outside of the acceptance of this study.

Within the framework of the standard model the top quark decays almost exclusively into a W boson and a b quark. If the top mass is greater than the sum of the masses of the W boson and the b quark, about 85 GeV/c^2, the W boson will be real. As shown in Fig. 1, the two W bosons subsequently decay either to a lepton and a neutrino, or a quark and an antiquark, while the b quarks hadronize to jets. The approximate branching fractions for the different decay modes are listed in Table I. The $t\bar{t}$ decays can be categorized by the decay mode of the final state W^+W^- pair. Most often both W bosons will decay to a quark-antiquark pair, leading to a fully hadronic final state. This happens for about 44% of $t\bar{t}$ decays, but a huge background from all other QCD multijet production processes makes isolation of the $t\bar{t}$ signal
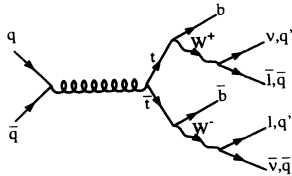
TABLE I. Decay modes for a $t\bar{t}$ pair and their approximate branching ratios (to lowest order) assuming charged-current decays. The symbol q stands for a light quark: u,d,c,s.

Decay mode	Branching ratio
$t\bar{t} \to (q\bar{q}'b)(q\bar{q}'\bar{b})$	36/81
$t\bar{t} \to (q\bar{q}'b)(e\nu\bar{b})$	12/81
$t\bar{t} \to (q\bar{q}'b)(\mu\nu\bar{b})$	12/81
$t\bar{t} \to (q\bar{q}'b)(\tau\nu\bar{b})$	12/81
$t\bar{t} \to (e\nu b)(\mu\nu\bar{b})$	2/81
$t\bar{t} \to (e\nu b)(\tau\nu\bar{b})$	2/81
$t\bar{t} \to (\mu\nu b)(\tau\nu\bar{b})$	2/81
$t\bar{t} \to (e\nu b)(e\nu\bar{b})$	1/81
$t\bar{t} \to (\mu\nu b)(\mu\nu\bar{b})$	1/81
$t\bar{t} \to (\tau\nu b)(\tau\nu\bar{b})$	1/81

extremely difficult [12]. If one requires that at least one of the W bosons decay leptonically to an e or a μ, the background is substantially reduced. Because of the difficulties associated with identifying the hadronic decays of τ leptons, the backgrounds to these decays cannot be substantially reduced. When just one of the W bosons decays to an electron or muon, the final state includes a charged lepton with high transverse momentum (P_T), an imbalance from the undetected neutrino, referred to as missing E_T or $\not{E}_T$, and four or more jets from the hadronized quarks. Decays of W bosons to τ leptons are not explicitly included in the search described in this paper except when they subsequently decay to an electron or a muon. This "lepton + jets" mode occurs about 30% of the time, and the background comes predominantly from higher-order production of W bosons, where the W recoils against significant jet activity (see Fig. 2). This is referred to as "W+multijet" background, and Monte Carlo studies indicate that the rate is about 2–10 times larger than the $t\bar{t}$ rate, depending on the top mass and the jet selection requirements used. Finally, about 5% of the time both W^+ and W^- decay to an electron or muon. The background in this "dilepton mode" comes from direct $b\bar{b}$, WW, $Z \to \tau\tau$, Drell-Yan production, and lepton misidentification. After imposing selection requirements, a signal-to-background ratio greater than 1.0 can be achieved with reasonable efficiency for $t\bar{t}$.

This paper describes a search for $t\bar{t}$ production using 19.3±0.7 pb^{-1} of $\bar{p}p$ collisions at $\sqrt{s} = 1.8$ TeV collected with the Collider Detector at Fermilab (CDF) between August of 1992 and May of 1993. The search uses both the lepton + jets mode and the dilepton mode, where the leptons are required to be either electrons or muons. In the dilepton mode it is sufficient to make various kine-
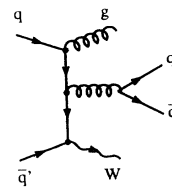

FIG. 1. Tree-level top-quark production by $q\bar{q}$ annihilation followed by the standard model top-quark decay chain.

FIG. 2. An example of W+multijet production.

matic and topological cuts to suppress the backgrounds. In the lepton + jets mode this is not the case. The search in the lepton + jets mode described here relies on the fact that standard model top decays always contain a b quark in the final state. Suppression of the W+multijet background in this search relies on the identification of at least one b or $\bar{b}$ quark among the decay products.

The paper is organized as follows. In Sec. II we describe briefly the CDF detector, with special attention given to those parts of the detector used in this search. In Sec. III we describe the identification of leptons and jets in the CDF detector. This includes triggering on high transverse momentum electrons, muons, jets, and neutrinos and their reconstruction and identification.

The dilepton search is described in Sec. IV, beginning with the off-line candidate event selection and the evaluation of the acceptance for $t\bar{t}$ events with M_{top} ranging from 100 to 180 GeV/c^2. This section also describes the results of applying the event selection to the data. Finally, the details of the background calculations for the dilepton analysis are given, and a lower limit on M_{top}, based on the dilepton data alone, is presented.

In Sec. V we begin the description of the lepton + jets analysis with the event selection and the evaluation of the acceptance for that selection. The rate of heavy flavor production in W+multijet events is expected to be small [13]. To suppress the W+multijet background, we apply two different methods for identifying b quarks in the event (b tagging). The first method uses the CDF silicon vertex detector (SVX) to locate decay vertices of b hadrons that are separated from the primary event vertex as a result of the long b lifetime. The second technique is to search in the event for additional leptons (e or μ) from semileptonic decays of b hadrons. We refer to these as "soft lepton tags" (SLT's) because the e or μ typically has low momentum compared to leptons from W decays. These two techniques, including efficiencies, background estimates, and the number of observed candidates, are described in Secs. V B and V C, respectively. While the background estimates described in Sec. V B apply specifically to the SVX search, much of the motivation and discussion of the techniques used to measure the backgrounds applies to SLT backgrounds as well. The accuracy of these background estimates can be checked in several different ways, and these are discussed in Secs. V B 3 and V C 2. The most direct method of checking backgrounds from W+multijet events is to study Z+multijet events, although in practice the statistics in Z + multijet events are limited. Details of this study are described in Sec. V D.

In summary, there are three counting experiments: dilepton events, SVX b tags, and SLT b tags. The individual results of these experiments each show an excess of candidate events over the expected background, although the sizes of the separate excesses are not statistically significant. These results are then combined into a single result in Secs. VI and VII. In Sec. VI we discuss the statistical significance of the combined result and the correlations and overlaps in both the signal acceptance and background estimates among the dilepton, SVX, and SLT analyses. In Sec. VII the combined and individual $t\bar{t}$

cross sections for the three analyses are calculated and compared.

In Sec. VIII we describe studies of the kinematic properties of the lepton + jet candidate events to determine if these events are qualitatively consistent with the $t\bar{t}$ hypothesis. Studies of both the b-tagged sample and the entire sample of candidate events before b tagging are presented. In Sec. IX we describe the kinematic reconstruction of $t\bar{t}$ pairs from the b-tagged events and the measurement of M_{top}. We conclude in Sec. X.

II. THE CDF DETECTOR

The CDF detector is a general-purpose detector designed to study the physics of $\bar{p}p$ collisions. It has both azimuthal and forward-backward symmetry. A superconducting solenoid of length 4.8 m and radius 1.5 m generates a 1.4-T magnetic field and contains tracking chambers used to detect charged particles and measure their momenta.

Surrounding the solenoid are sampling calorimeters used to measure the electromagnetic and hadronic energy of jets and electrons. Outside the calorimeters are drift chambers used for muon detection. A side-view cross section of the CDF detector is shown in Fig. 3. The polar angle (θ) in spherical coordinates is measured from the proton beam axis, and the azimuthal angle (ϕ) from the plane of the Tevatron. A more complete description of the CDF detector can be found elsewhere [14,15]. Important new additions to the detector, as well as the components of the CDF detector most relevant to the search for $t\bar{t}$ events, are summarized below.

The solenoid and tracking volume of CDF is surrounded by calorimeters, which cover 2π in azimuth, and in pseudorapidity, η, from -4.2 to 4.2 [16]. The calorimeters are segmented in azimuth and pseudorapidity to form a projective tower geometry, which points back to the nominal interaction point. There are three separate η regions of calorimeters, the central, end plug, and forward. Each region has an electromagnetic calorimeter [central electromagnetic (CEM), plug electromagnetic (PEM), and forward electromagnetic (FEM)] and behind it a hadronic calorimeter. The hadronic calorimeter overlapping the CEM is split into two parts, central (CHA) and wall (WHA), while single systems overlap PEM and FEM (PHA,FHA). In all cases, the absorber in the hadronic calorimeter is iron, and in the electromagnetic calorimeter, lead. The locations of the calorimeters are indicated in Fig. 3. Their coverage, thickness, and resolution are summarized in Table II. The energy resolution is given as a function of E_T, the projection of the observed energy (E) onto the plane transverse to the beam axis ($E_T = E \sin\theta$, where θ is shown in Fig. 3). The central towers are 15° wide in ϕ and 0.1 units wide in η and use a scintillator as the active sampling medium. The term "CHA" refers to both the CHA and the WHA throughout the rest of this paper. Located six radiation lengths deep in the CEM calorimeter, approximately at shower maximum for electromagnetic showers, are the central proportional chambers with strip and wire readout [central electromagnetic strip detector (CES)].
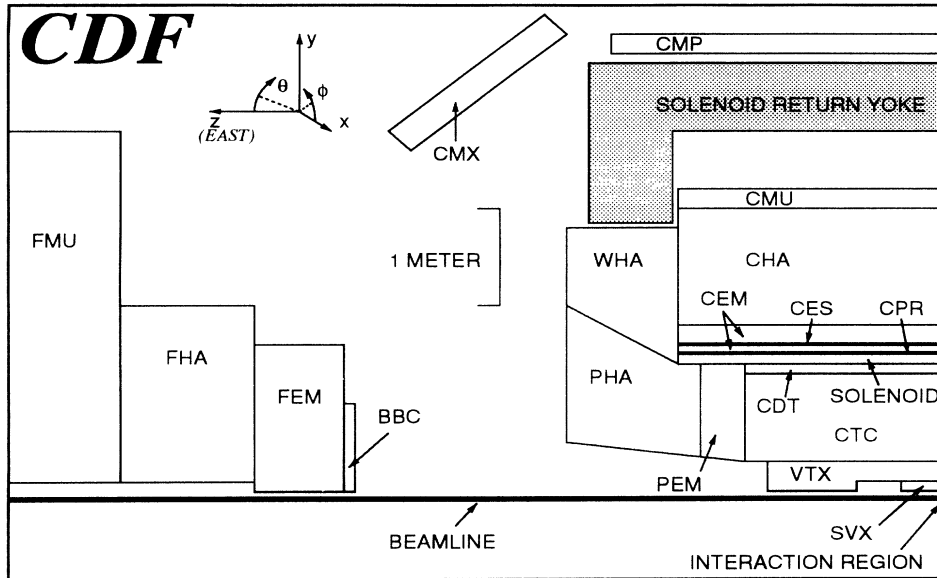
FIG. 3. A side-view cross section of the CDF detector. The detector is forward-backward symmetric about the interaction region, which is at the lower-right corner of the figure. See text for detector component definitions.

The CES provides shower-position measurements in both the z and r-ϕ views. Proportional chambers located between the solenoid and the CEM comprise the central-preradiator (CPR) detector which samples the early development of electromagnetic showers in the material of the solenoid coil. These chambers provide r-ϕ information only. In the end plug and forward region, gas proportional chambers are used as the active media in the calorimeters, and the tower size is 5° in ϕ, and 0.1 units in η. Electromagnetic shower positions are measured in the PEM with θ- and ϕ-oriented strips, giving a position resolution of approximately 0.2 cm by 0.2 cm.

Within the magnetic field of the solenoid are three tracking chambers for charged particles. Surrounding the 1.9-cm radius beryllium beampipe is a four-layer silicon microstrip vertex detector (SVX) [15], which was installed in CDF in 1992. The SVX is 51 cm long and consists of two identical cylindrical modules, which meet at $z = 0$. Because $\bar{p}p$ interactions are spread along the beamline with standard deviation $\sigma \sim 30$ cm, the geometrical

acceptance of the SVX is about 60% for $\bar{p}p$ interactions. The four layers of the SVX are at distances of 3.0, 4.2, 5.7, and 7.9 cm from the beamline. Axial microstrips with 60-μm pitch on the three innermost layers and 55-μm pitch on the outermost layer provide precision track reconstruction in the plane transverse to the beam. The SVX single-hit resolution is measured in data to be $\sigma = 13$ μm, and the impact parameter resolution at high momentum is measured to be $\sigma = 17$ μm. Because of radiation damage to the SVX readout chip, the performance of the SVX deteriorated over the course of the data taking period [15]. On the innermost layer, the ratio of the average analogue pulse size from a particle to the noise level (S/N) decreased from approximately 9 to 6 from the beginning to the end of the data taking period. The SVX performance is discussed in further detail in Sec. V B.

Outside the SVX is a vertex (VTX) drift chamber, installed in 1992, which provides tracking information up to a radius of 22 cm and $|\eta| < 3.25$. The VTX is used to measure the $\bar{p}p$ interaction vertex along the z axis with a resolution of 1 mm. Both the SVX and VTX are mounted inside the central tracking chamber (CTC), which is a 3.2-m-long drift chamber with an outer radius of 132 cm containing 84 concentric, cylindrical layers of sense wires. Sixty layers have wires parallel to the beam direction (axial wires) and provide tracking in the r-ϕ plane. Twenty-four layers (stereo) are tilted at $+3$ degrees or -3 degrees with respect to the beam direction. Together, the axial and stereo wires provide tracking in the r-z plane.

SVX track reconstruction is performed by assigning hits on the silicon strips to previously identified CTC tracks. A CTC track with at least two associated SVX hits is defined to be an SVX track. For this analysis, we calculate SVX χ^2, defined to be the increase in the track fit χ^2 when the SVX hits are included in the CTC track fit, divided by the number of included SVX hits. We require the SVX χ^2 to be less than six. We further require that at least two of the SVX hits must be associated with exactly one CTC track, contain no SVX channels with

TABLE II. Summary of CDF calorimeter properties. The symbol $\oplus$ signifies that the constant term is added in quadrature in the resolution. Energy resolutions for the electromagnetic calorimeters are for incident electrons and photons, and for the hadronic calorimeters are for incident isolated pions. Energy is given in GeV. Thicknesses are given in radiation lengths (X_0) and interaction lengths (λ_0) for the electromagnetic and hadronic calorimeters, respectively.

System	η Range	Energy resolution	Thickness
CEM	$|\eta| < 1.1$	$13.7\%/\sqrt{E_T} \oplus 2\%$	$18X_0$
PEM	$1.1 < |\eta| < 2.4$	$22\%/\sqrt{E} \oplus 2\%$	$18-21X_0$
FEM	$2.2 < |\eta| < 4.2$	$26\%/\sqrt{E} \oplus 2\%$	$25X_0$
CHA	$|\eta| < 0.9$	$50\%/\sqrt{E_T} \oplus 3\%$	$4.5\lambda_0$
WHA	$0.7 < |\eta| < 1.3$	$75\%/\sqrt{E} \oplus 4\%$	$4.5\lambda_0$
PHA	$1.3 < |\eta| < 2.4$	$106\%/\sqrt{E} \oplus 6\%$	$5.7\lambda_0$
FHA	$2.4 < |\eta| < 4.2$	$137\%/\sqrt{E} \oplus 3\%$	$7.7\lambda_0$

low gain or high noise, and have a charge profile consistent with that of a single particle. Studies using samples of jet triggers show that 78% of SVX tracks pass these additional selection requirements, independent of track P_T (P_T is defined similarly to E_T; $P_T = P \sin\theta$). Most of the inefficiency comes from the quality requirements made on at least two of the SVX hits. The SVX χ^2 requirement is approximately 96% efficient. Tracks that pass these requirements are referred to as good SVX tracks. The momentum resolution of the SVX-CTC system is $\delta P_T / P_T = [(0.0009 P_T)^2 + (0.0066)^2]^{1/2}$, where P_T has units of GeV/c.

The central calorimeters act as a hadron absorber for the central muon (CMU) detection system, which consists of four layers of drift chambers located outside the central hadronic calorimeter. The CMU system covers $|\eta| < 0.6$ and can be reached by muons with P_T in excess of 1.4 GeV/c. In 1992, 0.6 m of steel was added behind the CMU system for additional hadron absorption, and an additional four layers of drift chambers were added behind the steel to detect muons. This system is referred to as the central muon upgrade (CMP). Approximately 84% of the solid angle for $|\eta| < 0.6$ is covered by the CMU system, 63% by the CMP, and 53% by both. In addition, the coverage of the central muon system has been extended to the pseudorapidity range $0.6 < |\eta| < 1.0$ through the addition of four free-standing conical arches, which hold drift chambers for muon detection, sandwiched between scintillator counters for triggering. This system is called the central muon extension (CMX). Approximately 71% of the solid angle for $0.6 < |\eta| < 1.0$ is covered by the CMX. In all muon systems in the central region, muon P_T is measured with charged tracking and has a tracking resolution as discussed above.

The trigger system for the 1992–1993 CDF run is a three-level system. Each level is a logical OR of a number of triggers designed to select events with electrons, muons, or jets. We briefly outline the trigger function here; the selection criteria are described in detail in Sec. III.

Preamplifiers on detector channels provide two outputs: one, the "fast output," for immediate use by the trigger system, and the other for temporary front-end data storage until the trigger decision is made. The lowest-level trigger, "level 1" uses fast outputs from the three central muon detectors for muon triggers and fast outputs from all the calorimeters for electron and jet triggers. The calorimeter information is summed into towers of ($\Delta\eta = 0.2$)×($\Delta\phi = 15°$) for both the electromagnetic and hadronic calorimeters. At a typical luminosity of 5×10^{30} cm^2 s^{-1}, the rate of level-1 triggers is approximately 1 kHz.

The second-level trigger, "level 2," uses the calorimeter trigger information with greater sophistication. A list of calorimeter clusters is provided by a nearest-neighbor hardware cluster finder. For each cluster, the E_T, average ϕ, and average η are determined. This information is combined with a list of r-ϕ tracks provided by the central fast tracker (CFT), a hardware track processor, which uses fast timing information from the CTC as input. The CFT momentum resolution is $\delta P_T / P_T \approx 0.035 \times P_T$, with

an efficiency of 93.5±0.3% for tracks with P_T above 10 GeV/c. In addition, muon track-segment information is available in the second-level trigger from the CMU system, the CMP, and the CMX. Highly electromagnetic clusters can be matched to CFT tracks to form electron candidates. Muon track segments are also matched to CFT tracks to form muon candidates. At a typical instantaneous luminosity of 5×10^{30} cm^2 s^{-1}, the level-2 output rate is approximately 12 Hz.

Software reconstruction algorithms constitute the third level of triggering ("level 3"). The events selected in level 2 are read out into commercial processors (Silicon Graphics multi-CPU Power Servers), with combined processing power of approximately one billion instructions per second. The algorithms used in this "on-line" system are identical to those used in subsequent "off-line" reconstruction of the events selected by the level-3 trigger for output to magnetic tape. Most of the execution time is used for three-dimensional track reconstruction in the CTC. The output rate of the level-3 trigger was approximately 5 Hz, and the events were stored on magnetic tape for offline processing.

The CDF luminosity is measured using the beam-beam counters (BBC's). They consist of two planes of scintillation counters covering the angular range of 0.32° to 4.47° in both the forward and backward directions ($3.24 < |\eta| < 5.88$). Hits in both counters that arrive coincident with the particle bunches crossing through the detector serve as both a minimum-bias trigger and the primary luminosity monitor. The rate (number) of coincidences in these counters, divided by the effective cross section of the counters, is what gives the instantaneous (integrated) luminosity, respectively.

In previous publications, CDF normalized the BBC cross section ($\sigma_{BBC} = 46.8 \pm 3.2$ mb) to measurements at $\sqrt{s} = 546$ GeV, extrapolated to $\sqrt{s} = 1.8$ TeV [17]. With recent direct measurements of the elastic and total cross sections by the CDF collaboration [18], we are able to make a direct measurement of the BBC cross section of $\sigma_{BBC} = 51.2 \pm 1.7$ mb. After accounting for possible backgrounds in the BBC's, we have a total uncertainty of 3.6% on the integrand luminosity.

III. IDENTIFICATION AND MODELING OF JETS AND HIGH P_T LEPTONS

A. Triggers

The events for this analysis were collected using inclusive electron and muon triggers that make use of tracking, calorimeter, and muon chamber information. The level-1 calorimeter trigger requires a single trigger tower with $E_T > 6$ GeV (8 GeV) for the CEM (PEM, FEM), or $E_T > 8$ GeV (25 GeV) for the CHA (PHA, FHA). The central electron trigger at level 2 requires an energy cluster in the CEM with $E_T > 9$ GeV, together with an associated CTC track with transverse momentum $P_T > 9.2$ GeV/c, as measured by the CFT. Since CFT information is available only for $|\eta| \leq 1.0$, the plug electron trigger at level-2 simply requires either an energy cluster

in the PEM with $E_T > 20$ GeV, or $E_T > 15$ GeV and $\not{E}_T > 15$ GeV. An electromagnetic cluster is constructed as a set of contiguous CEM (PEM) trigger towers each with $E_T > 7$ GeV (4 GeV), including at least one "seed" tower with $E_T > 9$ GeV (6 GeV). The ratio of hadronic to electromagnetic energy in the cluster (E_{had}/E_{EM}) is required to be less than 0.125. For central electrons, the level-3 algorithm requires that the reconstructed cluster E_T be above 18 GeV and that there be a reconstructed track with $P_T > 13$ GeV/c pointing to it. For plug electrons, the reconstructed E_T is required to be above 20 GeV with $\not{E}_T > 20$ GeV. The central electron trigger is measured to be $(92.8\pm0.2)\%$ efficient for electrons with $20 < E_T < 150$ GeV. The plug electron trigger is measured to be $(91.9\pm0.4)\%$ efficient for electrons from W decays with electron E_T in the range $25 < E_T < 150$ GeV.

The level-1 central muon trigger requires a pair of hits on radially aligned wires in the CMU or CMX chambers. The transverse momentum, P_T, of the muon track segment is measured by using the arrival times of the drift electrons at the sense wires to determine the deflection angle due to the magnetic field. The muon trigger requires a track segment in the CMU system with $P_T > 6$ GeV/c in coincidence with hits in the CMP, or a track segment in the CMX with $P_T > 10$ GeV/c in coincidence with hits on scintillators placed on both sides of the chambers. The scintillator coincidence is required to occur in a narrow time window centered about the interaction time, in order to reduce the rate from particles not associated with the primary interaction.

The inclusive muon trigger at level 1 for the CMX was fully functional for 30% of the run. Throughout the run, sensitivity to top decays with a muon passing through CMX was preserved by a trigger that required a single calorimeter tower in the level-1 trigger and the CMX muon signature in the level-2 trigger. This trigger was present for 83% of the integrated luminosity of the run. The level-2 muon trigger requires a match between a CFT track in the r-ϕ plane with $P_T > 9.2$ GeV/c and a track segment in the muon chambers, which was triggered at level 1. The level-3 muon trigger requires a match better than 10 cm in $r\Delta\phi$ between a reconstructed track with $P_T > 18$ GeV/c, extrapolated to the radius of the muon chambers, and a track segment in those chambers. In addition, the energy deposited in the associated CHA tower must be less than 6 GeV. The CMU system (CMX) muon trigger is measured to be $(86.8\pm1.9)\%$ $[(54.4\pm5.5)\%]$ efficient for muons with $P_T > 20$ GeV/c.

The events collected with inclusive jet triggers are used to study the b-tagging backgrounds for both the SVX and SLT (see Sec. V B 3). The jet triggers were made by demanding a single trigger tower above thresholds (see above) at level 1 and a localized cluster of electromagnetic and hadronic transverse energy in the calorimeter at level 2. A jet cluster is initiated by a seed tower with $E_T > 3$ GeV and consists of all contiguous towers with $E_T > 1$ GeV in η and ϕ. Four triggers were used with separate thresholds of 20, 50, 70, and 100 GeV on the transverse energy of the clusters.

B. Electron selection

In the e+jets search, we use electrons in the central rapidity region ($|\eta| \leq 1.0$). For the dilepton search, electrons are also included in those regions in the plug calorimeters where tracking data are available.

The CDF central electron candidates have a CTC track extrapolating to a CEM cluster, which is constructed from a seed tower with $E_T > 3$ GeV and the two neighboring towers in pseudorapidity. The size of the cluster is three towers in pseudorapidity ($\Delta\eta = 0.3$) by one tower in azimuth ($\Delta\phi = 15°$). Fiducial cuts on the shower position, as measured in the CES, are applied to ensure that the electron candidate is away from calorimeter boundaries and that the energy is well measured. The fiducial volume for electrons covers 84% of the solid angle in the region $|\eta| < 1.0$.

Electrons from converted photons can be removed with high efficiency, $(88\pm4)\%$, using tracking information. Any electron that does not have a matching VTX track, or that can be paired with an oppositely charged CTC track to form a small effective mass, is rejected, since it might have come from a photon conversion.

The following electron selection variables are used to discriminate against charged hadrons: (1) the ratio of hadronic energy to electromagnetic energy of the cluster, E_{had}/E_{EM}; (2) the ratio of cluster energy to track momentum, E/P; (3) a comparison of the lateral shower profile in the calorimeter cluster with that of test beam electrons, L_{shr} [17]; (4) the distance between the position of the extrapolated track and the CES shower position measured in the r-ϕ and z views, Δx and Δz; (5) a χ^2 comparison of the CES shower profiles with those of test beam electrons, χ^2_{strip}; (6) the distance between the interaction vertex and the reconstructed track in the z direction, z-vertex match; and (7) isolation.

Two different isolation variables are used: calorimeter isolation I_{cal}, defined as the transverse energy in the towers within a cone of radius $R = \sqrt{(\Delta\phi)^2 + (\Delta\eta)^2} = 0.4$ centered on the electron but *excluding* the electron cluster's transverse energy, and track isolation I_{trk}, defined as the P_T sum of CTC tracks within a cone $R = 0.25$, excluding the lepton track contribution.

Table III lists the selection requirements for high-P_T central electrons in the e+jets search, and for the dilepton search, where both strict and loose criteria are defined. In the e+jets search, the selection efficiency for electrons, determined from a sample of $Z \to ee$ events, is found to be $(84\pm2)\%$, excluding the loss of efficiency from the removal of photon conversions (5%) and from the isolation cut (13% for $t\bar{t}$ events). In the dilepton search, the selection efficiencies for central electrons are $(87\pm1)\%$ and $(94\pm1)\%$ for the strict and loose selection criteria, respectively, excluding the loss of efficiency from the removal of photon conversions (5%) and from the isolation cut (9% for $t\bar{t}$ events). The detection efficiencies for $t\bar{t}$ events are measured from Monte Carlo data, as described in Secs. IV and V and the values measured from Z decays are used as cross checks.

Plug electrons are selected using the following variables: (1) E_{had}/E_{EM}; (2) the longitudinal and transverse

TABLE III. Central electron selection requirements and efficiencies. For the dilepton analysis only one central electron or muon is required to pass the I_{trk} cut. The efficiencies given in the table are for the combination of all the cuts, except the isolation requirement. E_T is in units of GeV.

Variable	e+jets cut	Dilep strict cuts	Dilep loose cuts
$E_{\mathrm{had}}/E_{\mathrm{EM}}$	<0.05	<0.05	$<0.055+0.045E_T/100$
E/P	<1.5	<2.0	<4.0
L_{shr}	<0.2	<0.2	<0.2
$|\Delta x|$	<1.5 cm	<1.5 cm	<1.5 cm
$|\Delta z|$	<3.0 cm	<3.0 cm	<3.0 cm
χ^2_{strip}	<10	<15	
z-vertex match	<5.0 cm		
Isolation	$I_{\mathrm{cal}}/E_T(e)<0.1$	$I_{\mathrm{trk}}<3$ GeV/c	$I_{\mathrm{trk}}<3$ GeV/c
Efficiency	$(84\pm2)\%$	$(87\pm1)\%$	$(94\pm1)\%$

shower profile, χ^2_{depth} and χ^2_{trans}; (3) CTC track match; (4) the ratio of the number of VTX hits pointing to the calorimeter cluster to the number predicted, f_{VTX}; and (5) I_{cal}, defined as above. Because of the CTC geometrical acceptance, the efficiency of the track requirement is reduced to 50% at $|\eta|=1.35$ and falls rapidly beyond that. The effective coverage for plug electrons is $1.20<|\eta|<1.35$. Fiducial cuts, required to ensure a reliable energy measurement, reduce the solid angle coverage in this region by an additional 11%. The plug electron selection efficiency is found to be $(85\pm3)\%$ on $W\rightarrow e\nu$ candidates, excluding the loss due to the isolation cut (25% for $t\bar{t}$ events). Calorimeter isolation is *always* required of plug electrons, whereas only one central electron or muon per event is required to pass the I_{trk} cut for the dilepton analysis. The high-P_T plug electron selection requirements are summarized in Table IV.

C. Muon selection

In the μ+jets search, we identify muons in the pseudorapidity region $|\eta|\leq1.0$ by requiring a match between a CTC track and a track segment in the muon chambers of CMU system, CMP, or CMX. For the dilepton search we also include muons in regions of the detector not covered by muon chambers but where track identification is good. These muons are identified by requiring the energy in the calorimeter tower in the path of the extrapo-

TABLE IV. Plug electron selection requirements and efficiencies. The efficiencies given in the table are for the combination of all the cuts, except the isolation requirement.

Variable	Cut
$E_{\mathrm{had}}/E_{\mathrm{EM}}$	<0.05
χ^2_{depth}	<15
χ^2_{trans}	<3
Track match	CTC track with hits in ≥3 axial layers pointing at cluster
f_{VTX}	$>50\%$
Isolation	$I_{\mathrm{cal}}/E_T(e)<0.1$
Efficiency	$(85\pm3)\%$

lated track to be consistent with that for a minimum ionizing particle. These muon candidates are called central minimum ionizing particles. This extends muon identification to $|\eta|<1.2$ as well as covering azimuthal holes in the region $|\eta|<1.0$. Note that central minimum ionizing particles do not cause triggers.

The following variables are used to separate muons from hadrons that interact in the calorimeters and from cosmic rays: (1) an energy deposition in the electromagnetic or hadronic calorimeters characteristic of minimum ionizing particle, E_{EM} or E_{had} energy; (2) the closest approach of the reconstructed track to the beam line, impact parameter; (3) the distance between the interaction vertex and the reconstructed track in the z direction, z-vertex match; (4) the matching distance between the extrapolated track and the track segment in the muon chambers, $\Delta x=r\Delta\phi$; and (5) I_{cal}, defined for muons such that the muon energy deposition in the calorimeter is removed or I_{trk} (see Sec. III B). The high-P_T muon selection requirements are summarized in Table V. For dimuons, at least one must be in the CMU or CMU-CMP region. The μ+jets search muon selection efficiency for a sample of $Z\rightarrow\mu\mu$ events is found to be $(90.6\pm1.4)\%$, excluding losses due to the isolation cut (19% for $t\bar{t}$ events). The muon selection efficiency for the dilepton search is found to be $(93.0\pm1.0)\%$, excluding the loss due to the isolation cut (8% for $t\bar{t}$ events). The detection efficiencies for $t\bar{t}$ events are measured from Monte Carlo data, as described in Secs. IV and V and the values measured from Z decays are used as cross-checks.

In the dilepton search, the selection requirements for central minimum ionizing particles are the same as those used for central muons (see Table V) except that there is no Δx cut, and the track isolation cut is replaced by a calorimeter isolation cut, $I_{\mathrm{cal}}<5$ GeV. Calorimeter isolation is *always* required of central minimum ionizing particles, whereas only one central electron or muon per event is required to pass the I_{trk} cut for the dilepton analysis.

The cut on the sum of electromagnetic and hadronic energy listed in Table V was designed to remove, from the central minimum ionizing particle sample, tracks that point at empty calorimeter towers due to track reconstruction problems. For simplicity, this cut is also applied to all central muons in the dilepton analysis. It is

TABLE V. Selection requirements and efficiencies for high-P_T muons. For dileptons, only one central electron or muon is required to pass the I_{trk} cut. The efficiencies given in the table are for the combination of all the cuts, except the isolation requirement.

Variable	μ+jets cut	Dilepton cuts
η range	$\lvert\eta\rvert<1.0$	$\lvert\eta\rvert<1.2$
EM energy	<2 GeV	<2 GeV
Hadronic energy	<6 GeV	<6 GeV
$E_{EM}+E_{had}$		>0.1 GeV
Impact parameter	<3 mm	<3 mm
z-vertex match	<5.0 cm	<5.0 cm
$\lvert\Delta x\rvert$	<2 cm (CMU),	<10 cm (CMU),
	<5 cm (CMP, CMX)	<20 cm (CMP, CMX)
Isolation	$I_{cal}/P_T(\mu)<0.1$	$I_{trk}<3$ GeV/c
Efficiency	$(90.6\pm1.4)\%$	$(93.0\pm1.0)\%$

not used in the μ+jets analysis, where central minimum ionizing particles are not included. To ensure that the energy deposited is well measured, the same fiducial cuts in ϕ as used for electrons are applied to reject central minimum ionizing particles that are near a boundary between towers in the calorimeter. This requirement defines a fiducial volume that covers 85% of the solid angle for $\lvert\eta\rvert<1.2$. The identification efficiency for central minimum ionizing particles is found to be $(93.0\pm1.0)\%$, excluding the loss due to the isolation requirement (18% for $t\bar{t}$ events).

D. Jet identification and energy corrections

The CDF jet reconstruction algorithm uses a cone of fixed radius in η-ϕ space. A detailed description of the algorithm can be found in Ref. [19]. For this analysis we have chosen the radius o the cone to be 0.4, which has been found to give improved efficiency compared to larger cone sizes for counting jets from Monte Carlo $t\bar{t}$ decays.

Jets may be mismeasured due to a variety of effects. These include effects due to (i) calorimeter nonlinearities, (ii) curvature of low-momentum charged particles by the CDF magnetic field, (iii) reduced calorimeter response at boundaries between modules and calorimeter subsystems, (iv) contributions from the underlying event, (v) out-of-cone losses, and (vi) undetected energy carried by muons or neutrinos. The correction factor depends on the jet E_T and η, and is meant to reproduce the average jet E_T correctly, not to reduce the jet fluctuations around this mean E_T. Typically, the jet corrections increase jet energies by about 30%, and are fully described in Refs. [19] and [20]. Estimates of the uncertainty in our knowledge of the reconstructed jet E_T due to detector effects range from 5% for 20 GeV corrected jets to 3% at 300 GeV [21]. In addition, there is a theoretical uncertainty in jet energies due to the possibility of large-angle gluon radiation, which may not be modeled correctly in perturbative-QCD Monte Carlo programs. We estimate that the combination of these uncertainties may be taken as an effective 10% uncertainty on the energy scale of jets.

It is possible to check the energy scale set by the jet corrections using the direct photon data sample. This contains a subset of two-jet events for which most of the energy of one jet is carried by a single γ, π^0, or η and is fully contained in the CEM calorimeter, where the energy scale is well understood.

Balancing the transverse momentum of the "photon" with the corrected jet E_T probes the behavior of the correction function. Cuts are imposed to require that there be no additional jet activity in the events. Figure 4 shows $\Delta=[E_T(\text{photon})-E_T(\text{recoiling jet})]/E_T(\text{photon})$, where the E_T (recoiling jet) is the corrected jet E_T, and $E_T(\text{photon})$ ranges from 16 to 30 GeV. The average imbalance is measured to be 2.7%, much smaller than the 10% uncertainty detailed above. Clearly this 2.7% imbalance in the photon-jet system could be used to reduce the jet energy uncertainties. However, the balancing technique can be affected by low-energy gluon radiation that is not detected, or by the mismeasurement of the
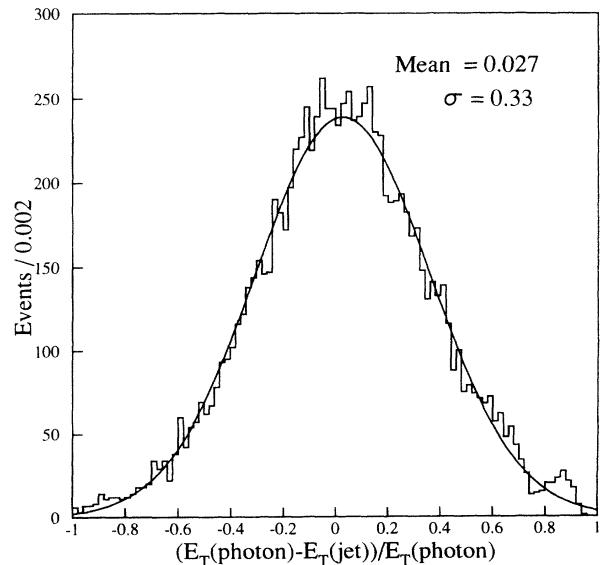

FIG. 4. $\Delta=[E_T(\text{photon})-E_T(\text{recoiling jet})]/E_T(\text{photon})$. The jet transverse energy is corrected.

photon energy in the cases where the photon is actually a π^0. Thus we will use 10% as the jet energy uncertainty in what follows. Studies are in progress to provide a better understanding of these issues.

E. $\not\!\!E_T$ measurement

This missing transverse energy ($\not\!\!E_T$) is defined to be the negative of the vector sum of transverse energy in all calorimeter towers with $|\eta| < 3.6$ [22]. The η range is restricted because the final focusing magnets of the Tevatron obscure parts of the forward hadron calorimeter. To be included in the sum, individual tower energies (E, not E_T) must exceed detector-dependent energy thresholds. These thresholds are 100 MeV in the CEM, CHA, and WHA, 300 MeV in the PEM, 500 MeV in the PHA and FEM, and 800 MeV in the FHA. For events with muon candidates, the vector sum of the calorimeter transverse energy is corrected by vectorially subtracting the energy deposited by the muon and then adding the P_T of the muon candidate as measured in the CTC. This is done for muons passing the high-P_T threshold, and in the case of the SLT analysis, for muon candidates with $P_T > 10$ GeV/c, which pass the soft lepton cuts described in Sec. V C 1. For the dilepton search, the $\not\!\!E_T$ is calculated using the corrected jet energies. The $\not\!\!E_T$ resolution is given approximately by $0.7\sqrt{\sum E_T}$, where $\sum E_T$ is the scalar sum of the transverse energy measured in units of GeV.

F. Monte Carlo programs

We use several different Monte Carlo generators to evaluate acceptances and, in certain cases, backgrounds. The primary Monte Carlo generator used for the signal acceptance in both the dilepton analysis and the lepton + jets analyses is ISAJET [23]. We use version 6.36 of ISAJET. ISAJET is a parton shower Monte Carlo program based on the leading-order QCD matrix elements for the hard-scattering subprocess, incoherent gluon emission, and independent fragmentation of the outgoing partons. ISAJET is also used to model WW background and $b\bar{b}$ backgrounds in the dilepton analysis. For both the $b\bar{b}$ and $t\bar{t}$ Monte Carlo samples, we use the CLEO Monte Carlo program [24] to model the decay of b hadrons. Version 5.6 of the HERWIG Monte Carlo generator [25] is also used and compared to ISAJET to estimate systematic uncertainties. In addition, HERWIG is the primary Monte Carlo used to model the kinematics of $t\bar{t}$ production in Secs. VIII and IX. HERWIG is a Monte Carlo program based on the leading order QCD matrix elements for the hard process, followed by coherent parton shower evolution, hadronization, and an underlying event model based on data.

In the lepton + jets analysis, the dominant background is production of W bosons in association with heavy quark pairs. As discussed in Sec. V B 3, this background is estimated directly from the data.

The Monte Carlo program used to study the kinematics of the W+jet background is VECBOS [26], which is described in Sec. VIII A. VECBOS is a parton-level Monte Carlo program based on tree-level matrix element calculations. We developed two techniques to transform the

partons produced by VECBOS into hadrons and jets, which can then be processed by the CDF detector simulation. One employs ISAJET, evolving the final-state light quarks and gluons according to a Field-Feynman fragmentation function [27] tuned on CDF data. The other uses HERWIG, adapted to perform the coherent shower evolution of both initial and final-state partons from an arbitrary hard-scattering subprocess [28].

With all Monte Carlo samples, the response of the CDF detector to the resulting final-state particles is simulated, and jets and leptons are reconstructed using the CDF reconstruction algorithms. This enables the sample of Monte Carlo events to be subjected to the same cuts as are applied to the data.

IV. HIGH-P_T DILEPTON SEARCH

A. Event selection

The search for $t\bar{t}$ in the dilepton channel concentrates on the process

$$\bar{p}p \to t\bar{t} + X \to W^+ W^- b\bar{b} + X \to l^+ \nu l^- \bar{\nu} + X \ .$$

The presence of two oppositely charged, high-P_T leptons (e or μ), together with large $\not\!\!E_T$, is a clean signature for the production and decay of a $t\bar{t}$ pair. Backgrounds to this signature come from WW, $\gamma/Z \to ee$, $\mu\mu$ (Drell-Yan), $Z \to \tau\tau$, $b\bar{b}$, and lepton misidentification. For high mass top, above 120 GeV/c^2, the two b quarks can have significant energy and are detected with good efficiency as hadronic jets in the calorimeter. Therefore, an additional two-jet requirement preserves most of the $t\bar{t}$ signal for high mass top and significantly reduces the backgrounds, which contain extra jets only through higher-order processes. Figure 5 shows the lepton P_T, $\not\!\!E_T$, and jet E_T dis-
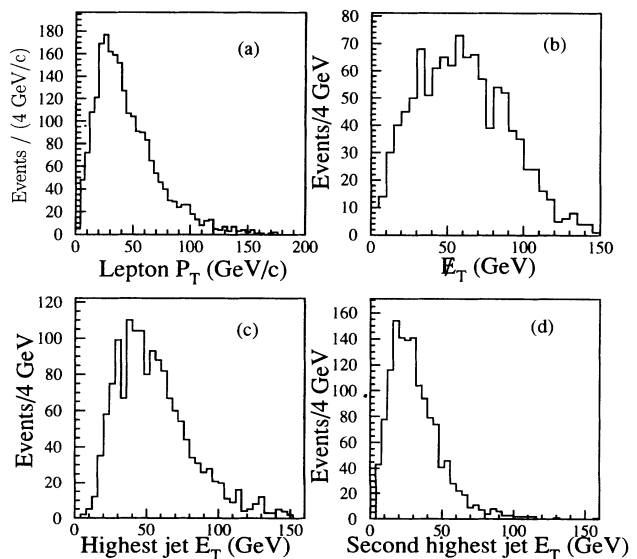

FIG. 5. Monte Carlo distributions for $M_{\text{top}} = 160$ GeV/c^2. (a) Lepton P_T spectrum from $t \to W \to l$. (b) $\not\!\!E_T$ for events with two leptons with $P_T > 20$ GeV/c. (c) Leading-jet E_T for dilepton events. (d) Next-to-leading jet E_T for dilepton events.

tributions for $t\bar{t}$ Monte Carlo events.

For M_{top} in the range 90–180 GeV/c^2, about 80% of the dilepton acceptance after selection cuts comes from the case where each W decays to an electron or muon. However, it is also possible for one or both of the leptons to come from the decay of a b quark, or for one or both of the W bosons to decay to a τ, which subsequently decays to an electron or muon. Such cases are included in the acceptance.

A P_T threshold of 20 GeV/c for each lepton has been chosen to preserve a large portion of the top signal, while suppressing the backgrounds from $b\bar{b}, Z \rightarrow \tau\tau$ decays, and from lepton misidentification. In Secs. III B and III C we discussed electron and muon selection, and both strict and loose criteria to select central leptons were defined. We require each event to have at least one central lepton passing the strict cuts. This gives better efficiency than applying strict criteria on both leptons and still provides good background rejection. At least one central lepton in each event must pass a track isolation cut $I_{\text{trk}} < 3$ GeV/c, where I_{trk} is the sum of P_T over all other tracks in a cone of $R = 0.25$ centered on the lepton track. This cut reduces backgrounds from lepton misidentification and from $b\bar{b}$.

We require the two leptons to have opposite electric charge. Same-charge lepton pairs from $t\bar{t}$ must include one lepton from b decay. Since these leptons tend to have lower P_T and to be nonisolated (i.e., accompanied by nearby particles from the b hadronization and decay), they are less likely to pass the momentum and lepton identification cuts. The opposite-charge requirement reduces the dilepton signal from $t\bar{t}$ by less than 6% for M_{top} between 90 and 180 GeV/c^2, while reducing backgrounds from lepton misidentification by a factor of 2.

After the P_T, lepton identification, isolation, and opposite-charge cuts, there are 5 $e\mu$, 685 ee, and 571 $\mu\mu$ events. Further kinematic and event topology cuts are applied to reduce the remaining backgrounds. Dielectron and dimuon backgrounds from Z decay are rejected with a dilepton invariant mass (M_{ll}) cut around the Z peak. We remove ee and $\mu\mu$ events with $75 < M_{ll} < 105$ GeV/c^2. Figure 6 shows the invariant mass distribution for the 1256 ee and $\mu\mu$ data events, and for top Monte Carlo simulation. For $M_{\text{top}} = 160$ GeV/c^2, 80% of dielectron and dimuon events from $t\bar{t}$ are expected to pass the invariant mass cut. After the invariant mass cut there are
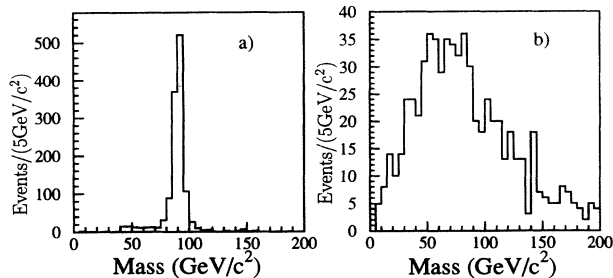

FIG. 6. Dilepton invariant mass distributions. (a) Dielectron and dimuon data. (b) Monte Carlo simulation for $M_{\text{top}} = 160$ GeV/c^2 (unnormalized).

58 ee and 62 $\mu\mu$ events in the data.

At this stage of the selection, ee and $\mu\mu$ backgrounds are expected to be dominated by Drell-Yan events. For the $e\mu$ channel, most of the expected backgrounds are from $Z \rightarrow \tau\tau$, $b\bar{b}$, and lepton misidentification. These backgrounds are rarely expected to have significant E_T; therefore, we require events to have $E_T > 25$ GeV. For Drell-Yan events, where high-P_T neutrinos are not expected, E_T can arise from biases and fluctuations in the jet energy measurement. To improve the rejection against this background, we calculate the E_T after making jet energy corrections, which take into account cracks between detector components and nonlinear calorimeter response.

In addition to the cut on the magnitude of E_T, we also place a cut on its direction in order to reduce backgrounds from the Drell-Yan continuum (outside the Z peak) and from $Z \rightarrow \tau\tau$. These cuts are also effective in reducing backgrounds from lepton misidentification and from $b\bar{b}$. Nonuniformities in the calorimeter cause asymmetric, non-Gaussian tails in the corrected jet response. Most Drell-Yan events with large E_T, near or above the 25 GeV threshold, contain a jet with corrected energy that has fluctuated below (rather than above) the true parton energy. In such cases the E_T direction is nearly aligned with the jet direction. For events with $E_T < 50$ GeV, we require $\Delta\phi(E_T, j) > 20°$, where $\Delta\phi(E_T, j)$ is the azimuthal angle between the direction of E_T and the direction of the nearest jet. Jets considered here must be in the central or plug calorimeters ($|\eta| < 2.4$) and have uncorrected $E_T > 10$ GeV. The E_T magnitude and direction requirements were chosen to achieve good rejection in a Drell-Yan control sample of Z+jet events. The distributions of $\Delta\phi(E_T, j)$ vs E_T for the Z+jet samples are shown in Fig. 7, together with the prediction for $t\bar{t}$ Monte Carlo events.

A similar cut, rejecting events where the E_T points along the direction of one of the leptons, reduces background from $Z \rightarrow \tau\tau$. The large E_t in these cases comes from energetic neutrinos from a $\tau \rightarrow l\nu\nu$ decay. For events with $E_T < 50$ GeV, we require $\Delta\phi(E_T, l) > 20°$, where $\Delta\phi(E_T, l)$ is the azimuthal angle between the direction of E_T and the direction of the nearest lepton. The distribution of $\Delta\phi(E_T, l)$ vs E_T for a $Z \rightarrow \tau\tau$ simulation is shown in Fig. 8 together with the prediction for top Monte Carlo events. The distribution of the smallest angle between E_T and the closest lepton or jet vs E_T is shown in Fig. 9 for the 120 ee and $\mu\mu$ events passing the invariant mass cut, for the 5 $e\mu$ events, and for top Monte Carlo simulation. The E_T magnitude and direction cuts are 76% efficient for $M_{\text{top}} = 160$ GeV/c^2. After these cuts, there are no ee or $\mu\mu$ events remaining. Two $e\mu$ events survive.

For high mass top events, the two b quarks can deposit considerable energy in the calorimeters. A better separation between signal and backgrounds can be obtained by requiring two jets in the central or plug calorimeters ($|\eta| < 2.4$) with uncorrected calorimeter transverse energies $E_T > 10$ GeV. The two-jet requirement is expected to reduce backgrounds by a factor of 4 (see Sec. IV C), while
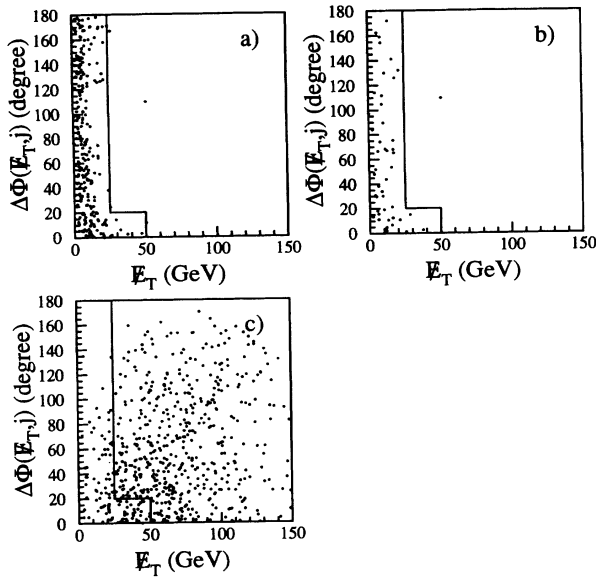
FIG. 7. Distributions of the azimuthal angle between $\not{E}_T$ and the closest jet vs $\not{E}_T$. (a) Dielectron and dimuon data from a Drell-Yan control sample of $Z + \geq 1$ jet events. (b) Dielectron and dimuon data from a Drell-Yan control sample of $Z + \geq 2$ jet events. (c) Monte Carlo simulation for $M_{\text{top}} = 160$ GeV/c^2 (unnormalized). The boundary in the figures separates signal and background.
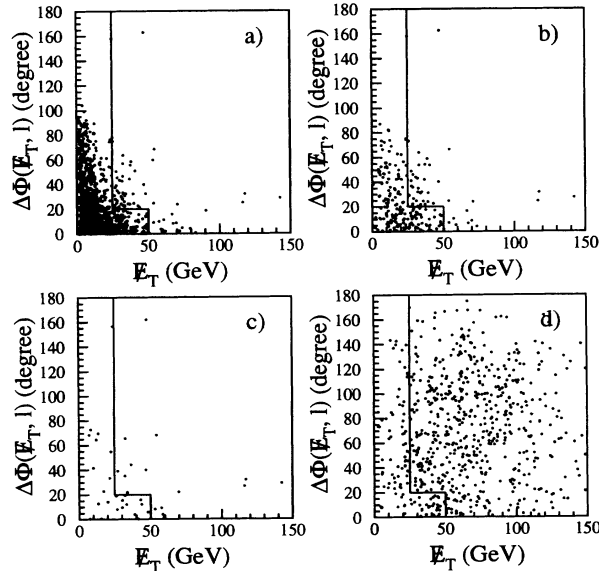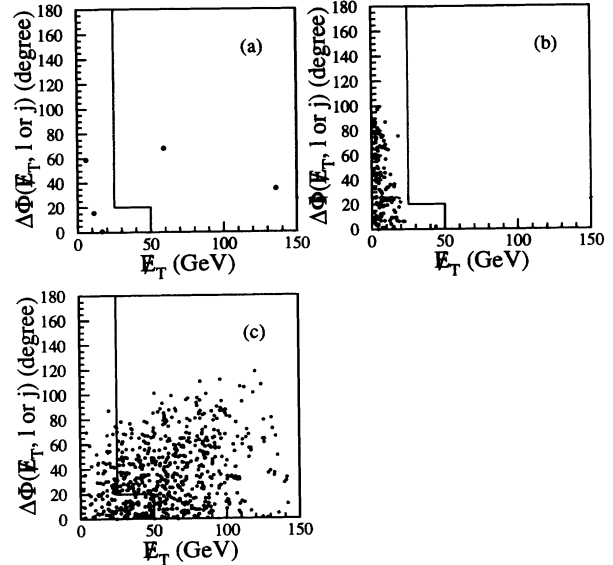

FIG. 8. Distributions of the azimuthal angle between $\not{E}_T$ and the closest lepton vs $\not{E}_T$. (a) $Z \to \tau\tau$ simulation, all jet multiplicities. (b) $Z \to \tau\tau$ simulation with ≥ 1 jet. (c) $Z \to \tau\tau$ simulation with ≥ 2 jets. (d) Monte Carlo events for $M_{\text{top}} = 160$ GeV/c^2 (unnormalized). The boundary in the figures separates signal and background.

FIG. 9. Distributions of the azimuthal angle between $\not{E}_T$ and the closest lepton or jet vs $\not{E}_T$. (a) $e\mu$ data. (b) Dielectron and dimuon data after the invariant mass cut. (c) Monte Carlo events for $M_{\text{top}} = 160$ GeV/c^2 (unnormalized). Events in the region to the left of the boundary in the figures are rejected by the $\not{E}_T$ cuts.

preserving 84% of the signal for $M_{\text{top}} = 160$ GeV/c^2. Both $e\mu$ events survive the two-jet cut.

A summary of the numbers of events surviving different stages of cuts is presented in Table VI. The characteristics of the two $e\mu$ events in the $t\bar{t}$ signal region are shown in Table VII. We have applied the b-tagging algorithms of Sec. V to these events, and find that the first event has a jet (jet 1 in event I in Table VII) with both a displaced-vertex tag and a soft muon (with $P_T = 8.8$ GeV/c) tag. We find no b tags in the second $e\mu$ event. A discussion of b tagging in dilepton events is presented in Sec. VI B. Figure 10 is an event display for event I, showing the observed calorimeter energy, the reconstructed CTC tracks, and the SVX tracks, which show a displaced vertex.

B. Event selection efficiencies

We define the total dilepton efficiency, ϵ_{total}, by the relation $\epsilon_{\text{DIL}} = \text{Br}\epsilon_{\text{total}}$, where ϵ_{dil} is the fraction of all $t\bar{t}$ events that pass the dilepton selection criteria. The

TABLE VI. Number of data events surviving consecutive requirements.

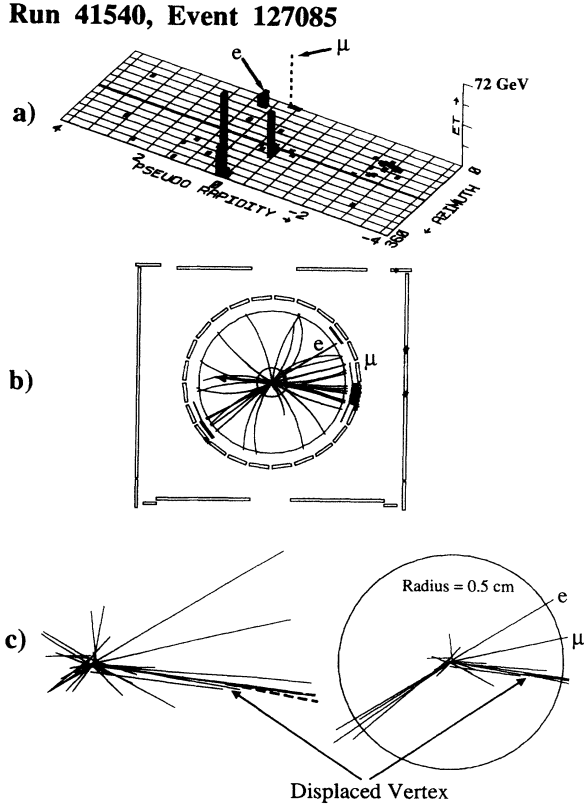| Cut	e_μ	ee	$\mu\mu$
P_T	8	702	588
Opposite charge	6	695	583
Isolation	5	685	571
Invariant mass	5	58	62
$\not{E}_T$ magnitude	2	0	1
$\not{E}_T$ direction	2	0	0
Two jet	2	0	0

Run 41540, Event 127085

FIG. 10. Event display for one of the $e\mu$ events; (a) displays the observed calorimeter E_T in the η-ϕ plane, (b) shows the reconstructed CTC tracks and muon hits in the r-ϕ plane, and (c) shows a similar display for the reconstructed SVX tracks. The jet with the displaced vertex is enlarged on the right half of (c). Extraneous tracks have been removed from the enlargement. Dashed tracks in the enlargment form the displaced vertex. The track lengths in the complete SVX display are proportional to their P_T.

branching ratio, Br, which has a value of $\frac{4}{81}$, is the semileptonic branching fraction of the W^+ and the W^- decaying into $e\mu$, ee, and $\mu\mu$. After all cuts, most of the signal comes from dileptons from W^+W^-, therefore ϵ_{total} corresponds closely to the fraction of W^+W^- dileptons that pass all cuts.

The total detection efficiency for the dilepton search is decomposed into several parts and written as $\epsilon_{\text{total}} = \epsilon_{\text{geom }P_T}\epsilon_{\text{ID}}\epsilon_{\text{isol}}\epsilon_{\text{topology}}\epsilon_{\text{two jet}}\epsilon_{\text{trigger}}$. These efficiencies were computed in the order listed and are shown as a function of top mass in Table VIII and Fig. 11. We use the ISAJET [23] Monte Carlo event generator and CDF detector simulation programs to determine the geometric and kinematic acceptance, $\epsilon_{\text{geom }P_T}$, which is the fraction of all $t\bar{t}$ events having two fiducial leptons with $P_T > 20$ GeV/c, divided by the constant Br. We note that $\epsilon_{\text{geom }P_T}$ is increasing with top mass because the leptons are more likely to be in the central region and have large momentum at higher top mass. In particular, the contribution to the geometric and kinematic acceptance from events with one or more leptons from b decay is increasing, from about 24% at $M_{\text{top}} = 120$ GeV/c^2 to 46% at $M_{\text{top}} = 160$ GeV/c^2.

We also use the Monte Carlo simulation to determine the efficiency of the lepton identification cuts, ϵ_{ID}, the efficiency of the lepton isolation cuts, ϵ_{isol}, the combined efficiency of the dilepton charge, invariant mass, and E_T cuts, $\epsilon_{\text{topology}}$, and the efficiency of the two-jet cut, $\epsilon_{\text{two jet}}$. We have verified that the Monte Carlo simulation reproduces the lepton identification efficiencies observed in $Z \rightarrow ee, \mu\mu$ events. Since leptons from b decay can overlap with other particles from the b fragmentation and decay, they are identified with less efficiency than those from W decay. Since the P_T of the b quarks increases with increasing top mass, so does the average P_T of the b fragmentation products and the P_T of leptons from semileptonic b decays. Because of the higher P_T of the leptons from the semileptonic decays, the fraction of leptons

TABLE VII. Characteristics of the two $e\mu$ events. The jet calorimeter energies have been corrected to estimate the original parton energies. Jets 1 and 2 have been treated as bottom-quark jets; jets 3 were treated as generic jets (no specific flavor assumed). The jet energy calibrations are discussed in Sec. IX. The jet energy corrections have also been included in the E_T calculation.

| | Event I Run 41540 event 127085 | | | | Event II Run 47122 event 38382 | | | |
	Charge	P_T (GeV/c)	η	ϕ (deg)	Charge	P_T (GeV/c)	η	ϕ (deg)
Electron	−	22.0	0.84	32	+	50.6	0.93	25
Muon	+	47.5	0.17	14	−	37.3	−0.74	4
Muon	+	8.8	0.18	352				
Jet 1		131	0.11	352		85	0.64	218
Jet 2		61	−0.54	215		26	1.34	344
Jet 3		26	−2.94	112		18	−3.31	344
E_T		136		179		60		149
$\Delta\phi(E_T, l)$				147				124
$\Delta\phi(E_T, j)$				36				68

TABLE VIII. Dilepton detection efficiencies.

M_{top}	$\epsilon_{geom\ P_T}$	ϵ_{ID}	ϵ_{Isol}	$\epsilon_{topology}$	$\epsilon_{trigger}$	$\epsilon_{two\ jet}$	ϵ_{total}
100	0.34	0.68	0.96	0.66	0.97	0.33	0.045±0.017
120	0.42	0.63	0.96	0.66	0.97	0.63	0.100±0.015
140	0.55	0.53	0.95	0.69	0.97	0.75	0.134±0.013
160	0.63	0.48	0.95	0.69	0.98	0.84	0.157±0.014
180	0.74	0.43	0.96	0.66	0.97	0.88	0.173±0.015

that pass the geometry and P_T requirements, which come from b decays increases with top mass. However, the higher P_T of the fragmentation products results in a decreasing efficiency for finding these same leptons due to the implicit lepton isolation required by the lepton selection (i.e., E_{had}/E_{EM} for electrons, E_{had} for muons). Therefore, $\epsilon_{geom\ P_T}$ increases with increasing top mass, while ϵ_{ID} decreases with top mass. The trigger efficiencies $\epsilon_{trigger}$ are determined using data collected by independent triggers.

The fractional uncertainty in ϵ_{total} varies from 38% to 9% for M_{top} in the range 100–180 GeV/c^2 (see Table VIII). For low-mass top events, the observed jets originate frequently from initial-state gluon radiation, rather than from b quarks. The b quarks from low-mass top decay are produced near threshold and are detected as calorimeter jets with low efficiency. The uncertainty in the efficiency of the two-jet requirement, mostly due to the limited understanding of initial-state gluon radiation, decreases from 36% for $M_{top} = 100$ GeV/c^2 to 3% for $M_{top} = 180$ GeV/c^2. We compared the efficiency of the two-jet requirement in our ISAJET sample, with that ob-

tained when the effect of gluon radiation was disabled in ISAJET. Half the difference between these efficiencies was taken as the systematic uncertainty in the efficiency of the two-jet cut. The average agrees well with results from the HERWIG Monte Carlo program, and is our best estimate of the efficiency of the two-jet requirement.

Other uncertainties in the detection efficiency have a small dependence on M_{top}, and come from the lepton identification cuts (6%), lepton isolation cuts (2%), E_T cuts (2%, estimated by changing the jet energy scale within ±10%, see Sec. III D), structure functions (2%), and Monte Carlo statistics (3%). The efficiencies and yields are listed as a function of top mass in Tables VIII and IX. The contributions to the top dilepton sensitivity after all cuts are expected to be 59% for $e\mu$, 21% for ee, and 20% for $\mu\mu$, approximately independent of M_{top}.

C. Dilepton backgrounds

The backgrounds in the dilepton channel are listed in Table X for various stages of the dilepton selection. The first column contains the background estimates after the P_T, opposite-charge, isolation, and invariant mass cuts are applied. The second column shows the backgrounds after the E_T cut is included; these are the cuts for a relatively low-mass top search. The third column is for the final selection, designed for high mass top, which includes a two-jet requirement. In what follows, we describe the methods used to estimate the different sources of background.

Dilepton backgrounds from WW production are determined using the ISAJET Monte Carlo program, normalized to a total WW cross section of 9.5 pb [29]. The dilepton topology of WW events is very similar to that of $t\bar{t}$ events, but WW events are expected to have less jet activity. Before jet cuts, we expect 1.17±0.37 dilepton events from WW. The error is dominated by a theoreti-
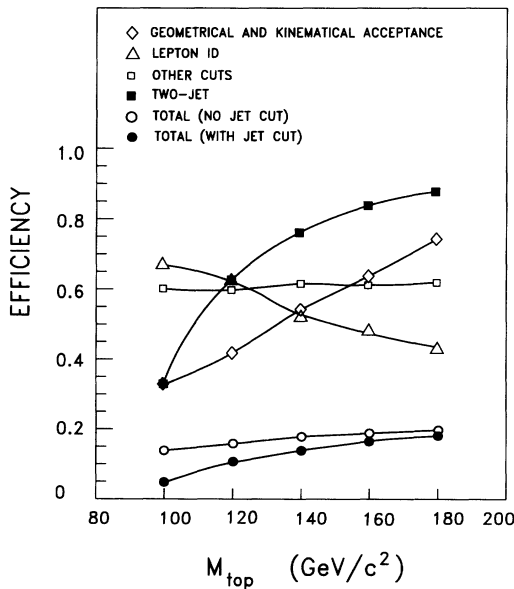

FIG. 11. Efficiencies of the dilepton selection as a function of M_{top}. "Other cuts" corresponds to the combined efficiency for the isolation, topology (opposite charge, mass, E_T) and trigger requirements.

TABLE IX. Detection efficiencies, $\epsilon_{dil} = Br\epsilon_{total}$, the predicted central value of $t\bar{t}$ production cross section from Ref. [10] and the number of events expected in 19.3 pb^{-1}, as functions of top mass.

M_{top} GeV/c^2	ϵ_{dil}	$\sigma_{t\bar{t}}$ (pb)	$N_{e\mu}$ (events)	$N_{e\mu,ee,\mu\mu}$ (events)
120	0.0049	38.9	2.2	3.7
140	0.0066	16.9	1.3	2.2
160	0.0078	8.2	0.8	1.3
180	0.0086	4.2	0.4	0.7

TABLE X. Number of background events expected in 19.3 pb^{-1} and the number of events observed in the data.

		Without $\not{E}_T$ and two-jet cuts	Without two-jet cut	All cuts
$e\mu$	WW	1.1	0.74	0.10 ± 0.04
	$Z\to\tau\tau$	3.7	0.22	0.07 ± 0.02
	$b\bar{b}$	1.2	0.10	0.04 ± 0.03
	Fake	1.2	0.19	0.03 ± 0.03
	Total background	7.2	1.25	0.24 ± 0.06
	CDF data	5	2	2
$ee,\mu\mu$	WW	0.6	0.43	0.06 ± 0.02
	$Z\to\tau\tau$	3.0	0.20	0.06 ± 0.02
	$b\bar{b}$	1.6	0.12	0.05 ± 0.03
	Fake	1.7	0.25	0.04 ± 0.03
	Drell-Yan	113	0.28	$0.10^{+0.23}_{-0.08}$
	Total background	120	1.28	$0.31^{+0.24}_{-0.10}$
	CDF data	120	0	0

cal uncertainty of 30% in the cross section.

Only 13% of WW events pass the two-jet cut. To check the ISAJET prescription for gluon radiation, we also studied an independent process, namely, Drell-Yan production at large invariant masses. Since both the high-mass Drell-Yan and WW processes are dominated by quark-antiquark initial-state contributions, their initial-state radiation spectra are expected to be similar for a given subprocess invariant mass. We performed a calculation using the exact Drell-Yan + 2 jet matrix elements [30], and found the efficiency of the two-jet cut to be approximately 2.7 times higher at typical WW subprocess invariant masses of 300 GeV/c^2 than at Z subprocess masses, which are around 100 GeV/c^2. In Z data we find that $4.1\pm0.6\%$ of the events have two jets above 10 GeV. Therefore, an alternative estimate of the fraction of events passing the two-jet cut in WW events is 11% (i.e., $2.7\times4.1\%$). Since there is good agreement with ISAJET, we use a two-jet cut efficiency of $13\pm4\%$, corresponding to the ISAJET central value, with an assigned systematic uncertainty of 30%. The total background from WW, after all cuts, is 0.16 ± 0.06 events.

Backgrounds from $Z\to\tau\tau\to e\mu$, ee, or $\mu\mu$ are studied using a data sample of $Z\to ee$ events and replacing each electron by a simulated τ that decays into e or μ. From this sample we obtain reliable rejection factors for the topology cuts (M_{ll}, $\not{E}_T$, two jet). The geometrical and kinematic acceptance together with the efficiency of the lepton identification cuts are obtained from an ISAJET Monte Carlo sample with detector simulation. The $Z\to\tau\tau$ cross section is set to the measured value for $Z\to ee$ [17]. We expect 0.42 ± 0.08 dilepton events from $Z\to\tau\tau$ after the lepton P_T, isolation, M_{ll}, and $\not{E}_T$ cuts, and 0.13 ± 0.04 events after the two-jet cut.

Heavy-flavor backgrounds, mostly $b\bar{b}$, have been studied using ISAJET [23] to model the production processes, and the CLEO Monte Carlo program [24] to model b-quark decay. Next-to-leading-order production processes such as gluon splitting and flavor excitation, as well as

the direct production of heavy flavor (b,c) quark-antiquark pairs, are included. To normalize the ISAJET predictions, we compare the yields of lower momentum $e\mu$ data events, with P_T thresholds of 15 GeV/c and 5 GeV/c on the first and second leptons, respectively, with the number of such events found in the Monte Carlo sample. The low-momentum $e\mu$ data sample is dominated by dileptons from heavy flavor [31], with other sources (mostly lepton misidentification) comprising $20\pm20\%$. We obtain a normalization factor (ratio of data to Monte Carlo rates) of 1.04 ± 0.21. A comparison of the low-momentum $e\mu$ data with Monte Carlo events is shown in Fig. 12 for several distributions. The rejection factors for the P_T and topology cuts are extracted from the Monte Carlo sample. We expect 0.22 ± 0.11 $b\bar{b}$ events after all cuts except for the two-jet requirement, and 0.10 ± 0.06 events after the imposition of the two-jet cut.

Events from QCD multijet or W+jet processes, with at least one misidentified lepton, conversion electron, or muon from hadron decay in flight, can mimic the $t\bar{t}$ signature and are referred to as "fake dilepton" backgrounds. Backgrounds from lepton misidentification are estimated by measuring the probabilities for tracks or calorimeter energy clusters from a jet sample, collected with a 20-GeV (transverse energy) threshold jet trigger, to satisfy muon or electron identification cuts. The fake probabilities are then applied to the number of events in the data with a lepton together with an additional track or cluster. The fake rates from the jet sample include an admixture of leptons from semileptonic decays of b and c quarks. Due to the long lifetime of heavy quarks, their daughter leptons have a track impact-parameter distribution that can be distinguished with the SVX from that of tracks from the primary interaction. We subtract the b and c contribution from the fake rates in order to avoid double counting $Wb\bar{b}$ and $b\bar{b}$ contributions, which are estimated separately. Subtraction of the b and c decay contribution from the fake rates lowers the expected background by $20\pm20\%$. The fake dilepton background is
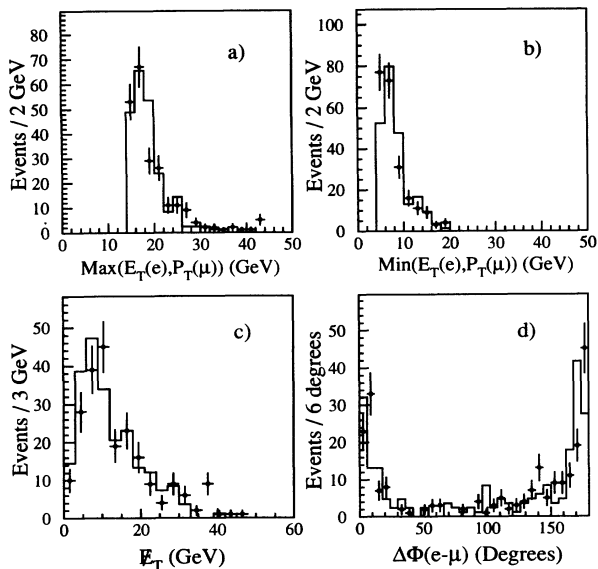
FIG. 12. Distributions for $e\mu$ data with $P_T^{l_1} > 15$ GeV/c and $P_T^{l_2} > 5$ GeV/c (points) compared to expectations from the ISAJET Monte Carlo simulation (histograms). (a) P_T spectrum of the leading lepton. (b) P_T spectrum of the second lepton. (c) E_T distribution. (d) Dilepton azimuthal angular separation.

0.44±0.29 events and 0.07±0.05 events before and after the two-jet cut, respectively.

Backgrounds from fakes are expected to yield as many same-charge as opposite-charge dilepton events. Including the effect of $B^0\bar{B}^0$ mixing [31], we expect the number of same-charge $b\bar{b}$ events to be 35±7 % of the number of opposite-charge $b\bar{b}$ events. As a check of the sum of our $b\bar{b}$ and fake background estimates, we can predict the number of same-charge events expected in the dilepton sample. In order to get better statistics for the comparison, we lowered the P_T threshold on both leptons to 15 GeV/c. After this P_T cut and isolation cuts, we predict 19.8±4.0 same-charge dilepton events (11.4±3.2 from fakes, and 8.4±2.4 from $b\bar{b}$), and observe 10 such events in the data. This may indicate that our estimate for the sum of $b\bar{b}$ and fake backgrounds is an overestimate.

The $t\bar{t}$ signature can also be mimicked by dilepton final states of Drell-Yan events ($\gamma/Z \to ee, \mu\mu$). We explicitly remove 1136 Z events with dilepton invariant mass between 75 and 105 GeV/c^2. In the continuum outside this window, there are 120 events. We have used the ISAJET rate of Drell-Yan events outside the Z window relative to that inside the Z window, together with the actual number of Z events in the data, to predict 113 events from the continuum. Together with a small contamination predicted from other backgrounds (see Table X), this agrees well with the observed dielectron and dimuon rates.

To estimate the background from the continuum after the E_T and jet requirements, a rejection factor for these cuts was obtained from the Z events and applied to the Drell-Yan events outside the Z window. The jet activity and $P_T(\gamma/Z)$ are expected to increase slightly with increasing dilepton invariant mass. Most of the dilepton events outside the Z window have low invariant mass (see

Fig. 6). Therefore, the E_T and jet cut rejection obtained from Z events was corrected (increased) to account for the lower average jet activity in the continuum. We calculated this correction to be 13%, using the exact Drell-Yan + 2 jet matrix elements [30].

Approximately 0.3% of Z events (three events) pass the E_T cuts, and 0.1% [based on the single event in Fig. 7(b)] pass an additional two-jet requirement. When scaling the events outside the Z window according to these fractions, we obtain an expected Drell-Yan background of 0.28±0.17 events after the E_T cuts, and $0.10^{+0.23}_{-0.08}$ events in the signal region after the two-jet requirement. The Drell-Yan background in the signal region is based on one $Z \to \mu\mu$ candidate event with large E_T and two jets. We expect 0.1 top ee or $\mu\mu$ events with mass in the Z window for $M_{\text{top}} = 160$ GeV/c^2. If the event were not a Z event, but $t\bar{t}$, then the Drell-Yan background could be smaller than our calculated value, although covered by the uncertainties quoted. We note that one of the jets in the event is tagged as a b quark with the displaced vertex algorithm described in Sec. V B.

As an overall check of the reliability of our background calculations, we have used the sample with lepton P_T thresholds lowered to 15 GeV/c, and have compared our predictions for the $e\mu$ channel with the number of events observed in the data after isolation cuts. With this lower threshold Drell-Yan backgrounds dominate the ee and $\mu\mu$ channels. By restricting the comparison to the $e\mu$ channel, we can test our predictions for the sum of non-Drell-Yan backgrounds, which constitute 88 (82) % of the total dilepton background before (after) the two-jet cut. Our prediction is 25±3 $e\mu$ background events, to be compared with 18 such events observed in the data. The breakdown for the different background sources is shown in Table XI.

We have also studied other background sources to the top signal region, such as WZ [32], and ZZ [33], $Wb\bar{b}$ [25], and $Z \to b\bar{b}$ [23] and have found them to be negligible. In summary, for the low mass top selection, without the two-jet cut, we expect 2.5±0.5 background events, and we observe two events in the data. Adding the final two-jet requirement, appropriate for a high-mass top search, we expect $0.56^{+0.25}_{-0.13}$ background events, and we observe two dilepton events in the data.

TABLE XI. Number of $e\mu$ background events expected in 19.3 pb^{-1} and the number of $e\mu$ events observed in the data. For this comparison, the lepton P_T threshold was lowered to 15 GeV/c.

	$P_T > 15$ GeV/c	Without E_T and two-jet cuts
$e\mu$	WW	1.2±0.4
	$Z \to \tau\tau$	8.3±0.5
	$b\bar{b}$	10±2
	Fake	5.9±1.8
	Total background	25±3
	CDF data	18

D. Low-mass top search and limits on top production

In a previous publication [34], based on a data sample of 4.1 pb^{-1} collected by CDF in 1988–1989, we presented a lower limit of 85 GeV/c^2 on M_{top} from the dilepton channel alone. When combined with the results from the lepton + jets + b channel, where the b was tagged through its semileptonic decay into muons, an improved limit of 91 GeV/c^2 at the 95% confidence level was obtained [34].

In the dilepton search with the two-jet cut and in the lepton + jets search described in Sec. V, we concentrate on top masses in the range 120 GeV/c^2 and above where the event selection is reasonably efficient. This leaves a hole between our previously published mass limit of 91 and 120 GeV/c^2, where these analyses begin. In order to fill this gap, we extract a new limit using the 19.3 pb^{-1} data sample from 1992–1993 and 3.7 pb^{-1} from 1988–1989 (this is the 4.1 pb^{-1} reported in Ref. [34], rescaled to the new σ_{BBC} from Sec. II). First it must be noted that for top masses close to the previous lower limit of 91 GeV/c^2, the b quarks are produced near threshold and, hence, most $t\bar{t}$ dilepton events will not have two observable jets above 10 GeV in the calorimeter. For a search in this low-mass region we must remove the two-jet requirement. When the two-jet cut is removed (see Table VI) no new events in addition to the two $e\mu$ signal region events appear in the 1992–1993 data. With these same cuts, there are no events found in the 1988–1989 data sample. The 1988–1989 $e\mu$ event of Ref. [34] fails the $E_T > 25$ GeV cut added to the $e\mu$ channel in the 1992–1993 analysis to reduce backgrounds expected in the larger data sample. The total background expected without the two-jet requirement in the combined data samples is 3.0±0.6 events.

We make the conservative assumption that the background fluctuated to zero in our dilepton data sample. Then we can obtain an upper limit on the $t\bar{t}$ cross section assuming that the two observed $e\mu$ events are from the signal (no background subtraction), as follows:

$$\sigma_{t\bar{t}}(95\% \text{ C.L.}) = \frac{N_{dil}(95\% \text{ C.L.})}{\int \mathcal{L}\, dt\, \epsilon_{dil}}, \quad (1)$$

where $N_{dil}(95\%$ C.L.) is the upper limit at the 95% confidence level on the number of top dilepton events, $\int \mathcal{L}\, dt$ is the integrated luminosity and $\epsilon_{dil} = \text{Br}\epsilon_{total}$ is the detection efficiency of the analysis for observing top events. In Table XII we show our results for the upper limit on $\sigma_{t\bar{t}}$, as a function of top mass, for the combined 1988–1989 and 1992–1993 data samples with $\int \mathcal{L}\, dt = 23.0 \pm 0.8$ pb^{-1}. A lower limit on the top quark mass is obtained by finding the intersection of our measured upper limit on the cross section as a function of top mass with theoretical lower estimates of $\sigma_{t\bar{t}}$ (see Fig. 13). We use the cross-section calculation, at the next-to-next-to-leading order, from Ref. [10]. From the 1992–1993 dilepton data alone, the limit is 113 GeV/c^2 at the 95% C.L. When combining the 1988–1989 and 1992–1993 dilepton data samples, we obtain the result $M_{top} > 118$ GeV/c^2 at the 95% C.L.

TABLE XII. Detection efficiencies with the two-jet cut removed and upper limit on $\sigma_{t\bar{t}}$ as functions of top mass.

M_{top} GeV/c^2	ϵ_{dil} no jet cut	$\sigma_{t\bar{t}}$ (pb) 95% C.L.
100	0.0068±0.0005	41.6
120	0.0078±0.0006	36.2
140	0.0088±0.0007	32.0
160	0.0093±0.0007	30.6

E. Summary of dilepton analysis

We have searched for events with two high-P_T leptons, large E_T, and two hadronic jets, as a possible manifestation of the production and decay of top-quark pairs with large M_{top}, above approximately 120 GeV/c^2. A signal of 3.7 (0.7) $t\bar{t}$ dilepton events is expected for $M_{top} = 120$ (180) GeV/c^2. In the $e\mu$ channel, two $t\bar{t}$ candidate events were observed. No ee or $\mu\mu$ events were found in the signal region. A total $0.56^{+0.25}_{-0.13}$ events is expected from background sources in the dilepton channels. This small excess of dilepton events is combined in Sec. VI with the results of the lepton + jets analysis described in Sec. V.

We have also carried out a search for lower mass top, by removing the two-jet requirement, which is only efficient at high masses. No additional dilepton events were found. Under the assumption that the two events are from signal, that is, without subtracting backgrounds, we measured the upper limits on the $t\bar{t}$ production cross section presented in Table XII. When these upper limits are compared with current theoretical calculations of $\sigma_{t\bar{t}}$ [10], we derive a lower limit on the top-quark mass, $M_{top} > 118$ GeV/c^2 at the 95% C.L.

V. SEARCH FOR $t\bar{t}$ IN THE LEPTON + JETS MODE

This section reports on the search for $t\bar{t}$ events in which one of the W bosons has decayed either to an $e\nu$ or
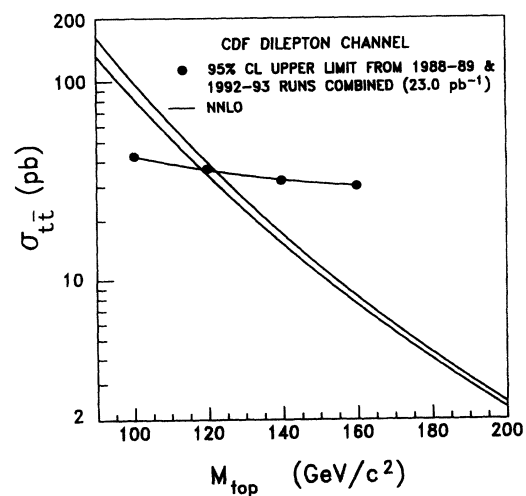

FIG. 13. The upper limit at the 95% C.L. on $\sigma_{t\bar{t}}$, overlaid with the theoretical lower bound and central value of a next to next to leading order (NNLO) calculation from Ref. [10].

TABLE XIII. The number of events passing various consecutive selection criteria in data. The good lepton requirement includes all quality selection, fiducial requirements, E_T cuts, and conversion removal.

Selection criteria	Electrons	Muons
Good lepton	28 522	17 994
Lepton isolation requirement	20 420	11 901
Z removal	18 700	11 310
$E_T > 20$ GeV	13 657	8 724
Good quality run	12 797	8 272
Trigger requirement	11 949	7 024

TABLE XIV. Summary of W candidate event yields as a function of observed jet multiplicity for electron and muon decay modes of the W. Each jet must have $E_T \geq 15$ GeV and $|\eta| \leq 2.0$.

Jet multiplicity	Electron events	Muon events
0 jet	10 663	6 264
1 jet	1 058	655
2 jets	191	90
3 jets	30	13
≥ 4 jets	7	2

a $\mu\nu$ pair, and the other W has decayed to quarks, giving rise to jets. This is the lepton + jets decay mode described in Sec. I. We first report on the selection of $W \rightarrow e\nu$ and $\mu\nu$ candidate events, and present the yield as a function of the number of jets observed in the event. We then show that requiring significant jet activity greatly increases the $t\bar{t}$ signal-to-background ratio. To suppress further the W+multijet background, we search for b quarks using two different methods of b tagging. The first, described in Sec. V B, uses SVX tracking information to search for displaced vertices. The second method searches for leptons from b-quark decay and is described in Sec. V C.

A. Inclusive W + jets selection

The W selection requires an isolated electron (muon) to pass the standard trigger and offline lepton identification outlined in Sec. III, and also to have $E_T \geq 20$ GeV ($P_T \geq 20$ GeV/c). We require the event z vertex position to be within 60 cm of the center of the CDF detector. We additionally require $E_T \geq 20$ GeV. Events containing Z bosons are removed from the sample by rejecting events with an oppositely charged dilepton (ee or $\mu\mu$) invariant mass in the range 70 to 110 GeV/c^2. Table XIII lists the number of events passing consecutive selection criteria. After all cuts, a total of 11 949 electron and 7024 muon events remain. Figure 14 shows the lepton-E_T transverse mass distribution for the electron and muon samples. A clear Jacobian peak is observed at the W mass. Defining a jet as a cluster (see Sec. III D) with $|\eta| \leq 2.0$ and $E_T \geq 15$ GeV, we bin the W candidate
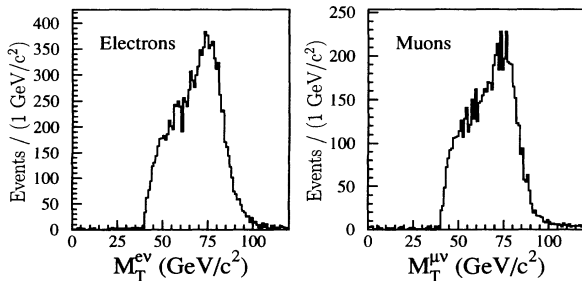
events according to their observed jet multiplicity (N_{jet}). Since the goal is simply to count clusters above a threshold, the E_T of these jets is not corrected for detector cracks, nonlinearities and other effects. The N_{jet} distributions are shown separately for electron and muon events in Table XIV, where it can be seen that the W+multijet cross section falls quickly with jet multiplicity [35].

Figure 15(a) shows the E_T distributions for $t\bar{t}$ Monte Carlo events generated with $M_{top} = 120$ and 180 GeV/c^2, and required to have a 20-GeV electron passing the electron selection criteria. The 20-GeV E_T cut is necessary to reduce backgrounds from misidentified leptons in QCD-jet events and semileptonic decays in $b\bar{b}$ events. This requirement is approximately 90% efficient for top events, and shows little sensitivity to variations in the top mass. Figure 15(b) shows the jet multiplicity calculated from a $t\bar{t}$ Monte Carlo program with top masses of 120 and 180 GeV/c^2. While, in principle, one might expect to observe one jet for each quark in the final-state of a $t\bar{t}$
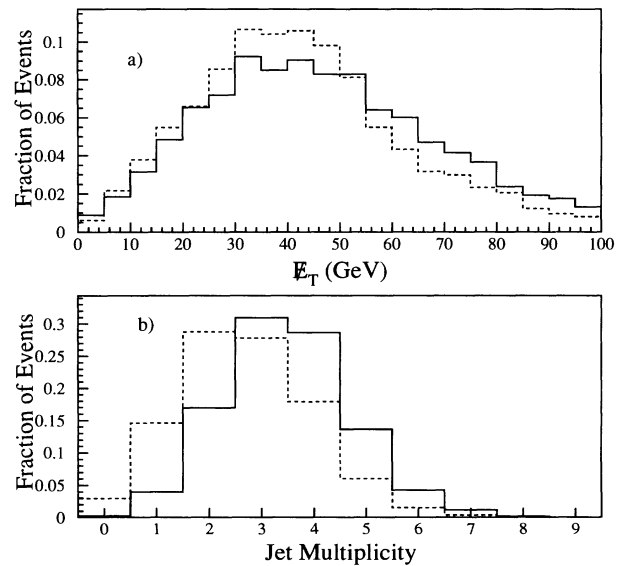

FIG. 15. The $t\bar{t}$ Monte Carlo distribution of (a) E_T for events with a 20-GeV electron passing electron identification cuts, and (b) the expected jet multiplicity distribution for events passing the W selection criteria. In both plots the dashed line is for $M_{top} = 120$ GeV/c^2 and the solid histogram is for $M_{top} = 180$ GeV/c^2.

FIG. 14. The transverse mass distribution for the $W \rightarrow e\nu$ and $W \rightarrow \mu\nu$ samples.

decay, in practice this is not the case because jets might coalesce, be lost down the beam line, or fail the 15-GeV calorimeter threshold requirement. On average, three or four reconstructed jets are observed in association with leptons from W decay. A straightforward method of defining a $t\bar{t}$ search sample, which greatly improves the ratio of the top signal to $W+$multijets background, is to require $N_{\rm jet} \geq 3$. Approximately 75% of the $t\bar{t}$ events ($M_{\rm top} = 160$ GeV/c^2) and less than 0.5% of all W events pass this requirement. We have chosen $N_{\rm jet} \geq 3$, rather than 4, as our signal region because the efficiency of the $N_{\rm jet} \geq 4$ requirement is a strong function of the top mass and of the modeling of initial-state gluon radiation in top events (see Sec. VII B).

Figure 16 shows the lepton-$\not{E}_T$ transverse mass distribution for the 52 events in the data that have $N_{\rm jet} \geq 3$ (see Table XIV). The distributions from the VECBOS [26] Monte Carlo program of W events and the ISAJET Monte Carlo program of $t\bar{t}$ events ($M_{\rm top} = 160$ GeV/c^2) are shown as solid and dashed histograms, respectively. The area of both Monte Carlo distributions is normalized to 52 events. The transverse mass distribution for $t\bar{t}$ events is slightly broader than the VECBOS prediction for higher-order QCD W production because $t\bar{t}$ events are on average more energetic, which causes a degradation of the $\not{E}_T$ resolution. The data have the characteristic high transverse mass edge near 80 GeV, as expected for on-shell W bosons.

The background in the $W+$jet(s) sample due to misidentified leptons in QCD-jet events or semileptonic decays in $b\bar{b}$ events, is estimated to be $(10\pm5)\%$, independent of jet multiplicity (for $N_{\rm jet} \geq 1$). This background es-
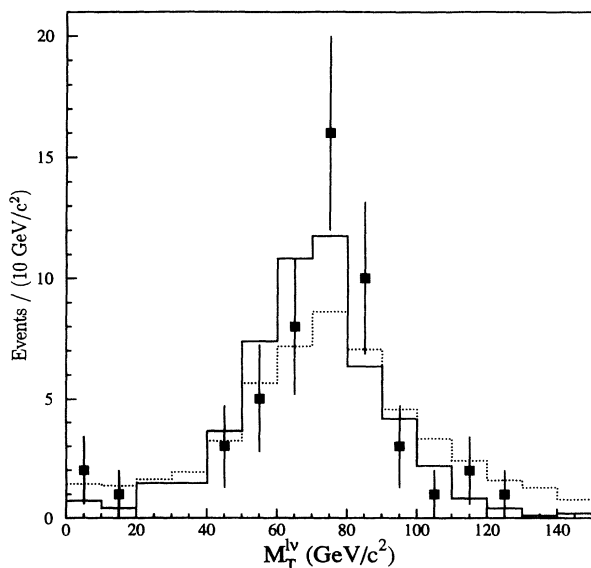
TABLE XV. Estimated number of background events in the $N_{\rm jet} \geq 3$ sample. The $Z \to \mu\mu$ and ee backgrounds are calculated by first estimating the acceptances for these events relative to those for $W \to \mu\nu$ and $e\nu$ and then normalizing to the observed data rate assuming that the data contain no top events. The uncertainty in the total background estimate takes into account correlations between uncertainties in the various background sources. There are 52 events with $N_{\rm jet} \geq 3$ in the data.

Background source	Background estimate
QCD and $b\bar{b}$	5.2 ± 2.6
WW, WZ, and ZZ	2.6 ± 1.2
$Z \to \tau\tau$	1.7 ± 0.5
$Z \to \mu\mu$	1.5 ± 0.4
$Z \to ee$	1.2 ± 0.6
Total	12.2 ± 3.1

timate is obtained by extrapolating the $\not{E}_T$ distribution for isolated leptons into the W-signal region, using the $\not{E}_T$ shape of the nonisolated leptons [17]. Other sources of backgrounds are $W \to \tau\nu$, followed by $\tau \to e$ or μ ($\approx 4\%$), $Z \to \tau\tau$, and $Z \to ee$ or $\mu\mu$, where one of the leptons is undetected (if the second muon in $Z \to \mu\mu$ is outside the CTC acceptance, for example). Backgrounds from Z decays are approximately 8% of the $W+$jet(s) sample. The data shown in Table XIV have not been corrected for QCD, $b\bar{b}$, $W \to \tau\nu$, and Z backgrounds. Background estimates for the $N_{\rm jet} \geq 3$ sample are given in Table XV.

In a previous letter [35], we presented a detailed comparison of $W +$ jets data with theoretical expectations, based on a data set collected in 1988–1989. In Table XVI we compare the number of $W +$ jets candidates in this analysis with expectations from the VECBOS Monte Carlo program. The VECBOS event generator is based on a tree-level matrix element calculation; therefore it has significant theoretical uncertainties in its absolute rate predictions. In this study, the VECBOS Monte Carlo events are generated with a renormalization scale $Q^2 = \langle P_T \rangle^2$, where $\langle P_T \rangle$ is the average transverse momentum of the partons. This choice of renormalization scale tends to yield higher cross sections than an alternative possible choice of $Q^2 = M_W^2$. In the analysis presented in Ref. [35], where the jet definition was slight-

FIG. 16. The lepton-$\not{E}_T$ transverse mass distribution for data (points), the VECBOS W Monte Carlo program (solid), and $t\bar{t}$ Monte Carlo events (dashed) when $N_{\rm jet} \geq 3$. The area of both Monte Carlo histograms are normalized to the number of data events, 52. The VECBOS result contains contributions from both three and four jets in the ratio observed in the data.

TABLE XVI. Comparison of $W+$jet(s) yields with expectations from the VECBOS Monte Carlo program. The first uncertainty on the VECBOS prediction is due to Monte Carlo statistics, the second is due to jet energy scale and lepton identification efficiency uncertainties, the third is due to the luminosity normalization. The VECBOS predictions include the $W \to \tau\nu$ contribution. The data have not been corrected for backgrounds, which are discussed in the text.

Jet multiplicity	Data	VECBOS $(Q^2 = \langle P_T \rangle^2)$
1 jet	1713	$1571\pm82^{+267}_{-204}\pm55$
2 jets	281	$267\pm20^{+77}_{-53}\pm9$
3 jets	43	$39\pm3^{+11}_{-9}\pm2$
≥ 4 jets	9	$7\pm1^{+3}_{-2}\pm0.2$

ly different than the one used here, it is found that the cross sections for $Q^2 = M_W^2$ are lower than those calculated for $Q^2 = \langle P_T \rangle^2$ by a factor of ≈ 1.3 for $N_{\text{jet}} = 1$, rising to ≈ 2.1 for $N_{\text{jet}} = 4$. The VECBOS $W + N$ jets predictions displayed in Table XVI are based on the $W + N$ jets matrix element only. We have not attempted to correct for the cases where, for example, a generated $W + (N+1)$ jets event is reconstructed to be an $W + N$ jets event.

The acceptances for $t\bar{t}$ and W+multijet events passing the lepton identification and kinematic requirements are determined from the ISAJET $\bar{p}p \to t\bar{t}$ and VECBOS $\bar{p}p \to W$+multijet Monte Carlo programs, and the CDF detector simulation. Acceptances are then corrected for the lepton trigger inefficiencies, described in Sec. III A, and for differences in the lepton identification efficiencies between data and Monte Carlo simulation. After correcting for trigger efficiencies, the acceptance for electron events is corrected for two additional effects: (1) the photon-conversion removal algorithm is applied to data, but not to Monte Carlo events, and is estimated to reject $(5\pm3)\%$ of prompt electrons, and (2) the efficiency for high-P_T isolated electrons to pass the combined electron identification requirements has been measured in a data sample of $Z \to e^+ e^-$ events to be $(5\pm4)\%$ larger than in the Monte Carlo simulation. Similarly, the acceptance for muon events is degraded because the efficiency of the muon matching requirements is measured to be $(4.8\pm1.5)\%$ smaller in data than in Monte Carlo simulation. As discussed in Sec. III A, a large fraction of the CMX muon data was collected with a level-1 calorimeter trigger requirement. The efficiency of this requirement on $W \to \mu$ events is a strong function of the hadronic activity in the event, and Monte Carlo events with a CMX muon are required to satisfy a simulation of the level-1 trigger.

Table XVII lists the $t\bar{t}$ production cross section [10] for various top masses. Also shown is the acceptance for top events, including branching ratio, and the number of expected $t\bar{t}$ events with $N_{\text{jet}} \geq 3$ in 19.3 pb^{-1} of data. As shown in Table I, the branching ratio is 24/81 for one of the two W's in top events to decay to e or μ and the other one into hadrons. We also expect a $\approx 5\%$ contribution to the total acceptance from events from $W \to \tau \to e$ or μ, $W \to q\bar{q}$. Further contributions to the total acceptance come from events where both W's decay leptonically into e, μ, or τ and this amount varies between 14% and 20% for top masses between 120 and 180 GeV/c^2. The uncertainty on the expected number of events is the quadrature

sum of a 3.6% systematic uncertainty in the luminosity and the systematic uncertainties on the acceptance, which are discussed below.

Systematic uncertainties in the acceptance arise from uncertainties in the lepton detection efficiencies (5%), uncertainties in the jet energy scale, and in the modeling of initial-state radiation, which affects the expected jet multiplicity in top events. The jet energy scale is known to 10% (Sec. III D), resulting in an uncertainty on the $t\bar{t}$ acceptance that varies between 10% and 3% for top masses between 120 and 180 GeV/c^2. Note that this energy scale uncertainty has a much larger effect on the VECBOS predictions displayed in Table XVI because of the steeply falling transverse energy spectrum of jets in W events. The uncertainty on the kinematic acceptance due to modeling of initial-state radiation in the $t\bar{t}$ Monte Carlo program is taken to be 7%, which is one half of the decrease in acceptance when initial-state radiation is turned off in the ISAJET Monte Carlo generator.

The lepton identification criteria listed in Secs. III B and III C contain a number of explicit and implicit isolation requirements. We use $t\bar{t}$ events made with the ISAJET Monte Carlo program and the detector simulation to extrapolate the efficiency for highly isolated leptons to the less isolated leptons expected in $t\bar{t}$ events, which typically contain three or four observed jets (see Fig. 15). The efficiency of the isolation requirement, which is $(96\pm1)\%$ for leptons from inclusive W decays, is estimated to be $\approx 86\%$ for leptons in $t\bar{t}$ events with three or more jets. To study the model dependence of the acceptance calculation, we also have computed the top acceptance with the HERWIG generator. For a top mass of 120 [180] GeV/c^2, we find the acceptance to be $(10\pm5)\%$ lower $[(1\pm3)\%$ higher] than that calculated using the ISAJET generator (the uncertainties here are statistical). As a further check, we use the identical procedure (i.e., ISAJET generator, detector simulation, and corrections described above) to calculate the acceptance for inclusive W events. We then use this acceptance, in conjunction with the observed number of W events, to extract a measurement of the W production cross section, which is found to be consistent with our previously reported measurement [17,36].

As can be seen from Tables XVI and XVII, the VECBOS prediction for the W+jets background in the three or more jet sample (≈ 46), is larger than the expected number of $t\bar{t}$ events for top masses above 120 GeV/c^2. Additional background rejection is needed to isolate a possible $t\bar{t}$ signal. This can be provided by requiring the presence

TABLE XVII. Summary of $t\bar{t}$ acceptance as a function of top mass. A_{top} is the acceptance for top events, including branching ratios, for the lepton $+E_T+3$ or more jets selection. The expected number of events is calculated with the central value of the theoretical expectation for $\sigma_{t\bar{t}}$. It includes a 3.6% normalization uncertainty on the luminosity of 19.3 pb^{-1}, but no theoretical uncertainty. There are 52 events in the data passing the lepton $+E_T+3$ or more jets requirements.

M_{top} (GeV/c^2)	120	140	160	180
$\sigma(t\bar{t})$ (pb) (theory)	$38.9^{+10.8}_{-5.2}$	$16.9^{+3.6}_{-1.8}$	$8.2^{+1.4}_{-0.8}$	$4.2^{+0.6}_{-0.4}$
A_{top}	0.051 ± 0.007	0.067 ± 0.008	0.077 ± 0.008	0.081 ± 0.008
Expected No. of events	39 ± 6	22 ± 3	12 ± 2	6.6 ± 0.7

of a b-flavored hadron in the W+multijet sample. In Sec. V B and V C we discuss searches for b quarks exploiting displaced vertex and semileptonic decay signatures. In addition, we will show that, by looking for a b quark, we can obtain background estimates independent of the uncertain absolute rate predictions of the VECBOS Monte Carlo program.

B. Search for $t\bar{t}$ using SVX b tagging

The average P_T for b hadrons from top-quark decay [see Fig. 17(a)] is large compared with the scale set by the b-quark mass. This, combined with the long b-quark lifetime, results in a long average decay length for b hadrons in $t\bar{t}$ events. The distribution of the decay distance in the plane transverse to the beam direction, defined to be L_{xy}, is shown in Fig. 17(b).

A simplified illustration of an event containing a b hadron with large P_T is shown in Fig. 18. Tracks from the b-hadron decay are measurably displaced from the $\bar{p}p$ interaction point, called the primary vertex. The ability to identify such displaced tracks depends on the resolution for determining both the trajectory of each track and the position of the primary vertex from which most tracks emanate. At the CDF interaction region, primary vertices have a Gaussian distribution along the beam direction with $\sigma \sim 30$ cm and transverse to the beam axis with a $\sigma \sim 36$ μm. The detector axis and beam axis are not exactly parallel and coaxial. The detector axis and the beam axis have a relative slope of ~ 4.5 μm/cm in the horizontal plane and ~ -3 μm/cm in the vertical plane. Through the course of the 9 months of data taking, these slopes were stable at the level of 1 μm/cm. The displacement of the detector axis and the beam axis (at the nominal interaction position $z=0$) varied between 200 and
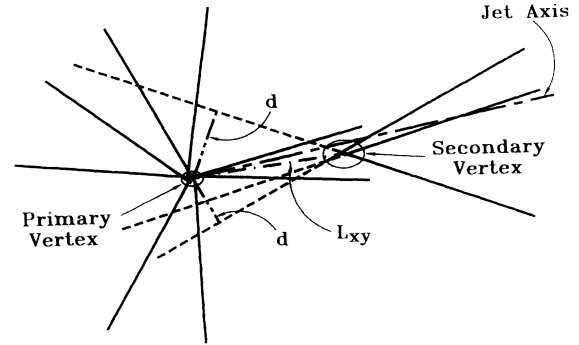
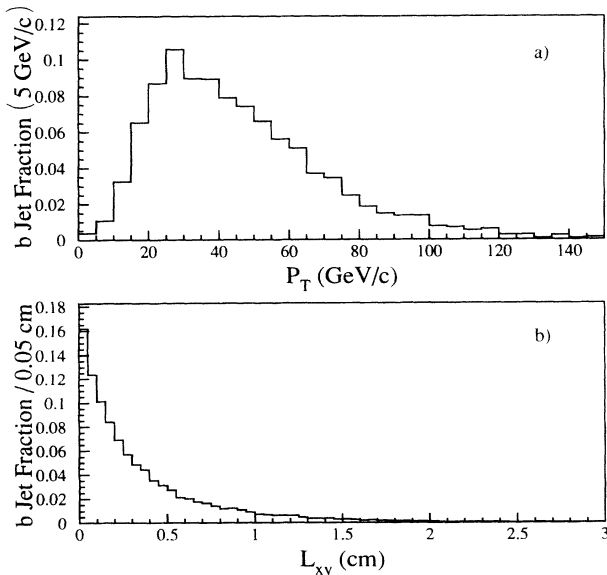FIG. 18. Simplified view of an event containing a secondary vertex shown in the transverse (r-ϕ) plane. The solid lines represent charged-particle tracks reconstructed in the SVX. The primary vertex is the point in the r-ϕ plane where the $\bar{p}p$ interaction occurs. The secondary vertex is the point of decay for a long-lived particle originating at the primary vertex. The impact parameter, d, is shown for representative tracks. Also shown is L_{xy}, the two-dimensional decay distance to the secondary vertex, measured in the r-ϕ plane.

1200 μm in the horizontal plane and 400 and -1000 μm in the vertical plane. The slope and displacement drifted due to changing Tevatron conditions, but were measured on a run-by-run basis to accuracies of ~ 0.4 μm/cm for the slope and ~ 10 μm for the displacement.

The primary vertex is found for each event by a weighted fit of the SVX tracks and the VTX z event vertex position, with appropriate corrections for detector offset and slope. An iterative search removes tracks from the fit, which have large impact parameters. The impact parameter, d, is the distance of closest approach of a track to the primary vertex in the r-ϕ plane (see Fig. 18). The uncertainty in the fitted primary-vertex coordinates transverse to the beam direction ranges from 6 to 36 μm depending on the number of tracks and the event topology.

Because of the high-luminosity conditions of the 1992–1993 run, approximately 40% of events in the W sample described above contain multiple primary interactions separated along the beam axis. In these events, the event vertex is chosen to be the one with the greatest total transverse momentum of associated tracks. All tracks used in the vertex fit and subsequent analysis are required to extrapolate to within 5 cm of this vertex along the beam direction. The resolution on the extrapolation to the z position for CTC tracks above 2 GeV/c is approximately 6 mm. The primary high-P_T electron or muon is associated with the chosen vertex in 99.9% of the events.

Displaced tracks identified with the SVX are used as input to three b-tagging algorithms. All three algorithms require the size of the impact parameter, d, to be large compared to its estimated uncertainty. The sign of the impact parameter is given by the location of the beam in the transverse plane, relative to the circle, which describes the track trajectory in the transverse plane. For positively charged tracks, the CDF convention is to assign a negative sign to d when the location of the beam lies inside the circle, and a positive sign to d when it is outside. This convention is reversed for negatively

FIG. 17. (a) The P_T spectrum for b hadrons from $t\bar{t}$ Monte Carlo events with M_{top} of 160 GeV/c^2. (b) The transverse decay length distribution for the b hadrons, before detector resolution effects, in the same sample.

charged tracks. Tracks from heavy-flavor decay will populate both the positive and negative tails of the impact parameter distribution. The uncertainty on d, σ_d, is computed for each track with the measured momentum and multiple scattering based on the traversed material. It ranges from 50 μm for 1 GeV/c charged tracks to 15 μm for 10 GeV/c tracks. A check of this calculation is shown in Fig. 19(a), which displays the distribution of impact parameter significance, d/σ_d, for tracks from a subset of events in the 50-GeV jet-trigger sample. The core of the data distribution fits well to a Gaussian distribution with $\sigma = 1.08 \pm 0.01$. The tails of the distribution come from a combination of non-Gaussian effects and true long-lived particles. Using a combination of data and Monte Carlo simulation of heavy flavor decays, we estimate approximately 30% of the tracks with $|d|/\sigma_d > 3.0$ are the decay products of long-lived particles. Shown in Fig. 19(b) is the distribution of d/σ_d for tracks from b decays taken from an ISAJET Monte Carlo sample after full CDF detector simulation. This broad distribution shows the effect of the long b-quark lifetime.

1. Description of the tagging algorithms

The b-tagging algorithms are applied to sets of SVX tracks associated with jets that have calorimeter $E_T \geq 15$ GeV and $|\eta| < 2.0$. An SVX track is associated with a jet if the opening angle between the track direction and the jet direction (given by the calorimeter) is less than 35°. In order to remove tracks consistent with photon conversions and K_S or Λ decays originating from the primary vertex, we impose an impact parameter requirement ($|d| < 0.15$ cm). This removes 3.1% of tracks prior to tagging and is approximately 99% efficient for tracks from b decay. In addition, track pairs consistent with the K_S or Λ mass are removed. The three b-tagging algo-

FIG. 19. The distribution of impact parameter significance, d/σ_d, for (a) tracks from a subset of events in the 50-GeV jet-trigger sample, and for (b) tracks from b decay in $t\bar{t}$ Monte Carlo events ($M_{\text{top}} = 160$ GeV/c^2). The Gaussian fit to the core of the 50-GeV jet distribution has $\sigma = 1.08 \pm 0.01$.

rithms are referred to as the "jet-vertexing" algorithm, the "jet-probability" algorithm, and the "d-ϕ" algorithm.

The jet-vertexing algorithm requires a jet to contain at least two good SVX tracks (defined in Sec. II) with $P_T \geq 2$ GeV/c and absolute impact parameter significance $|d|/\sigma_d \geq 3$ [37]. Using these tracks, L_{xy} and its error $\sigma_{L_{xy}}$ (typically ~ 130 μm) are calculated using a three-dimensional common vertex constrained fit. If the contribution to the overall χ^2 of the fit due to any one track is more than 50, that track is removed and a fit is attempted with the remaining tracks. The sign of L_{xy} is given by the sign of the vector dot product of the L_{xy} direction and the direction of the vector sum of the tagged tracks' momenta. The secondary vertex is required to have significance $|L_{xy}|/\sigma_{L_{xy}} \geq 3.0$. Jets containing many mismeasured tracks, and no true secondary vertices, have vertices that are equally likely to have L_{xy} either positive or negative. This has been checked by combining tracks from different jets to form a vertex. This avoids contamination from real long-lived objects found within a single jet. In order to mimic the small opening angle of tracks in the same jet, events with jets nearly back-to-back were selected. Track pairs with an opening angle near 180° will form vertices with similar properties to those formed by tracks with opening angles near 0°. The larger of the two jets is taken as defining the positive L_{xy} direction. The resultant L_{xy} distribution is observed to be symmetric about $L_{xy} = 0$. In contrast, jets containing long-lived particles have vertices with L_{xy} predominantly positive. For the purposes of identifying b jets, only jets with positive L_{xy} are considered "tags." As explained below, the bulk of the SVX b-tagging results reported use this algorithm.

The jet-probability algorithm [38] uses a track's signed impact parameter to determine the probability that the track is consistent with originating from the primary vertex (i.e., zero lifetime). For this algorithm only the sign of the impact parameter is defined to be positive if the point of closest approach to the primary vertex lies in the same hemisphere as the jet direction, and negative otherwise. Tracks from long-lived objects will usually have a positive impact parameter. A resolution function is derived from the negative impact parameter distribution of tracks from jets in the 50 GeV jet-trigger sample. Each track in a jet is assigned a probability that it comes from the primary vertex using this resolution function, and the track probabilities are combined into an overall probability that the jet is consistent with the zero lifetime hypothesis. A jet is tagged by this algorithm if it has an overall jet probability of less than 1% and two or more tracks with positive impact parameter and $P_T \geq 1.5$ GeV/c. Figure 20 shows the jet probability for jets with $E_T > 9$ GeV in the inclusive-jet sample, and for jets near a muon with $P_T > 9$ GeV/c in the inclusive central muon sample. The muon sample has been measured to be enriched in semileptonic b-hadron decay [39]. The enhancement at low jet probability in the muon sample is due to heavy-flavor decay. A smaller enhancement at low jet probability, also indicating the presence of heavy flavor, is found in the inclusive-jet sample.
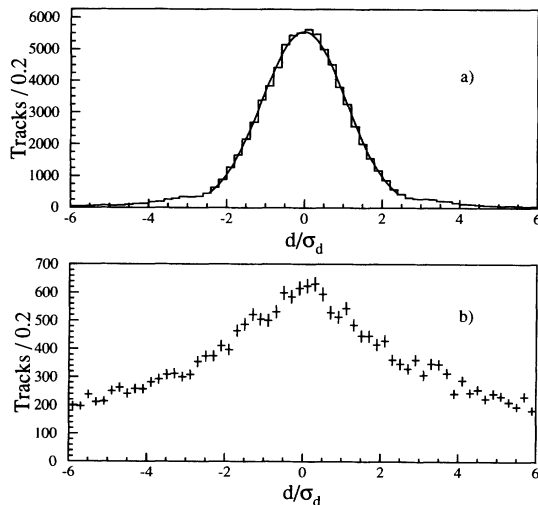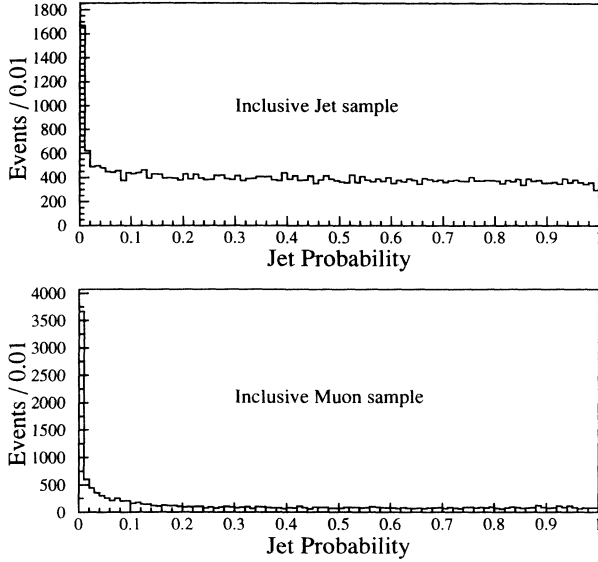
FIG. 20. The distribution of jet probability for jets in the inclusive-jet sample and for jets near muon candidates. Low probability indicates that the tracks in the jet are inconsistent with arising from the primary vertex.

The third b-tagging algorithm identifies secondary vertices by the d-ϕ correlation between the impact parameter d and azimuthal angle ϕ of the associated tracks [40]. The algorithm requires at least three good tracks with $P_T \geq 400$ MeV/c and $|d|/\sigma_d \geq 2.5$. Tracks identified as low-P_T electrons or muons as described in Sec. V C are included regardless of their impact parameter significance. Figure 21 shows all SVX tracks represented as points in the d-ϕ plane for a typical event tagged by this algorithm. The tracks with small d are likely to
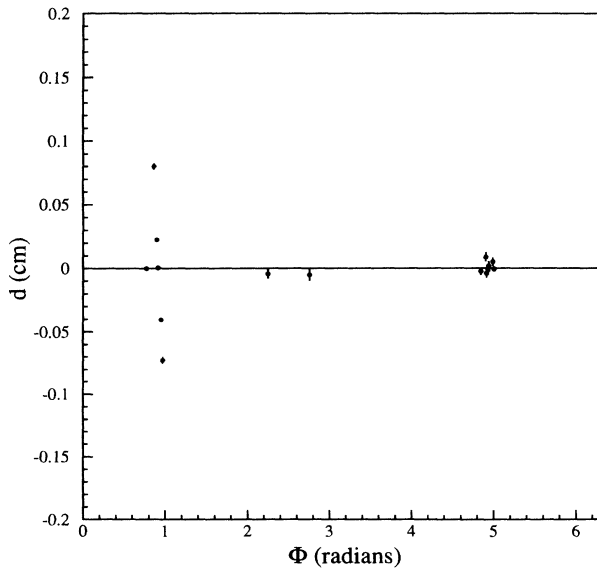
FIG. 21. The distribution of the impact parameter (d) vs azimuthal angle for the SVX tracks in a typical tagged event. The d-ϕ tagging algorithm identifies the tracks near $\phi = 1$ radian as a potential heavy-flavor decay.

come from the primary vertex. Secondary vertices will give tracks which form a line in the d-ϕ plane with nonzero slope. The d-ϕ algorithm tags the tracks near $\phi = 1$ radian with large d as a heavy-flavor decay candidate.

The three b-tagging algorithms used in this analysis were developed to complement and check each other. The consistency of their results tests the stability of the analysis with respect to (1) changes in the minimum P_T and impact parameter significance requirements in the selection of the tracks that may be included in a tag, and (2) changes in the minimum number of tracks required for a tag. The tracking errors are strongly correlated with the track P_T, and the impact parameter significance of the tracks and vertexing errors are in turn correlated with the number of tracks used to find a vertex. The consistent results of the three tagging algorithms are an important confirmation that our treatment of tracking and vertexing systematic uncertainties is correct.

The effort to estimate all systematic uncertainties and perform various cross checks was focused on the jet-vertexing algorithm. Therefore, in this paper the bulk of the analysis reported uses the jet-vertexing algorithm. The tagging efficiency, its systematic uncertainties, and background rates are discussed in detail for this method. Where appropriate, the results from the other two tagging methods are also given.

To confirm that these algorithms identify b quarks, their performance is evaluated and cross checked in a large inclusive electron sample, selected by requiring an electron with $|\eta| < 1.0$ and $P_T \geq 10$ GeV/c. We measure the fraction of the events in this sample that originate from semileptonic B decay by measuring the yield of muons near the electron candidate and comparing this to the yield predicted by a Monte Carlo simulation of the cascade decay $B \rightarrow e\mu X$. This method gives a semileptonic B-decay fraction for the inclusive electron sample (F_b) of $(37 \pm 8)\%$. This result has been checked by an alternate method for measuring F_b, which uses the yield of observed $D^0 \rightarrow K\pi$ decays near the electron candidates, compared to the yield predicted by a Monte Carlo simulation of the decay $B \rightarrow eD^0 X$. This result is consistent with the F_b quoted above. To verify that electron candidates, which have an associated secondary vertex include a high percentage of b jets, the decay length of the secondary vertex is converted into an estimate of the effective proper decay length ("$c\tau_{\rm eff}$") using the expression [41]

$$c\tau_{\rm eff} = L_{xy} \frac{M}{P_T F}, \tag{2}$$

where M is the invariant mass of the tracks associated to the secondary vertex, P_T is their total vector transverse momentum, and F is a scale factor determined from a b Monte Carlo sample, which accounts for b-hadron decay products that are not attached to the secondary vertex. This simulated sample was made using the HERWIG [25] event generator and the standard CDF simulation. For P_T greater than 15 GeV/c (which is true for the majority of tags), F is independent of P_T and is determined to be 0.7. Below P_T of 15 GeV/c, F rises slowly by approximately 10% of itself.
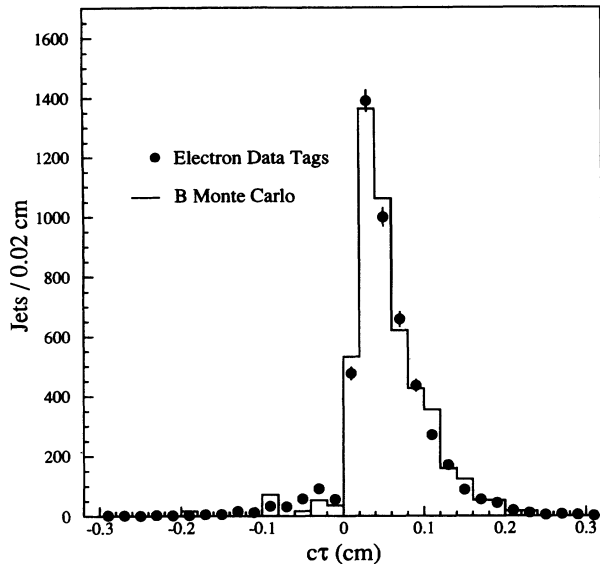
FIG. 22. The $c\tau_{\text{eff}}$ distribution for jets with a secondary vertex in the inclusive electron data (points with errors) compared to Monte Carlo simulation (histogram) with the world average B lifetime.

The $c\tau_{\text{eff}}$ distribution for the electron data is shown as the points in Fig. 22, and the $c\tau_{\text{eff}}$ distribution for jets in the Monte Carlo sample is shown as the solid histogram. The data agree well with the Monte Carlo simulation of b decay, which uses the world average b-hadron lifetime [42].

We attempt to classify the tags observed in a sample of unbiased (generic) jets that are found in events passing the 50 GeV jet trigger. The $c\tau_{\text{eff}}$ distribution for tags found in this event sample is shown in Fig. 23. We fit this dis-
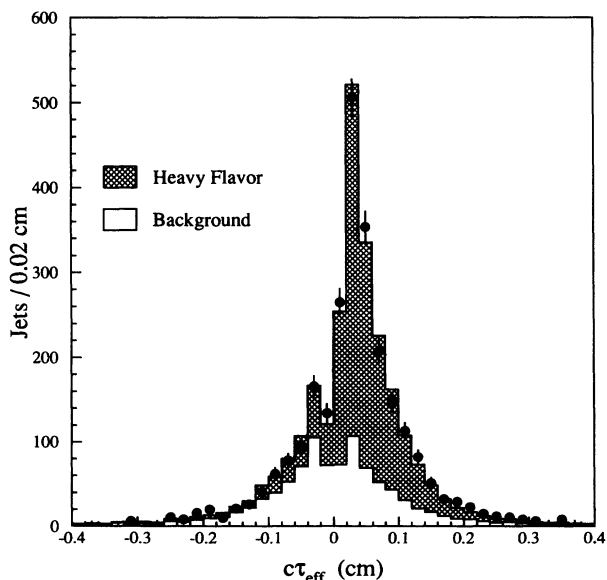

FIG. 23. The $c\tau_{\text{eff}}$ distribution for jets with a secondary vertex in the sample collected with a 50-GeV jet trigger (points). The distribution is fit to a combination of heavy flavor (b decays and c decays; shaded) and background (histogram). The fit gives the relative fractions of positive L_{xy} tags from heavy flavor and background to be approximately 75% and 25%, respectively.

tribution to a combination of $c\tau_{\text{eff}}$ distributions from Monte Carlo simulation of b-quark decays, c-quark decays, the "fake" decays caused by mismeasured tracks. The $c\tau_{\text{eff}}$ distributions from b quarks and c quarks are determined by first hadronizing quarks using ISAJET, then decaying the mesons using the CLEO Monte Carlo program. The track parameters of the decay products are then smeared by a resolution function determined from the data. The $c\tau_{\text{eff}}$ for fake tags is determined by generating tracks with zero lifetime and smearing the track parameters with the resolution function. The three distributions of $c\tau_{\text{eff}}$ are then fit simultaneously to the data spectrum and the relative contribution of each is determined. From this fitting procedure we can extract an estimate of the fraction of tags in this sample that come from each of these three sources. We find the tagged events for this sample are approximately 75% heavy flavor (b and c quarks) and 25% fakes. The observed b to c quark ratio is consistent with 1.0, before correcting for the difference in tagging efficiencies for b and c quarks. We can also estimate the same fractions for the tags, which have negative L_{xy}. For the negative L_{xy} sample, we find the tagged events are approximately 35% heavy flavor and 65% fakes. Systematic uncertainties in this procedure arise from uncertainties in the Monte Carlo simulation of heavy flavor, the resolution function, and the simulation of the fakes. These effects are under study and will be discussed further in a separate publication.

2. Tagging efficiency

We use a data sample of inclusive electron events to measure the efficiency for tagging a single semileptonic b jet. The data sample is enriched in $b\bar{b}$ events, where an electron from a semileptonic b-hadron decay is recoiling against a jet from the other b. Two complementary methods for measuring the tagging efficiency are used. In the first method, we identify a subsample of events, which have at least one tagged jet that is not the jet which contains the electron candidate. The number of such events is N_{single}. By selecting this event sample, we increase the b purity by about a factor of 2 and therefore reduce the relative systematic error on the b purity. The requirement also isolates a sample of events where the two b quarks are spatially separated so the tagging efficiency of a single b jet can be measured. Within this sample, we then examine the jets that contain the electron candidate and count the number of events in which these jets are also tagged. This number is referred to as N_{double}. The SVX b-tagging efficiency for semileptonic b decays, ϵ_{sl}, is given by

$$\epsilon_{\text{sl}} = \frac{N_{\text{double}}}{N_{\text{single}}} . \tag{3}$$

In the second method, we use the entire electron sample and measure $N_{\text{tagged}\ e}$, the number of tagged jets that contain the electron candidate. The ϵ_{sl} is then given by

$$\epsilon_{\text{sl}} = \frac{N_{\text{tagged}\ e}}{N_e \times F_b} , \tag{4}$$

F. ABE *et al.*

where N_e is the number of electron candidates and F_b is the fraction of electrons which come from semileptonic b-hadron decay $(37\pm8)\%$. In both methods, the efficiency is measured for jets with at least two good SVX tracks and small background subtractions (of order 10%) are performed to correct for mistags of non-b jets. The efficiency for tagging a semileptonic b decay found using the first method is 0.31 ± 0.03, where the uncertainty is dominated by the limited number of double-tagged events. The efficiency found using the second method is 0.29 ± 0.06, where the error is dominated by the uncertainty on F_b.

Monte Carlo simulation is used to extrapolate the measured b-tagging efficiency for semileptonic b decays to that expected for generic b decays in $t\bar{t}$ events. To do this we must scale the tagging efficiency in the Monte Carlo simulation to the value observed in the data. Figure 24 shows the ratio of the tagging efficiency measured in the electron data divided by the tagging efficiency observed in the semileptonic b Monte Carlo simulation, as a function of the E_T of the jet associated with the electron. The Monte Carlo tagging efficiency must be multiplied by a scale factor of 0.72 in order to agree with that measured in the electron data.

The b decays used to determine the scale factor and b decays from $t\bar{t}$ events differ because the average b-jet E_T is higher in $t\bar{t}$ events than it is in the electron data sample, and because the b decays in the electron data are semileptonic, whereas the decays in $t\bar{t}$ events are generic. However, we find the scale factor to be approximately independent of E_T, as shown in Fig. 24. In addition, we find good agreement between kinematic features (invariant mass, summed P_T of the tagged tracks, the tagged track multiplicity, etc.) of tagged jets in data that do not contain an electron, and a Monte Carlo simulation of generic b decays. Based on this information, we scale down the tagging efficiency in Monte Carlo $t\bar{t}$ events by a factor of 0.72.

The systematic uncertainty assigned to the determination of the Monte Carlo scale factor is ±0.21 (29%) and is dominated by a ±0.17 (23%) systematic uncertainty in its E_T dependence. We estimate this effect by taking a ±1 σ variation in the slope of a linear fit to Fig. 24, weighted by the E_T spectrum of b jets from $t\bar{t}$ events. The systematic uncertainty also includes an uncertainty

due to limited statistics on the number of double tags, and an uncertainty on the b fraction of the electron sample. The Monte Carlo simulation has a higher SVX tracking efficiency and slightly better impact-parameter resolution than the data. However, these discrepancies can only account for approximately $\frac{1}{3}$ of the data–Monte Carlo difference. The fact that the SVX b-tagging efficiency is lower than expected does not affect the statistical significance of the results reported here, but does enter into the cross-section calculation as discussed in Sec. VII.

The event-tagging efficiency ϵ_{tag} measures the efficiency for tagging at least one b jet in a $t\bar{t}$ event with three or more observed jets. For the jet-vertexing algorithm, ϵ_{tag} is determined using ISAJET $t\bar{t}$ Monte Carlo events for various top masses and the CLEO parametrization for the decay of the B mesons. Table XVIII gives ϵ_{tag} and the number of expected SVX b-tagged events for various values of the top mass. These estimates include corrections for the scale factor and the effect of inefficiency for events with primary vertices outside the SVX fiducial volume. Tagging efficiencies measured for the other two b-tagging algorithms are similar to the tagging efficiencies measured for the jet-vertexing algorithm.

For a top mass of 160 GeV/c^2, ϵ_{tag} can be factorized as follows: Of the $t\bar{t}$ events, which pass the $N_{\text{jet}} \geq 3$ requirement, 67% have at least one b jet within the SVX fiducial volume. Of these events, 91% have at least one b jet with two or more tracks, which pass the jet-vertexing selection criteria. Of these selected events, 36% have at least one tagged jet. The 36% includes the 0.72 factor between Monte Carlo simulation and data tagging efficiencies. For a single b jet that is well contained within the SVX and CTC fiducial volumes ($|z$ vertex$| < 25$ cm and $|\eta| < 1.0$) and $E_T > 20$ GeV, the b-tagging efficiency is approximately 30%.

The uncertainty on ϵ_{tag} in Table XVIII comes from adding in quadrature the uncertainty in the scale factor and the statistical error from the Monte Carlo sample. To calculate the number of expected events, we use the $t\bar{t}$ cross section from Ref. [10]. The uncertainty on the expected number of events comes from adding in quadrature the uncertainties on the acceptance, the tagging efficiency, and the luminosity. We do not include an uncertainty from the $t\bar{t}$ cross section.

3. Backgrounds in the SVX search

In the $W+$multijet sample, we expect tags from a variety of sources in the absence of any $t\bar{t}$ events. These
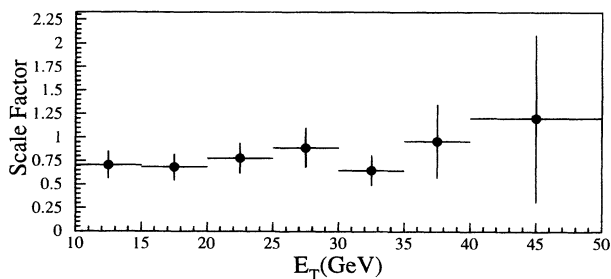

FIG. 24. The SVX tagging efficiency in the inclusive electron data divided by the SVX tagging efficiency in a Monte Carlo sample of semileptonic B decays.

TABLE XVIII. Summary of SVX tagging efficiency (defined as the efficiency for tagging at least one jet in a $t\bar{t}$ event with three or more jets) and the expected number of SVX b-tagged $t\bar{t}$ events in the data sample.

M_{top} (GeV/c^2)	ϵ_{tag}	Expected No. of events
120	0.20 ± 0.05	7.7 ± 2.5
140	0.22 ± 0.06	4.8 ± 1.7
160	0.22 ± 0.06	2.7 ± 0.9
180	0.22 ± 0.06	1.4 ± 0.4

are events from the production of W's in association with heavy quark pairs ($W b\bar{b}, W c\bar{c}$) [13], mistags due to track mismeasurements, $\bar{p}p \to W +$ charm, $b\bar{b}$ production, WW or WZ production, and $Z \to \tau\bar{\tau}$. The dominant contribution to the background is expected to come from the first two sources, and two different techniques are used to estimate their magnitude. The first method directly measures the tagging rate in inclusive-jet events, which has contributions from both heavy-flavor tags and mistags. This tagging rate is then applied to the $W +$ multijet events to produce a background estimate. In the second method we explicitly compute the $W +$ heavy quark pair background, using the theoretical tools available, and add a separate estimate from the data of the mistag background.

In the first method, the heavy quark pair content of jets in $W +$ multijet events is assumed to be the same as, or less than, that in inclusive-jet events. The positive L_{xy} tag is measured in a sample of 67 000 events passing the 50-GeV jet trigger. These events contain 137 000 jets with $E_T > 15$ GeV, which we will refer to as "generic jets" to distinguish them from jets enriched in heavy flavor. The tagging rate measured in this sample is used to assign a tagging probability to each of the jets in the $W +$ multijet events. This approach has the advantage that it uses a directly measured tag rate including mistags, the small contribution from residual K_S and Λ decays, and all contributions to heavy flavor production in jets.

The heavy-flavor content of jets in an inclusive-jet sample stems from three primary sources: (1) direct production (e.g., $gg \to b\bar{b}$), (2) the so-called gluon-splitting processes, where a final-state gluon branches into a heavy quark pair [43], and (3) flavor excitation (initial-state gluon splitting). In the generic-jet sample, which is triggered by a high transverse energy jet but has no explicit requirement on the transverse energy of the heavy quarks produced, the gluon splitting process accounts for around 65% (75%) of the produced $b\bar{b}$ ($c\bar{c}$) pairs [44]. In the case of $W +$ multijet events, heavy flavor $b\bar{b}$ and $c\bar{c}$ pairs come from gluon splitting only [13]. Both the VECBOS and HERWIG Monte Carlo calculations [25] predict a fraction of gluon jets in $W +$ multijet events smaller than in inclusive-jet events by a factor 1.5 to 2, for jet multiplicities between 1 and 4. Including all contributions, the HERWIG Monte Carlo calculation predicts the b content per jet in the $W +$ multijet sample to be approximately three times smaller than in the generic jet sample. One therefore expects the fraction of heavy flavor in the $W +$ multijet sample to be smaller than that in the generic-jet sample. Using the tagging rate measured in the generic-jet sample should, therefore, provide an overestimate of the $W +$ multijet background. The discussion of the second method later in the section will strengthen this conclusion with a more quantitative study.

The positive and negative L_{xy} tagging rates in the generic-jet sample are shown in Fig. 25 as a function of the jet E_T and jet track multiplicity. Only jets with two or more good SVX tracks, as required by the jet-vertexing algorithm, are considered. The ratio of positive
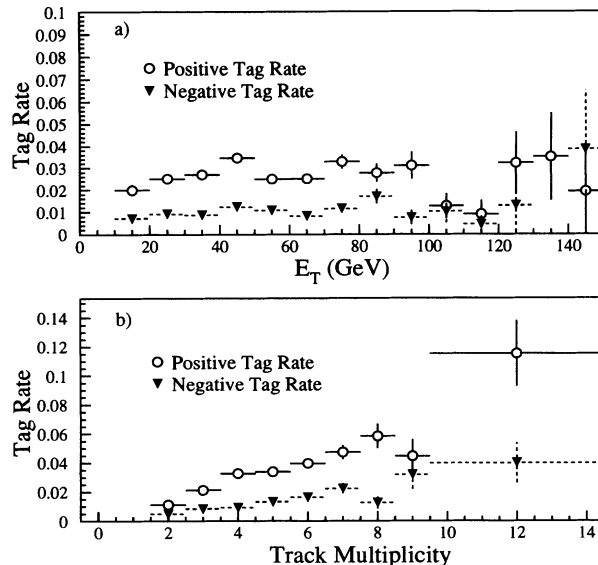

FIG. 25. The tagging rate, defined to be the number of tagged jets divided by the number of jets having two or more good SVX tracks, as a function of (a) the jet E_T and (b) number of SVX tracks associated with the jet. Shown are the rate for positive L_{xy} tags (circles) and negative (triangles) L_{xy} tags as measured in the generic-jet sample.

L_{xy} to negative L_{xy} tags is approximately 2.7:1. The excess of positive L_{xy} tags (i.e., the number of positive L_{xy} tags minus the number of negative L_{xy} tags) is consistent with coming from b or c decay. This is determined using three different methods. First, we compare the $c\tau$ distribution of the tags in data to a Monte Carlo simulation of jets, which contain heavy flavor (see Fig. 22). Second, we have measured the number of SVX tags that contain a low P_T lepton, presumably from b or c decay (selected using the algorithm described in Sec. V C), and compared that to the expectations from a similar Monte Carlo sample of heavy-flavor jets. Lastly, we assume that the excess of positive L_{xy} tags is due to heavy flavor plus the sum of residual K_S decays, Λ decays, or photon conversions. We estimate the latter by relaxing the cuts designed to eliminate tracks that are consistent with K_S or Λ decays. Using the observed yield of tags that are consistent with K_S or Λ decays, and photon conversions, we estimate the residual contamination from these sources in the standard selection (with K_S and Λ removal) is $(10\pm10)\%$. From all three of these studies, which yield consistent results, we conclude that approximately 75–100 % of the excess positive L_{xy} tags are from b or c decay.

The probability of obtaining a SVX tag in the generic-jet sample is parametrized as a function of jet E_T, jet SVX-track multiplicity, and jet $|\eta|$. We check the reliability of these parametrizations of the positive and negative L_{xy} tags in several ways with several different control samples. Figure 26 compares the predicted and observed tag rates as a function of the number of jets and the scalar sum E_T for the same sample. It shows that the parametrization correctly reflects the tagging rate dependence on these variables in this sample. The parametriza-
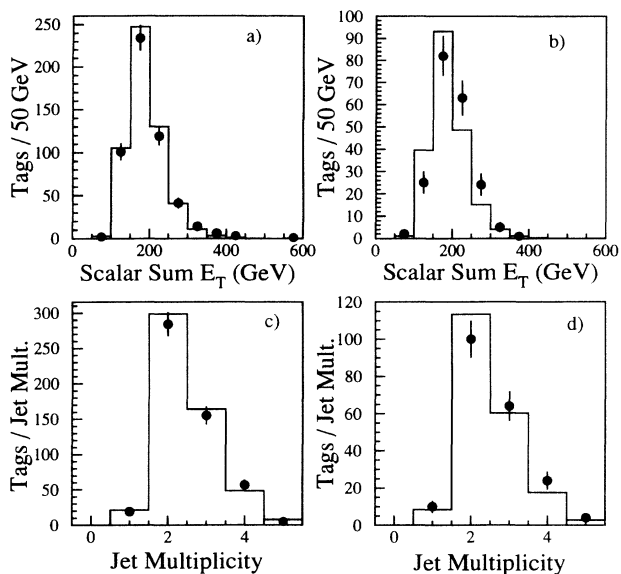
FIG. 26. The predicted number of tags (solid histogram) using the 50-GeV jet-trigger sample tag rate and the actual number of tags observed (points) in the same sample vs scalar sum E_T in the event for (a) the positive L_{xy} tags and (b) negative L_{xy} tags, and vs observed jet multiplicity for (c) the positive L_{xy} tags and (d) negative L_{xy} tags.
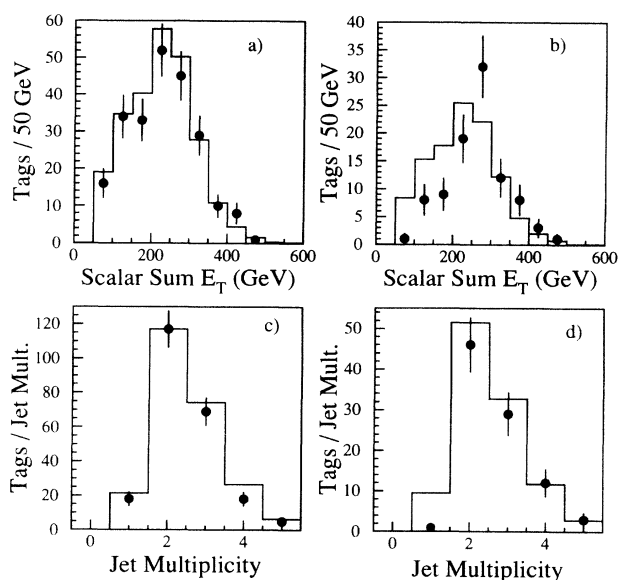

FIG. 27. The predicted number of tags (solid histogram) using the 50-GeV jet-trigger sample tag rate and the actual number of tags observed (points) in the 100-GeV jet-trigger sample vs scalar sum E_T in the event for (a) the positive L_{xy} tags and (b) negative L_{xy} tags, and vs event jet multiplicity for (c) the positive L_{xy} tags and (d) negative L_{xy} tags.

tion further divides the jets sample into two $|\eta|$ regions given by $|\eta| < 1.0$ and $|\eta| > 1.0$. The majority of tagged jets have $|\eta| < 1$, and the tagging rate is observed to fall quickly as $|\eta|$ increases above 1.0. The tagging-rate parametrization is also checked by predicting the tagging rate as a function of jet multiplicity and scalar sum E_T in an independent sample of events from the 100 GeV jet trigger. Figure 27 shows the predicted and observed number of tags, where the prediction uses the tagging rates from the 50-GeV jet sample.

Similar checks of the background method have been performed in electron triggers that are identified as photon conversions, events with a Z boson (see Sec. V D for more), and in a sample of events with scalar sum E_T above 300 GeV. In the latter sample, we have restricted the comparison to the region where there are good statistics in the 50-GeV jet sample by requiring the jet $E_T < 100$ GeV. This is also the relevant E_T range, since in the $52W+3$ or more jet events, only 2 (0) of the jets with two or more associated SVX tracks have E_T above 100 (110) GeV. The results of these studies are summarized in Table XIX.

The poor agreement between the number of predicted and observed negative L_{xy} tags in the sample of events with scalar sum E_T above 300 GeV has been studied extensively. The ratio of the observed to predicted number of tags is 1.38 ± 0.13. Nevertheless, the predicted excess of positive tags agrees with the data. When compared to the 50-GeV jet sample, a larger fraction of the large sum E_T events were collected at the end of the data-taking period, when the SVX performance was deteriorating. If events from this time period are eliminated from the sample, the ratio of the observed to predicted number of tags is reduced to 1.22 ± 0.12. Two of the 52 $W+3$ or more jet events are in this run range and neither of these are tagged. Based on the deviation between the predicted and observed tag rate in these data, and an additional systematic error due to variations in the tag rate over the run (8% relative uncertainty), we assign a systematic uncertainty to the tagging-rate predictions of $\pm13\%$ for the positive L_{xy} tags and $\pm39\%$ for the negative L_{xy} tags.

Applying the positive L_{xy} parametrization to each jet

TABLE XIX. Total observed and predicted $+L_{xy}$ and $-L_{xy}$ tags in independent jet samples. The predictions come from a parametrization using the 50 GeV jet sample. The statistical uncertainties on the predictions in all cases are $\leq 5\%$.

Sample	$+L_{xy}$ Tags		$-L_{xy}$ Tags	
	Observed	Predicted	Observed	Predicted
Jet 100	229	248	92	109
Conversions	67	63	17	20
$\Sigma E_T > 300$ GeV	349	319	162	117
$Z+$jets	2	2.1	0	0.7

in the W sample yields the first estimate of the total expected number of events with a SVX tag from $Wb\bar{b}$, $Wc\bar{c}$, and mistags. This is shown in the first row of Table XXI.

In the second method, the expected $Wb\bar{b}$ and $Wc\bar{c}$ rates are explicitly calculated from Monte Carlo samples and added to the inclusive-jet negative L_{xy} rate, which serves as the estimate of the mistag rate. The leading-order matrix element calculation described in Ref. [13] and the HERWIG Monte Carlo generator [25] are used to compute the inclusive $Wb\bar{b}$ and $Wc\bar{c}$ production rates. The HERWIG prediction is obtained by generating the default $W+1$ jet hard process, heavy quark pairs being produced by gluon splitting from initial and final-state parton evolution. Using the same choice of parton distribution functions and renormalization scale the two approaches yield the same cross section to well within the renormalization scale uncertainty. This uncertainty is estimated in reference [13] to be ±40%. To be conservative, we select the upper value in this range, and multiply the HERWIG prediction by a factor of 1.4.

HERWIG is then used to estimate the fraction of $W+$multijet events containing a $c\bar{c}$ or $b\bar{b}$ pair as a function of jet multiplicity. $W+$multijet final states are produced by HERWIG via multiple hard gluon emission in the shower evolution. The fractions obtained from HERWIG are given in Table XX. They are multiplied by the observed number of $W+$multijet events, after correcting for the non-W background, and by the expected tagging efficiency, approximately 15–20 % for $Wb\bar{b}$ and 4–6 % for $Wc\bar{c}$, to give the number of expected events. This procedure removes any uncertainty on the absolute HERWIG normalization of $W+$multijet rates.

As a test of this procedure and of the ability of HERWIG to reproduce the correct rate of heavy quark production in multijet events, we repeated this study for a sample of QCD jets, and compared the results to data. The HERWIG prediction does not include the factor of 1.4 used to rescale the gluon splitting rate. Figure 28 compares the tagging rate predicted by HERWIG to the observed excess positive L_{xy} tagging rate, as a function of the number of jets in the generic-jet sample and as a function of jet E_T in the sample with scalar sum E_T above 300 GeV. We have also verified that the predictions of the heavy-flavor fraction in the generic-jet sample using the full next-to-leading-order matrix element computation are consistent with HERWIG [44]. This gives us confidence that the predicted rate of tags in $Wb\bar{b}$ and $Wc\bar{c}$ events using the second method should be accurate.

To derive the final uncertainty on the $Wb\bar{b}$ and $Wc\bar{c}$ background estimates from HERWIG, we compute by what factor the rate of gluon splitting to $b\bar{b}$ and $c\bar{c}$ can be changed in HERWIG before the predicted positive L_{xy} excess tagging rate exceeds the rate measured in various jet data samples. We found that in a sample of 20-GeV jet triggers, the measured positive L_{xy} excess tagging rate per jet with two good SVX tracks is larger than the HERWIG prediction (using the default gluon splitting rate) by a factor approximately 1.5. Increasing the rate of gluon splitting to $b\bar{b}$ and $c\bar{c}$ in HERWIG by a factor 2.2 leads to a prediction one σ above the measurement. This changes the overall predicted b content (c content) per jet

TABLE XX. Monte Carlo prediction of the fraction of events (in percent) before tagging, which are $Wb\bar{b}$ and $Wc\bar{c}$ as a function of jet multiplicity. The uncertainty reflects Monte Carlo statistics only. The systematic uncertainty is discussed in the text.

Jet multiplicity	$Wb\bar{b}$ (%)	$Wc\bar{c}$ (%)
1 jet	0.74±0.03	1.66±0.05
2 jets	1.46±0.11	3.43±0.18
3 jets	2.95±0.42	4.83±0.67

from approximately 1.3% (3.3%) to 2.2% (6.0%). We therefore assign a ±0.8 error (the difference between 2.2 and 1.4) on the 1.4 factor used to rescale the HERWIG gluon splitting rate. Notice that using the upper bound would lead to a predicted tagging rate in the 50-GeV jet and sum E_T above 300-GeV samples significantly higher than the one we observe (see Fig. 28). In addition, we assign a ±40% uncertainty to the dependence on the number of jets in the event based on the shape in Fig. 28(a). Adding the uncertainty on the heavy-flavor content of the positive L_{xy} excess (±35%) and the uncertainty on the SVX tagging efficiency (±30%), we derive a total uncertainty of ±80% on the predicted $Wb\bar{b}$ and $Wc\bar{c}$ rates using method 2.

The predicted rate from mistags only is shown in the third row of Table XXI. The uncertainty includes both the systematic uncertainty on the negative L_{xy} tagging-rate prediction and the uncertainty on the assumption that non-heavy-flavor tags have an L_{xy} distribution symmetric about $L_{xy}=0$. As mentioned in Sec. V B 1, the negative L_{xy} tags are approximately 35% from real
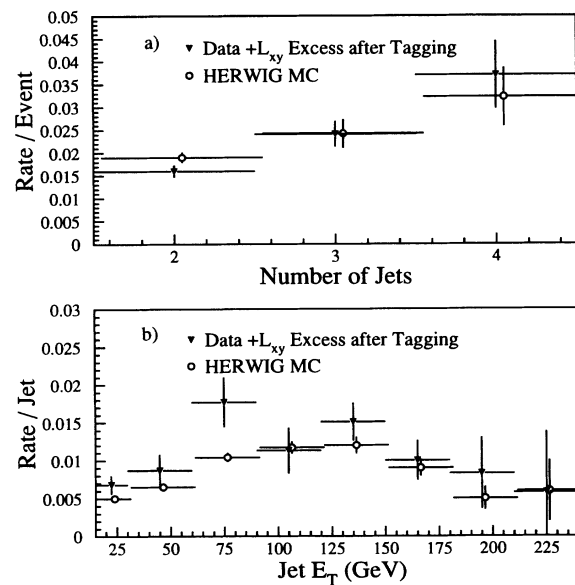

FIG. 28. The excess positive L_{xy} tagging rate in data (solid triangles) and a HERWIG Monte Carlo simulation of jets which contain heavy flavor (open circles) for (a) the 50-GeV jet-trigger sample as a function of observed jet multiplicity and for (b) in the sample with scalar sum E_T above 300 GeV as a function of observed jet E_T. The errors shown are statistical only.

TABLE XXI. Summary of background and observed tags.

	Source	$W + 1$ jet	$W + 2$ jets	$W + \geq 3$ jets
(1)	$W b\bar{b}, W c\bar{c}$ + Mistags, Method 1	12.7±1.7	4.86±0.63	1.99±0.26
(2)	$W b\bar{b}, W c\bar{c}$ only, Method 2	2.7±2.2	1.05±0.85	0.37±0.31
(3)	Mistags only, Method 2	4.8±2.5	1.85±0.98	0.76±0.43
(4)	$W b\bar{b}, W c\bar{c}$ + Mistags, Method 2	7.5±3.3	2.90±1.30	1.13±0.53
(5)	Wc	2.4±0.8	0.66±0.27	0.14±0.07
(6)	$Z \to \tau\bar{\tau}, WW, WZ$	0.20±0.10	0.19±0.09	0.08±0.04
(7)	Non-W, including $b\bar{b}$	0.50±0.30	0.59±0.44	0.09±0.09
(8)	Total Method 1	15.8±2.1	6.3±0.8	2.30±0.29
(9)	Total Method 2	10.6±3.7	4.3±1.4	1.44±0.54
(10)	Events Before Tagging	1713	281	52
(11)	Observed Tagged Events	8	8	6

heavy-flavor decays. Therefore, there is some double counting of the true heavy-flavor background by using the addition of rows (2) and (3) for the method-2 background estimate. This effect is small compared to the systematic error on the method-2 background and tends to cause the background to be an overestimate. The sum of $W b\bar{b}$, $W c\bar{c}$ and mistags, as estimated using this second method, is shown in row (4) of Table XXI.

We now proceed to the evaluation of the remaining backgrounds listed at the beginning of this section and which are common to both methods. The background from $\bar{p}p \to W +$ charm [45], which arises from the flavor excitation processes $sg \to Wc$ and $dg \to Wc$, is determined by using the HERWIG and VECBOS Monte Carlo generators [25,26] to compute the expected fraction of W+multijet events produced by this process and the tagging rate for these events. The results of this calculation are shown in row (5) of Table XXI, where the estimated uncertainty is dominated by the uncertainty in the strange sea content in the proton (±30%), computed by examining a wide range of different structure functions [46].

The background from non-W sources, including direct $b\bar{b}$, is determined directly from the data by studying the isolation of lepton (electron or muon) candidates in both the low E_T region ($E_T \leq 15$ GeV) and the high E_T region ($E_T \geq 20$ GeV) [17]. The total number of non-W background events in the signal region (high E_T and isolated lepton) is estimated as the number of nonisolated lepton candidates in the high E_T region scaled by the ratio of isolated to nonisolated lepton candidates in the low E_T region, which is dominated by background. In order to predict the number of tagged non-W events in the signal region, we scale the estimate by the tagging rate measured in the background dominated (low E_T region with isolated lepton) region.

Contributions expected from WW or WZ production with $W \to c\bar{s}$ or $Z \to b\bar{b}$, and from $Z \to \tau\bar{\tau}$ are estimated with ISAJET and are found to be small. The cross sections used to normalize the diboson expectations are taken from Refs. [29,32], and we assign a systematic uncertainty of 30%, which is the difference between the leading-order and next-to-leading order calculations of diboson

production. The result of these calculations is shown in the sixth row of Table XXI.

The total backgrounds using the above two methods are listed in the eighth and ninth rows of Table XXI. As expected, the rates using method 2 are slightly lower than the predicted rates from method 1, since the expected heavy flavor content of W+multijet events is smaller than in inclusive-jet events.

To be conservative, the background estimate is taken to be the result of the first method. For the jet-vertexing algorithm, the estimated background when requiring $N_{\text{jet}} \geq 3$ is 2.3±0.3. The background estimate for the jet-probability algorithm is 2.3±0.3, and for the d-ϕ algorithm the background is estimated to be 1.8±0.2.

4. Observed SVX tags in the W+multijet sample

The b-tagging algorithms are now applied to the W candidate data sample. The $c\tau_{\text{eff}}$ distribution [see Eq. (2)] for the vertexed jets in the W+multijet sample in the data is shown in Fig. 29. The data are shown as points, and the expected distribution for a sample of Monte Carlo b jets is overlaid. The tags in the W+multijet sample are consistent with coming primarily from heavy-flavor jets. The events with a tagged jet ($c\tau_{\text{eff}} \geq 0$) are summarized in the last line of Table XXI as a function of jet multiplicity. The tags in the W events with 1 and 2 jets are expected to be dominantly from sources other than $t\bar{t}$ decay (see Table XXI). There are four negative L_{xy} tags in the $W + 1$ and 2 jet sample, which is consistent with the expectation of 6.6±2.7 given in Table XXI. Figure 30 shows the number of W candidates (from Table XIV), the number of events tagged by the jet-vertexing algorithm, and the background, as a function of jet multiplicity in the event.

In the signal region, $W + \geq 3$ jet events, there are six events tagged using the jet-vertexing algorithm. The $c\tau_{\text{eff}}$ values for these six events are highlighted in Fig. 29. The other two tagging algorithms yield consistent results: The jet-probability algorithm observes four tagged events and the d-ϕ algorithm observes five. No negative L_{xy} jet-vertexing tags are observed in the $W + \geq 3$ jets sample.
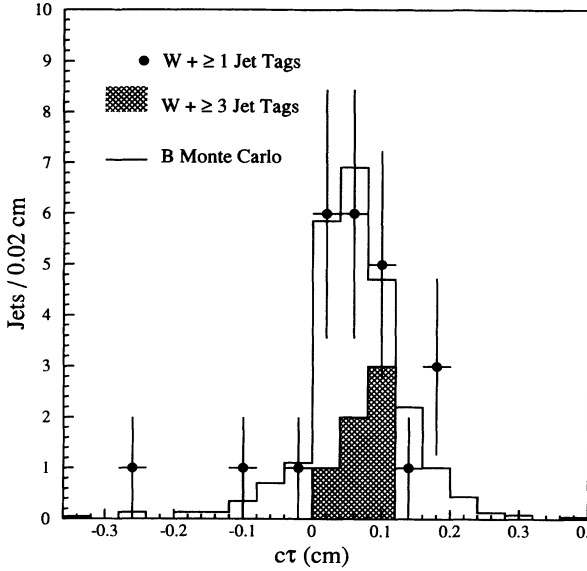
FIG. 29. The $c\tau_{\text{eff}}$ distribution for jets with a secondary vertex in the W+jets data (points with errors) compared to b quark jets from Monte Carlo $t\bar{t}$ events (histogram normalized to data). The shaded histogram is the $W+\geq 3$ jets tags in the data. A $W+2$ jet event with a $c\tau_{\text{eff}}=1.2$ cm and a $W+1$ jet event with a $c\tau_{\text{eff}}=-0.41$ cm are not shown.

5. Correlations among the SVX tagging algorithms

A study of the correlations among the different SVX tagging algorithms provides an additional check on whether the observed tags result from heavy-flavor jets or from the misidentification of light-quark or gluon jets. We have verified that there are large correlations among
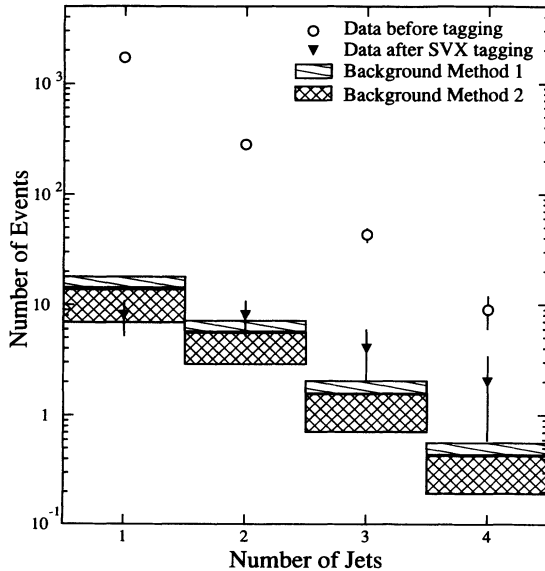

FIG. 30. The W+jets distribution observed in the data. The open circles are before SVX tagging and the solid triangles are after SVX tagging. The cross-hatched boxes are the two after tagging background estimates. See text for description.

the algorithms for real heavy-flavor decays, as one would expect, and there are small correlations among the algorithms for mistags. In the generic-jet sample, we find that jets which are tagged with positive L_{xy} by the jet-vertexing algorithm are also tagged by at least one of the other tagging algorithms approximately 50% of the time, and by both approximately 25% of the time. As previously stated, these tags are dominated by heavy-flavor production in jets.

An equivalent to the negative L_{xy} tag for the jet-vertexing algorithm, which measures the rate of mistags, has been defined for the other two algorithms. For the jet-probability algorithm a selection is made using tracks which have negative impact parameters. For the d-ϕ algorithm, an effective flight distance is estimated and tags which appear to come from behind the primary vertex are selected. In a sample of jet-vertexing tagged events with negative L_{xy}, at least one of the other two algorithms has an equivalent negative L_{xy} tag about 20% of the time, and both occur approximately 3% of the time. These tags are dominated by tracking mistakes, which accounts for the smaller overlap among the algorithms.

The correlations among the three algorithms on $t\bar{t}$ events are studied using a $t\bar{t}$ Monte Carlo sample. Since $t\bar{t}$ events have two b quarks, it is possible for two algorithms to tag different jets in a single event. In the Monte Carlo sample, about 75% of the events tagged by the jet-vertexing algorithm are also tagged by at least one of the other algorithms, approximately 30% are tagged by both.

In the $W+\geq 3$ jet data sample, six events are tagged by the jet-vertexing algorithm. Of the six, three are tagged by the jet-probability algorithm, four by the d-ϕ algorithm, and two of these are tagged by all three algorithms. In addition to the six events, there are two events, one that is tagged only by the jet-probability algorithm and one that is tagged only by the d-ϕ algorithm. Within statistics, this is consistent with what is expected from sources of heavy flavor. If all six jet-vertexing tags were due to tracking errors, we would expect approximately 1 of these events to be tagged by one of the other two algorithms. In contrast, five of the six events are tagged by at least one other algorithm.

C. Search for $t\bar{t}$ using soft leptons

An alternative way to tag b quarks is to search for leptons produced in decays of the b quark through $b \rightarrow l\nu_l X$ ($l=e$ or μ), or $b \rightarrow c \rightarrow l\nu_l X$ (cascade decays). In this section, we present a search for additional leptons in the W+jets sample described in Sec. V A. Because these additional leptons in top events are expected to have low P_T, we refer to them as "soft lepton tags" (SLT's) (see Fig. 31). In order to maintain high efficiency for leptons from cascade decays, the lepton P_T threshold in the search is set at 2 GeV/c.

The search presented in this section is a dilepton search optimized for the detection of one lepton from bottom or charm decay. On the other hand, the requirements of the high-P_T dilepton search described in Sec. IV are designed for detection of two leptons from W decays.
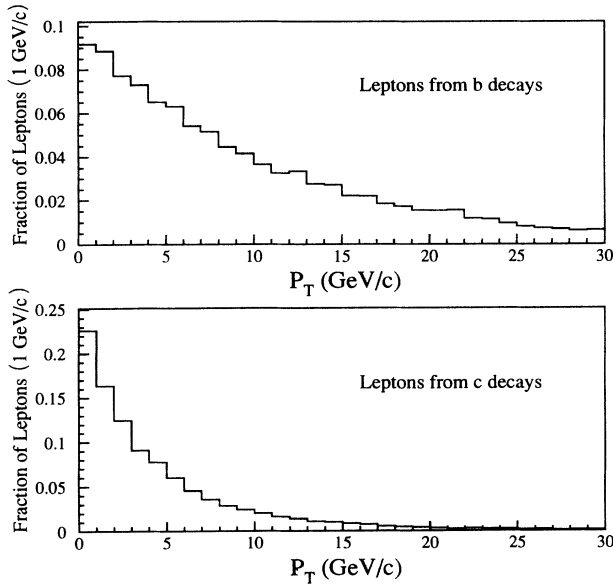
FIG. 31. P_T spectra of leptons from the decay of b and c quarks in top Monte Carlo events ($M_{top} = 160$ GeV/c^2).

There is a small overlap in the acceptance for top events of the two searches. To allow the results of these two searches to be combined (see Sec. VI), lepton pairs passing the requirements of the high-P_T dilepton search are excluded from the SLT search described here.

1. Description of the algorithm and tagging efficiency

To search for electrons from b and c decays, we extrapolate each particle track reconstructed in the CTC to the calorimeter and attempt to match it to a CES shower cluster. The matched CES clusters are required to be consistent in size, shape, and position with expectations for electron showers. The efficiency of this and other selection criteria is determined from a sample of electrons produced by photon conversions, selected using CTC tracking information only. The P_T distribution and the distribution of the ratio of electromagnetic calorimeter energy to CTC-measured momentum (E/P) for these electrons are shown in Figs. 32(a) and 32(b). The distributions of the difference between the extrapolated position of the CTC track and the CES-cluster position in the azimuthal direction (Δx) and parallel to the beam direction (Δz) are shown in Figs. 32(c) and 32(d), respectively. In addition, the specific ionization (dE/dx), measured in the CTC, is required to be consistent with the electron hypothesis. Figure 33(a) shows the dE/dx response of the CTC for electrons from the photon conversion sample and for an electron-depleted (hadron) sample selected by requiring $E/P < 0.5$. Electron candidates must also match to an energy deposition in the CPR corresponding to at least four minimum-ionizing particles. Figure 33(b) shows the distribution of the CPR response to electrons and to the hadron sample. The efficiency of these electron requirements, measured using the photon conversion
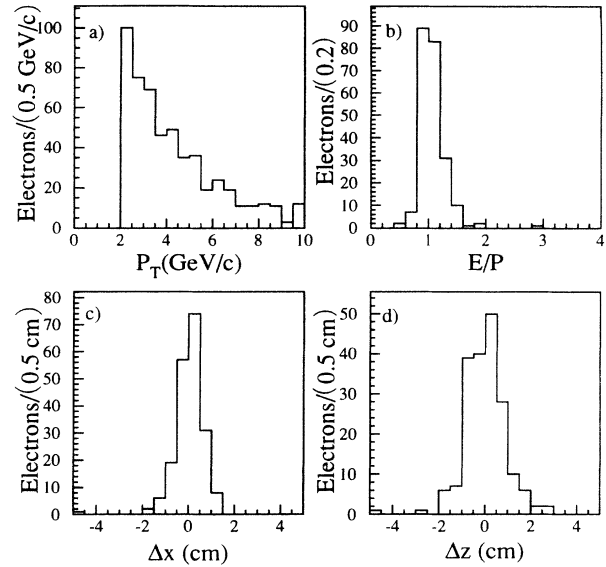

FIG. 32. Distributions for a sample of electrons from photon conversions of (a) P_T of the electron candidate, and (b) the ratio of calorimeter energy to CTC-measured momentum (E/P). Also shown are the distribution of the difference between the extrapolated position of the CTC track and the CES-cluster position in the (c) azimuthal direction (Δx) and (d) in the direction parallel to the beam (Δz).
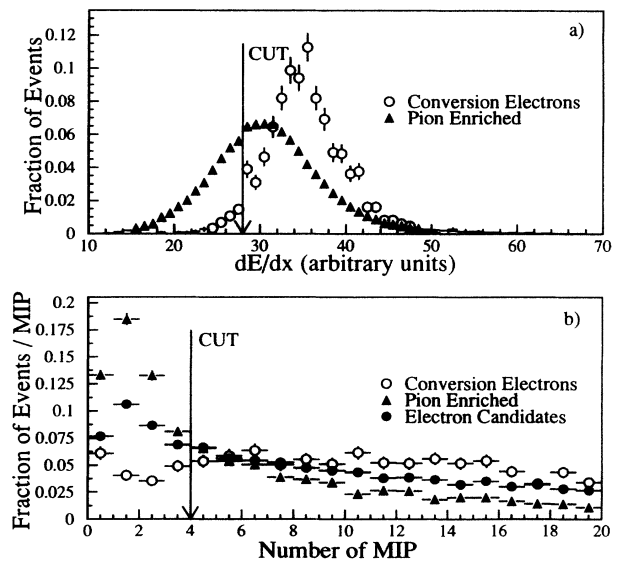

FIG. 33. The distribution for a conversion-electron sample and a pion enriched sample of (a) dE/dx in the CTC, and (b) energy deposition in the CPR, in units of the energy deposited for a minimum-ionizing particle (MIP). Also shown in (b) is the distribution of CPR response for, a mixture of electrons and hadrons, which pass all the other electron requirements except the CPR requirements. The hadron sample has been selected by requiring $E/P < 0.5$.
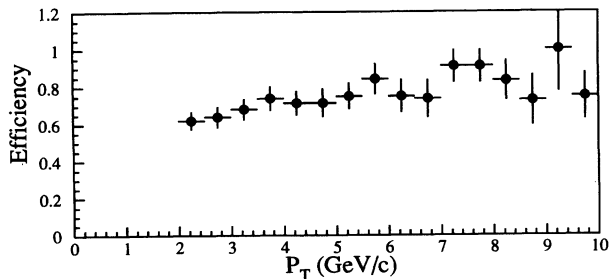
FIG. 34. Efficiency for the isolation-independent electron selection requirements as a function of P_T.

sample, is shown in Fig. 34 as a function of the P_T of the electron.

In addition, we require $0.7 < E/P < 1.5$ and the energy in the hadronic compartment of the calorimeter to be consistent with expectations for electrons (E_{had}/E_{EM} < 0.1). The calorimeter energy associated with a track is the energy deposited in the calorimeter tower to which the track points. However, if the track extrapolates to within 2 cm of a tower boundary, the energy of the neighboring tower is also included. This is in contrast to the algorithm used in the selection of high-P_T electrons from W decays, where energies are summed over three calorimeter towers (see Sec. III B). The energy-clustering algorithm used here is optimized for detection of electrons from b or c decays. Since these electrons are not isolated, the efficiency for the E/P and E_{had}/E_{EM} requirements must be calculated using a Monte Carlo model (see Fig. 35). For a Monte Carlo sample with $M_{top} = 160$ GeV/c^2, the average efficiency is found to be $(53\pm3)\%$ and $(23\pm3)\%$ for electrons from b and c decays, respectively, where the errors reflect statistical uncertainty only. Uncertainty in the calorimeter modeling
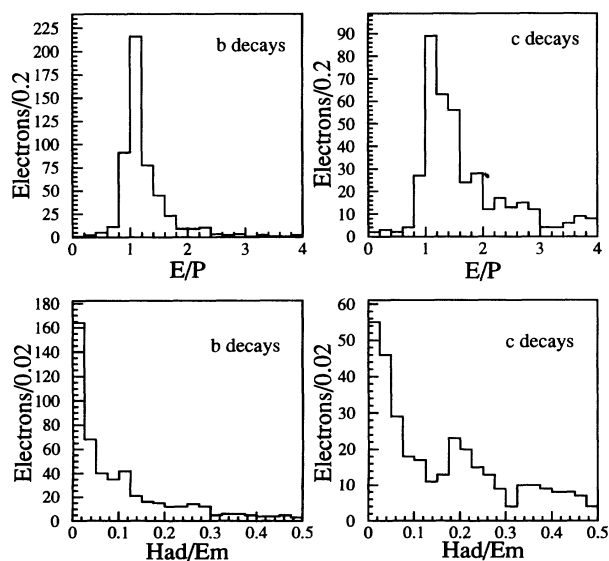
of nearby hadronic showers results in an additional 10% systematic uncertainty on these efficiencies.

To identify muons from b or c decays, track segments reconstructed in the CMU system and the CMP are matched to tracks in the CTC. Approximately 84% of the solid angle for $|\eta| < 0.6$ is covered by the CMU system, 63% by the CMP system, and 53% by both. Since muons of P_T below approximately 2.8 GeV/c are expected to stop in the steel before reaching the CMP drift chambers, only the CMU system is used in identifying muons with $2 < P_T < 3$ GeV/c. Muon candidate tracks with $P_T > 3$ GeV/c that are within the fiducial volume of both the CMU and CMP systems are required to be well matched to track segments in both the CMU system and CMP.

The reconstruction efficiency of CMU and CMP track segments is measured using samples of muons from $J/\psi \rightarrow \mu^+\mu^-$ and $Z \rightarrow \mu^+\mu^-$ decays. The efficiency is found to be $(98\pm1)\%$ and $(96.1\pm0.2)\%$ for CMP and the CMU system, respectively. These samples are also used to measure the efficiency of the matching requirements between CTC tracks and CMU-CMP track segments. Efficiencies are shown as a function of muon P_T in Fig. 36 for the three cases: muons in the CMU system only, muons in CMP only, and muons in both the CMU system and CMP. Track segments are required to match in position and direction (ϕ) with the extrapolated CTC track. The ϕ measurements in the muon chambers include a non-Gaussian component to the resolution, which becomes more important relative to multiple scattering as the P_T increases. This introduces a small P_T-dependent inefficiency (see Fig. 36). We do not require ϕ matching for muon candidates found in both the CMU system and CMP, and the ϕ-matching requirements are relaxed at

FIG. 35. E/P and E_{had}/E_{EM} for electrons from b and c decays of $P_T > 2$ GeV/c in the $t\bar{t}$ Monte Carlo simulation ($M_{top} = 160$ GeV/c^2).
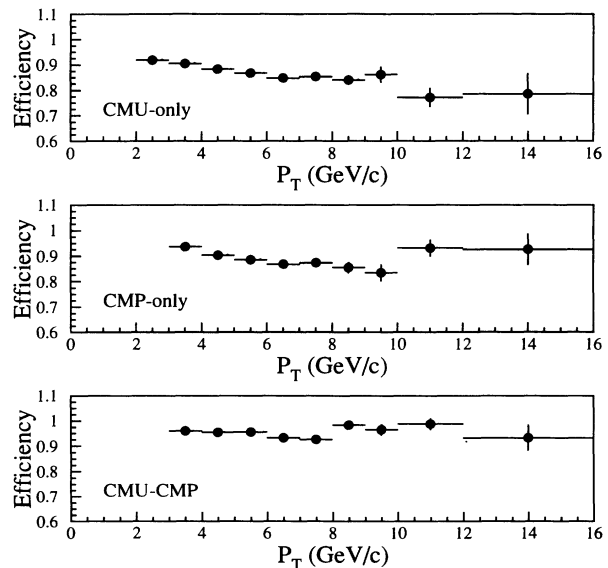

FIG. 36. Efficiencies as a function of P_T for the CTC-to-CMU and/or CMP matching criteria as measured with a sample of $J/\psi \rightarrow \mu^+\mu^-$ decays.

high momentum ($P_T > 10$ GeV/c for CMP, and $P_T > 20$ GeV/c for the CMU system).

To maintain high efficiency for nonisolated muons from b and c decays, we do not impose the minimum-ionizing requirements described in Sec. III C, which are intended for isolated muons from W decay. These requirements are designed to reduce high-P_T hadronic punch through, which is also effectively reduced by requiring a match between the CTC track and the CMP track segment. Figure 37 shows the energy deposited in the CHA for two samples of muon candidates with $P_T > 15$ GeV/c. The solid histogram shows the CHA energy distribution for muons that are identified in both the CMU system and CMP, and the dashed histogram shows the distribution for muons identified in the CMU system only. The higher rate in the high-energy tail of the CMU-only distribution is caused by hadronic punchthrough that is greatly reduced by the CMP requirement. In order to reduce the punchthrough background in the regions not covered by the CMP system, we apply an isolation-dependent requirement on muon candidates with $P_T > 6$ GeV/c that do not have a matching CMP track segment; we require $E_{had} < 6$ GeV $+ \sum p$, where E_{had} is the hadronic energy of the tower traversed by the muon and $\sum p$ is the scalar sum of the momenta of all tracks within a cone of 0.2 of the muon candidate. No requirement is applied for lower-P_T muons since at low momentum, calorimeter information is not as effective at rejecting the background events from hadron punchthrough. Monte Carlo studies indicate that the requirement described above is $> 98\%$ efficient for real muons from b and c decays in top events.

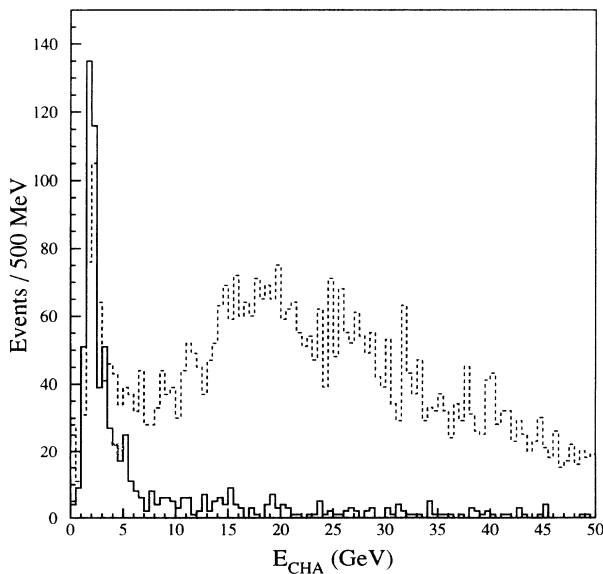To calculate the acceptance for top events, we use the

FIG. 37. CHA energy for muon candidates, which are identified both in the CMU and CMP detectors (solid) and for muon candidates identified in just the CMU detector (dashed). The muon candidates populating the high-energy tail in the CMU-only distribution are due to hadrons which punch through the calorimeter.

ISAJET Monte Carlo generator, modified to use the CLEO Monte Carlo program for the decay of B mesons, and a simulation of the CDF detector. The efficiency for detecting an additional electron or muon of $P_T > 2$ GeV/c in top events is $\epsilon_{tag} = (16 \pm 2)\%$, resulting in the number of expected tagged $t\bar{t}$ events given in Table XXII. Of these events, 37% will contain an electron tag, and 63% will contain a muon tag, independent of top mass. For the $t\bar{t}$ Monte Carlo sample with a top mass of 140 GeV/c^2, 53% of these leptons come directly from b decay, 35% come from the c quarks from b decay, and the remaining 13% come from the W in the reaction $t \to Wb$. These fractions are very weakly dependent on the assumed top mass. The Monte Carlo simulation also predicts that a small fraction of tagged top events (approximately 7%) should contain more than one reconstructed soft lepton. Note that ϵ_{tag} defined above does not include the small (approximately 4%) probability of misidentifying a hadron as a lepton in top events. Systematic uncertainties in the lepton tagging rate arise from uncertainties in the muon and electron detection efficiencies (6%), uncertainties in the b and c quark semileptonic branching ratios (10%), uncertainty in the fragmentation of b quarks into hadrons (5%), and the finite statistics of our Monte Carlo samples (7%).

As a further check of the efficiency of the SLT tagging procedure, we search for SLT tags the inclusive electron sample described in Sec. V B. We estimate that the fraction of electrons in this sample that are from semileptonic b decays in $b\bar{b}$ events is $F_b = (37 \pm 8)\%$. The sample of jets recoiling against these electrons is therefore enriched in b quarks. We find 767 SLT tags in the 55 061 jets with $P_T > 10$ GeV/c and $|\eta| < 2$ in this sample. The background from fake leptons in this sample (see Sec. V C 2), is estimated to be 310 ± 62, so that the excess of SLT tags over background is 457 ± 68. Theoretical calculations [44] suggest that the fraction of recoil jets in $b\bar{b}$ events that actually contain a b or $\bar{b}$ quark is $F_{rec} = (49 \pm 15)\%$. Monte Carlo studies yield an SLT tagging efficiency $\epsilon = (7.0 \pm 1.3)\%$ for these jets. Therefore, the background-subtracted expected number of SLT tagged jets in this sample is the product 55 061 $\times (\epsilon F_b F_{rec}) = 700 \pm 300$, in good agreement with the number of observed SLT tags.

2. Backgrounds in the soft lepton search

To measure the hadron rejection of the electron requirements, we study a large sample of tracks in generic

TABLE XXII. Summary of the soft lepton tagging efficiency (ϵ_{tag}) and the expected number of $t\bar{t}$ events with a soft lepton tag in the $W + 3$ or more jets data sample. We define ϵ_{tag} as the probability of finding at least one lepton (electron or muon) in top events with three or more jets.

M_{top} GeV/c^2	ϵ_{tag}	Expected events
120	0.165±0.025	6.33±1.26
140	0.159±0.024	3.48±0.70
160	0.152±0.023	1.85±0.34
180	0.159±0.024	1.05±0.18

jet events from a mixture of 20, 50, 70, and 100 GeV inclusive-jet triggers, (see Sec. V B 3). We define a "track-tag rate" as the ratio of the number of tracks passing the electron selection criteria described in Sec. V C 1 to the total number of CTC tracks that extrapolate to the fiducial region instrumented by both the CES and the CPR. The track-tag rate is parametrized as a function of P_T and $\sum p /p$, where $\sum p$ is the scalar sum of the momenta of all other tracks within a cone of 0.2 at the calorimeter in η-ϕ space, and p is the momentum of the track (see Fig. 38). To be included in the sum, tracks have to reach the calorimeter, i.e., have $P_T > 350$ MeV/c, since lower momentum tracks curl up in the magnetic field. The quantity $\sum p /p$ is a measure of the relative isolation of the track. The probability for a track to satisfy the electron selection criteria depends on isolation because nearby particles can deposit energy in the tower traversed by the particle, and this extra energy affects the E/P and E_{had}/E_{EM} measurements.

Similarly, the track-tag rate for muons, shown in Fig. 39, is defined to be the ratio of the number of tracks in generic jet events passing the muon selection criteria of Sec. V C 1, to the number of tracks extrapolating to the fiducial region instrumented by the CMU system and/or CMP. A trigger bias is present in the generic-jet sample because the energy of jets containing a muon (whether real or fake) systematically tends to be measured low in the calorimeter. To select an unbiased set of tracks in generic-jet events, we only consider tracks that are well separated from at least one jet that satisfies the hardware trigger requirement. Since the muon selection requirements are only very weakly dependent on isolation, we have found no need to parametrize the muon track-tag rate in terms of isolation.
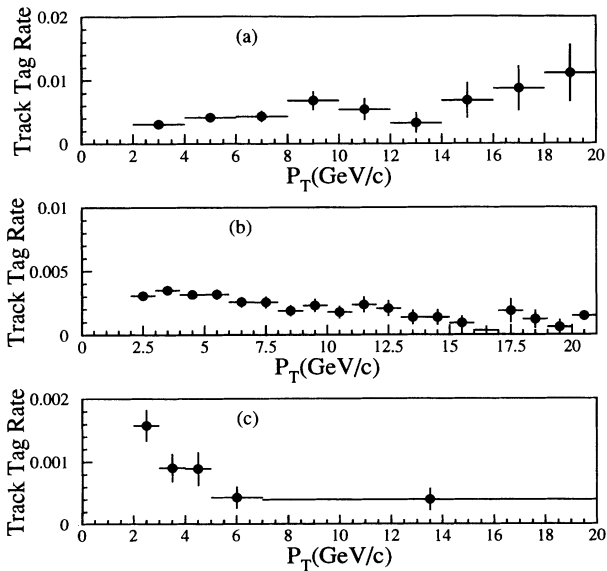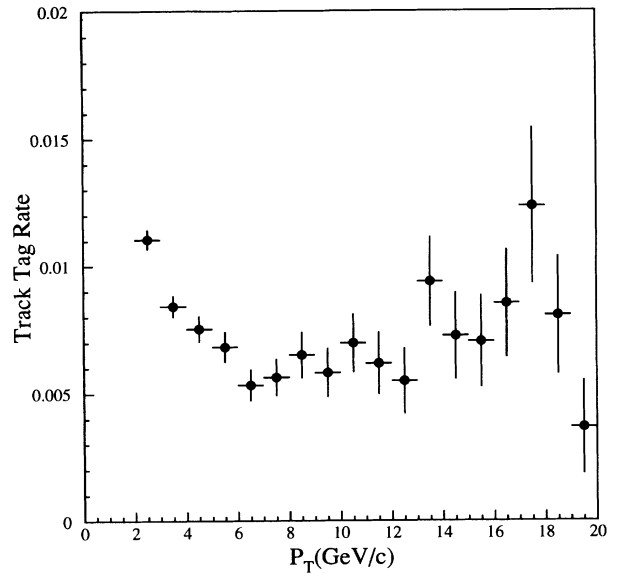

FIG. 39. Track-tag rate for muons in generic jets.

Possible sample-dependent variations of the electron and muon tag rate calculations are studied by examining samples of minimum bias, photon + jets, Z +jets, six jets, high $\sum E_T$ ($\sum E_T \geq 300$ GeV) events, and data collected with inclusive-jet triggers with E_T between 20 and 100 GeV. Comparisons between the lepton yields in these data sets and expectations from the track-tag rate parametrizations are given in Table XXIII. Based on these studies, we assign a 10% (15%) systematic uncertainty on the tag-rate prediction for muons (electrons).

Because of the presence of leptons from b and c quarks in the generic-jet sample, as discussed in Sec. V B 3, these tag rates represent an overestimate of the backgrounds due to misidentification. By searching for SVX tags in jet events containing a lepton candidate of $P_T > 2$ GeV/c, we estimate that $(25\pm12)\%$ of the SLT tags in the generic-jet sample are due to real leptons from b or c quark decays.

In the determination of the background in the W +jet sample, we assume that the heavy-flavor content (b and c quarks) of generic jets is equal to that of jets in W events. This is equivalent to the "method 1" background estimate for the SVX tag analysis described in Sec. V B 3. As was discussed in that section, this assumption is a conservative one that tends to overestimate the amount of background in W events. The background is estimated by applying the tag rates measured in generic jets to the track spectrum found in W events. This estimate includes candidates that are not produced by heavy flavor (misidentified pions, muons from decays in flight, etc.), as well as background arising from generic heavy-flavor production in association with a W boson ($Wb\bar{b}$ and $Wc\bar{c}$).

Other backgrounds arise from Drell-Yan production, WW, WZ, and ZZ boson production, $Z \to \tau\tau$ decays, double semileptonic decays in $b\bar{b}$ events, and direct production of W +charm. To minimize the Drell-Yan background, we reject isolated, opposite-sign, same-flavor lep-

FIG. 38. Track-tag rates for the electron search for tracks satisfying (a) $\sum p /p < 0.2$, where $\sum p$ is the scalar sum of the momenta of all other tracks within a cone of 0.2, and p is the momentum of the track. (b) $0.2 < \sum p /p < 5$. (c) $\sum p /p > 5$.

TABLE XXIII. A comparison of the observed number of lepton candidates in different samples with the prediction from the track-tag rate parametrizations. The track-tag rate parametrizations were obtained from a mixture of the 20-, 50-, 70-, and 100-GeV inclusive-jet triggers. A trigger bias is present in the muon yields for the inclusive-jet triggers because the energies of jets containing hadrons that do not interact in the calorimeter are measured systematically low. For this reason, only tracks well separated from a trigger-jet are considered in the muon analysis. The statistical uncertainties on the predictions are negligible.

Sample	Number of electrons		Number of muons	
	Predicted	Observed	Predicted	Observed
100-GeV jet trigger	598	531	487	471
70-GeV jet trigger	621	631	511	546
50-GeV jet trigger	502	531	374	375
20-GeV jet trigger	757	785	556	557
16-GeV photon sample	30	37	129	128
Six-jet sample	65	60	143	144
$\sum E_T$	259	203	762	682
Minimum bias	25	21	50	47
Z+jets	1.4	2	2.7	4

ton pairs. The remaining background is estimated by scaling the number of removed Drell-Yan candidates by the inefficiency of the isolation requirement $(5\pm3)\%$, as measured on a sample of Z events. The diboson and $Z \rightarrow \tau\tau$ backgrounds are estimated using the ISAJET Monte Carlo generator and a full simulation of the CDF detector. Based on comparisons of the jet multiplicity in W+jets data with the ISAJET prediction, we assign a systematic uncertainty of 30% to the background estimate due to the uncertainties in the modeling of the jet multiplicity in Z and diboson events. The cross sections used to normalize the diboson expectations are taken from Refs. [29,32] [$\sigma(WW)=9.9$ pb, $\sigma(WZ)=2.8$ pb, and $\sigma(ZZ)=1.1$ pb]. A systematic uncertainty of 30% is assigned to the expected number of events, corresponding to the difference between the leading-order and next-to-leading-order calculations of diboson production cross sections. The $b\bar{b}$ and W+charm backgrounds are calculated using the method described in Sec. V B 3.

The results of the background calculation are summarized in Table XXIV. The "fakes+ $Wb\bar{b}$ + $Wc\bar{c}$ " entry in Table XXIV is the background estimated using the track-tag rates as parametrized in inclusive-jet events, under the conservative assumption that the heavy-flavor content of jets in W events is the same as that of generic jets.

Alternatively, the SLT background in the W+jets sample can be estimated using the equivalent of the "method-2" estimate of Sec. V B 3. In this case, the fake lepton and the $Wb\bar{b}$ + $Wc\bar{c}$ backgrounds are considered separately. The fake background is estimated by scaling down the track-tag rate parametrizations by $(25\pm12)\%$, which corresponds to the estimated fraction of SLT tags in jet events, which are due to semileptonic b or c decays. The $Wb\bar{b}$ + $Wc\bar{c}$ backgrounds are estimated using the same method described in Sec. V B 3, and for the SLT analysis are 2.3$\pm$1.8, 1.0$\pm$0.8, and 0.3$\pm$0.2 events for the W+1, 2, and $\geq$3 jets samples, respectively. The re-

sulting total background estimates, for each of these jet-multiplicity samples, are 29.1$\pm$4.2, 8.7$\pm$1.4, and 2.7$\pm$0.4 events. As expected, the method-2 background estimates are lower than the method-1 background estimates presented in Table XXIV.

3. Observed SLT tags in the W+multijet sample

Applying the lepton-identification algorithms to the W sample results in the number of tagged events listed in Table XXIV. The number of events with additional leptons found in the W+1 and W+2 jet samples, which should have a small contribution from $t\bar{t}$ production, is in agreement with the background expectation. Among the 52 events with three or more jets, we find that seven of them are tagged, with an expected background of 3.1$\pm$0.3. When the P_T requirement of the soft lepton is increased to 4 GeV/c, four events are tagged and the expected background is decreased to 1.7$\pm$0.2. This change causes the number of expected SLT tags from $t\bar{t}$ events to decrease by 22 (21)% for a top mass of 120 (160) GeV/c^2. In Fig. 40 we compare the expected P_T spectrum of tags in the W+1 jet sample with data. In Fig. 41 we display the same comparison, including the expected top contribution, for the $W\pm \geq 3$ jets sample.

Of the seven tagged events, three are also tagged by the SVX analysis. Table XXV lists the characteristics of the ten events with at least one SLT or SVX tag. (Typical resolutions for these quantities can be found in Secs. II and III and Ref. [47].) One of the events tagged by both SLT and SVX (45 047 and 104 393) is an event in which the SLT tag consists of an isolated high-P_T electron candidate. This event passes all of the requirements of the high-P_T dilepton selection described in Sec. IV A, except that the electron is near the edge of a calorimeter tower and fails the E/P and χ^2_{strip} requirements for electron identification in the dilepton analysis (while passing the somewhat different electron requirements for electron

TABLE XXIV. Summary of SLT backgrounds as a function of jet multiplicity.

| Source		$W+1$ Jet	$W+2$ Jets	$W+ \geq 3$ Jets
Fakes $+ Wbb + Wc\bar{c}$	e tags	9.9 ± 1.5	2.9 ± 0.4	0.88 ± 0.13
	μ tags	19.2 ± 1.9	5.9 ± 0.6	1.82 ± 0.18
	$e+\mu$ tags	29.1 ± 2.9	8.8 ± 0.9	2.70 ± 0.27
bb	e tags	0.8 ± 0.6	0.14 ± 0.10	0.03 ± 0.02
	μ tags	0.9 ± 0.6	0.14 ± 0.10	0.03 ± 0.02
	$e+\mu$ tags	1.7 ± 1.2	0.28 ± 0.20	0.05 ± 0.03
Diboson	e tags	0.25 ± 0.12	0.11 ± 0.06	0.03 ± 0.02
	μ tags	0.28 ± 0.13	0.03 ± 0.02	0.01 ± 0.01
	$e+\mu$ tags	0.53 ± 0.25	0.14 ± 0.08	0.04 ± 0.03
$Z \to \tau\tau$	e tags	0.37 ± 0.13	0.11 ± 0.05	0.08 ± 0.03
	μ tags	0.30 ± 0.11	0.07 ± 0.04	0.06 ± 0.03
	$e+\mu$ tags	0.67 ± 0.24	0.18 ± 0.09	0.14 ± 0.06
Drell-Yan	e tags	0.15 ± 0.10	0.03 ± 0.03	0.03 ± 0.03
	μ tags	0.15 ± 0.10	0.03 ± 0.03	0.03 ± 0.03
	$e+\mu$ tags	0.30 ± 0.20	0.05 ± 0.05	0.05 ± 0.05
$W+c$	e tags	0.4 ± 0.1	0.10 ± 0.03	0.02 ± 0.01
	μ tags	1.4 ± 0.5	0.32 ± 0.08	0.06 ± 0.02
	$e+\mu$ tags	1.8 ± 0.6	0.42 ± 0.11	0.08 ± 0.03
Total	e tags	11.9 ± 1.6	3.4 ± 0.4	1.1 ± 0.2
	μ tags	22.2 ± 2.1	6.5 ± 0.6	2.0 ± 0.2
	$e+\mu$ tags	34.1 ± 3.3	9.9 ± 1.0	3.1 ± 0.3
Events before tagging		1713	281	52
Events after tagging	e tags	17	2	4
	μ tags	16	10	3
	$e+\mu$ tags	33	12	7
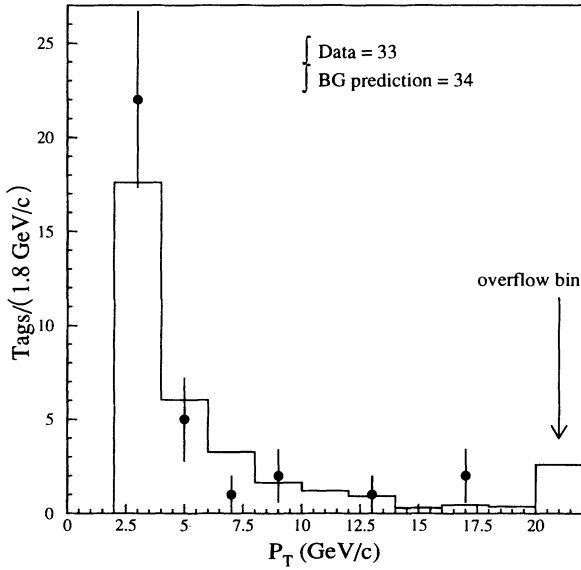
FIG. 40. The P_T spectrum of tags in the $W+1$ jet sample compared with expectations from the background calculation. The data are the points and the background is the solid histogram. The background is obtained from the method-1 calculation.
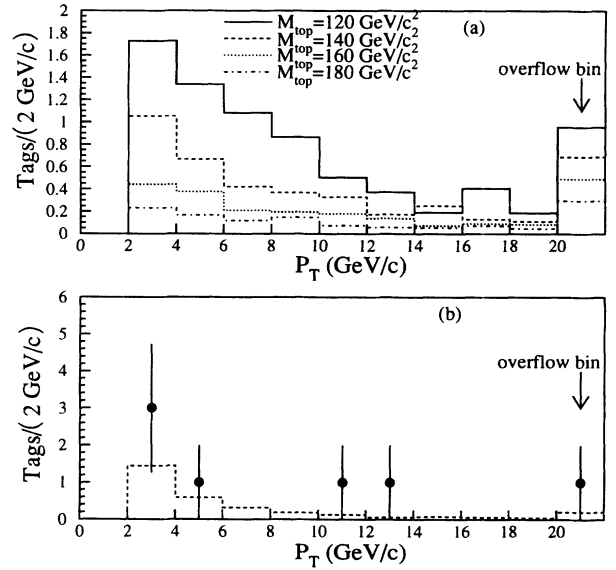
FIG. 41. (a) The expected P_T spectra of tags from top events in the $W+ \geq 3$ jets sample for different top masses. The spectra are normalized using the top cross-section predictions from Ref. [10]. (b) The P_T spectrum of leptons tagged by the SLT analysis in the $W+ \geq 3$ jets sample (points) compared with the background expectations from the method-1 calculation.

TABLE XXV. Characteristics of the ten tagged lepton+jets events. Jets tagged by the SVX jet-vertexing algorithm (SLT algorithm) are labeled with "SVX" ("SLT"). The jet energies and $\not{E}_T$ are not corrected for calorimeter nonlinearities, etc.

	P_T (GeV/c)	η	ϕ (rad)		P_T (GeV/c)	η	ϕ (rad)
Run 43096 event 47223				**Run 42517 event 44047**			
electron (−)	33.1	−0.81	0.77	muon (+)	49.7	0.86	5.72
Jet 1 (SVX)	101.4	0.02	0.91	Jet 1	26.0	0.49	3.12
Jet 2	57.2	1.35	2.74	Jet 2 (SLT)	21.9	0.15	3.83
Jet 3	47.4	1.02	4.87	Jet 3 (SVX)	18.2	−0.67	4.34
$\not{E}_T$	72.0		4.55	$\not{E}_T$	60.2		1.33
SLT				SLT (e−)	4.21	0.32	3.64
Run 45047 event 104393				**Run 45610 event 139604**			
muon (−)	39.4	−0.36	2.03	muon (+)	54.3	−0.18	0.21
Jet 1 (SVX)	43.9	−1.20	2.06	Jet 1 (SVX)	58.9	−0.70	1.42
Jet 2 (SLT)	30.2	0.41	4.45	Jet 2	50.9	−0.90	4.52
Jet 3	22.5	0.91	2.05	Jet 3	27.0	−1.51	4.80
$\not{E}_T$	91.0		5.52	$\not{E}_T$	27.7		2.53
SLT (e+)	22.6	0.42	4.41	SLT			
Run 42548 event 143286				**Run 45705 event 54765**			
electron (+)	65.1	−0.43	1.77	electron (−)	52.6	0.70	1.35
Jet 1 (SLT)	44.2	−0.50	4.21	Jet 1	74.0	0.81	3.73
Jet 2	25.8	−0.67	3.18	Jet 2	36.6	−0.22	3.06
Jet 3	16.7	1.70	5.82	Jet 3 (SLT)	33.9	0.68	4.98
$\not{E}_T$	46.1		6.00	$\not{E}_T$	57.9		0.23
SLT (μ−)	2.24	−0.19	4.30	SLT (e+)	11.1	0.74	4.85
Run 43351 event 266423				**Run 40758 event 44414**			
muon (−)	24.1	−0.07	6.24	electron (+)	109.0	0.44	3.64
Jet 1	99.8	1.18	5.68	Jet 1 (SVX)	74.0	−0.24	0.30
Jet 2	68.8	−0.18	3.07	Jet 2	64.1	0.30	1.91
Jet 3	22.0	0.23	5.56	Jet 3	51.9	0.62	0.80
Jet 4 (SLT)	11.9	0.38	1.67	Jet 4	20.2	1.46	5.65
$\not{E}_T$	68.2		2.39	$\not{E}_T$	56.2		4.69
SLT (μ−)	2.12	0.48	1.86	SLT			
Run 45879 event 123158				**Run 45880 event 31838**			
muon (+)	53.7	−0.21	0.09	electron (−)	27.3	0.16	4.48
Jet 1	69.4	−1.63	2.79	Jet 1	84.2	−0.20	6.21
Jet 2 (SVX,SLT)	62.1	−0.11	5.21	Jet 2	39.6	1.09	4.27
Jet 3	28.8	0.13	0.66	Jet 3 (SLT)	20.8	0.38	1.14
Jet 4	25.9	−0.44	3.26	Jet 4	15.9	−0.59	3.70
$\not{E}_T$	20.8		3.34	$\not{E}_T$	68.3		2.34
SLT (μ−)	13.5	−0.11	5.23	SLT (e−)	2.58	0.41	1.24

tags described here). Figure 42 shows an event display for one of the events with an SVX tag. Shown are the observed calorimeter energy, the CTC charged tracks, and the SVX tracks that show the displaced vertex.

D. Checks using the Z + multijet control sample

In principle, the Z + multijet sample can provide a good cross-check of the heavy-flavor content of the W + multijet events because of the similar W and Z production mechanisms. If there is a standard model source of heavy flavor in association with W bosons (other than $t\bar{t}$) exceeding our background prediction, it could likely produce Z + heavy-flavor events in excess of background predictions. In practice, the combined cross-section times branching ratio for $Z \rightarrow l^+ l^-$ is an order of magnitude lower than $W \rightarrow l\nu$, giving only limited statistics in the Z channel. In addition, studies of systematic effects of the tagging algorithms are best performed using the large control samples described in the previous sections. Nonetheless the study of heavy-flavor production in Z + multijet events presented here serves as a rough check for the SVX and SLT b tagging methods. Note that the gluon-fusion channel, which cannot produce $W + b\bar{b}$ accounts for no more than 40% of the $Z + b\bar{b}$ cross section [48].

The Z selection criteria are designed to collect a pure sample of Z candidates. If the sample has a significant non-Z component, perhaps due to heavy-flavor pairs, the background prediction becomes problematic. For this sample, we select events with oppositely charged ee or $\mu\mu$ pairs with a pair mass between 75 and 105 GeV/c^2. One lepton is required to pass the lepton identification criteria used in the lepton + jets analysis that is described in Secs. III B and III C. In order to improve the statistics of the event sample, the second lepton E_T threshold is lowered to 10 GeV and the selection criteria are loosened. In order to get the best rejection of background, the
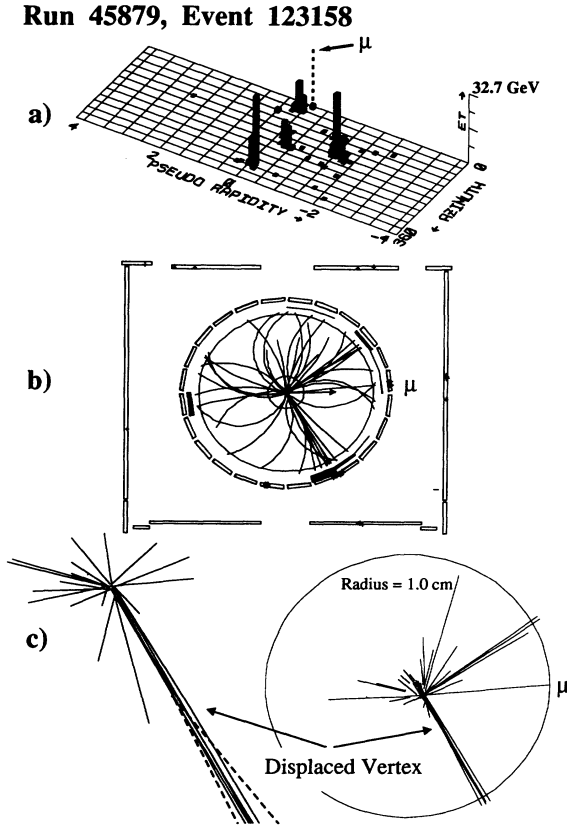
Run 45879, Event 123158

FIG. 42. Event display for one of the SVX tagged W+multijet events; (a) displays the observed calorimeter E_T in the η-ϕ plane, (b) shows muons hits in the CMU (circular detector just outside the tracking chamber) and CMP muon hits (the outside muon detector) as well as the charged tracks found by the CTC. Detail of tracks found by the SVX as well as the complete SVX event display are shown in (c). The dashed tracks form the displaced vertex. Extraneous tracks have been removed from the enlargement. The track lengths in the complete SVX event display are proportional to the track's P_T.

second lepton is required to have $I_{cal}/E_T < 0.1$, where I_{cal} is the calorimeter isolation variable defined in Sec. III. This cut is more than 90% efficient for the Z+multijet events.

Table XXVI lists the yield of Z candidates and the number of tags observed in these events for both the SLT and SVX tagging algorithms. The background predic-

tion, also given in Table XXVI, is calculated in the same way as in Secs. V B 3 and V C 2 for the W sample. No backgrounds from non-Z sources, such as $b\bar{b}$ background or $t\bar{t}$ are included. In the whole sample we observe eight and predict 5.8 events. We also search for tags in the $Z + \geq 3$ jet sample, the equivalent to the top search region in the W sample. This sample consists of three events with three jets and two events with four jets. Two SVX tags (both in events with four jets) and no SLT tags are observed. The predicted background is 0.64 ± 0.055 (0.31 ± 0.05 for SVX tagging only). The probability of observing two or more when expecting 0.64 ± 0.06 (0.31 ± 0.05) is 14% (4%). For completeness, we have also examined Z candidate events, where the second lepton fails the isolation requirement. This is expected to add less than 10% acceptance to the Z sample and allows in a potential background from $b\bar{b}$ production. In the $N_{jet}=1$, 2, and ≥ 3 jet bins we find 19, 3, and 1 more event(s), respectively. In these additional events, we observe one SVX tagged event with two jets (this event was discussed in Sec. IV), and an additional SVX tagged event with three jets. No SLT tags were added. Because of the presence of additional events, the background prediction in the $Z+3$ or more jets sample increases to 0.77 events (0.42 for SVX tagging only). This does not include any added contribution from non-Z sources that contain heavy flavor. Although statistically limited, the excess of tagged $Z+3$ or more jet events could potentially signal a (non-$t\bar{t}$) source of heavy-flavor production in association with a vector boson, which exceeds our background predictions, although higher statistics checks of b tagging in $W+1$ and 2 jet events are consistent with expectations.

E. Summary of tagged lepton + jets search

Two methods of tagging b quarks in $t\bar{t}$ events have been developed and applied to a sample of W candidates with associated jet activity. In 52 $W+3$ or more jet events, we find six tags in six different events using a b-tagging algorithm based on SVX secondary vertex information. We predict a background of 2.3 ± 0.3 tags in the absence of $t\bar{t}$ events. This background prediction comes largely from the data, and is expected to be an overestimate. A second background method, which relies more heavily on Monte Carlo simulation of background processes, gives a lower estimate. Two other tagging algorithms employing SVX information give similar results

TABLE XXVI. Summary of the rate of Z candidates both with and without b tags, and the expected backgrounds.

	$Z+1$ jet	$Z+2$ jet	$Z+ \geq 3$ jets
Observed Z Candidates	176	21	5
SVX tags	0	0	2
SVX background prediction	1.4 ± 0.2	0.32 ± 0.05	0.31 ± 0.05
SLT tags	6	0	0
SLT background prediction	2.9 ± 0.3	0.52 ± 0.05	0.33 ± 0.03
SVX+SLT tags	6	0	2
SVX+SLT background prediction	4.3 ± 0.4	0.84 ± 0.07	0.64 ± 0.06

for the number of observed tags and expected background. The correlations between the three SVX tagging algorithms in data are consistent with what is expected from sources of real heavy flavor. Using a low-momentum or *soft* lepton *b* tag, we observe seven tags in seven of the 52 events. The background in the absence of $t\bar{t}$ events is predicted to be 3.1 ± 0.3 tags. This is also expected to be an overestimate. There are three events tagged by both the SLT and SVX algorithms. Finally, a low statistics check of our background estimation, performed on events with $Z+3$ or more jets, found two tagged events on an expected background of 0.64 ± 0.06.

VI. DISCUSSION OF THE RESULTS OF THE COUNTING EXPERIMENTS

The analyses presented in Secs. IV and V yield an excess of events over expected backgrounds. In Secs. VI A and VI B we estimate the statistical significance of these results. In Sec. VI A we calculate the probability $\mathcal{P}_i$ ($i=$SVX,SLT,dil) that an upward fluctuation of the estimated backgrounds is responsible for the observed excess in each of the analyses individually. In Sec. VI B we combine the three analyses and evaluate the probability $\mathcal{P}_{\text{combined}}$ that the combined observation is a result of an upward fluctuation of the summed background estimates. In Sec. VI B 1 this is done using the total number of candidate events. We note that of the combined total of ten SVX or SLT tagged events, three events are tagged by both, and there is additional significance in these double-tagged events, which is ignored in the simple event-counting of Sec. VI B 1. In order to include the significance of the three double-tagged events in $\mathcal{P}_{\text{combined}}$ we first demonstrate that we understand tagging correlations between SVX and SLT events. This is done in Sec. VI B 2 by studying a large sample of generic jet events. In Sec. VI B 3 we calculate $\mathcal{P}_{\text{combined}}$ by summing the total number of SVX+SLT tags (13), thereby including the significance of the double-tagged events, and the two dilepton candidates to give 15 "counts." This calculation is performed with a Monte Carlo program that includes correlations between SVX and SLT background fluctuations. These correlations result from the large overlap in the sources of background. The calculation also includes the smaller effect of correlations in the SVX and SLT mistag probabilities. This Monte Carlo treatment yields our best estimate of the significance of the combined result. The results from these sections are summarized in Table XXVII. In Sec. VI B 4 we evaluate $\mathcal{P}_{\text{combined}}$ for a

TABLE XXVII. Summary of the results of Secs. VI A and VI B. $\mathcal{P}$ is the probability that the observation is a result of an upward fluctuation of the estimated backgrounds.

Method	$\mathcal{P}$
SVX Individual	0.032
SLT Individual	0.041
dil Individual	0.12
Combined, events	0.016
Combined, counts	0.0026

mixture of $t\bar{t}$ and background, and in Sec. VI B 5 we describe various checks of the combined result.

In Sec. VI C we discuss the results of applying the *b*-tagging algorithms to the dilepton candidate events. One event is found to be tagged by both SVX and SLT. In Sec. VI D we discuss hypotheses other than $t\bar{t}$ production as a source of the excess of tagged events.

A. Statistical significance of the individual results

We find an excess of events over expected backgrounds in each of the analyses. The dilepton search finds two events with an expected background of $0.56^{+0.25}_{-0.13}$ events. The lepton + jets search using the SVX *b* tag has a total of six candidate events with a background expectation of 2.30 ± 0.29 events (method 1) and the lepton + jets search using the SLT finds a total of seven candidates with an expected background of 3.1 ± 0.3 events.

For each of these results we calculate the probability $\mathcal{P}$ that the estimated background has fluctuated up to the number of candidate events seen or greater. This calculation is done using Poisson statistics, where the mean of the distribution is given a Gaussian smearing in order to account for systematic uncertainty on the expected number of background events. We find $\mathcal{P}_{\text{dil}}=12\%$ for the dilepton search, $\mathcal{P}_{\text{SVX}}=3.2\%$ for the SVX search, and $\mathcal{P}_{\text{SLT}}=4.1\%$ for the SLT search.

B. Statistical significance of the combined result

1. Combined result by counting events

The combined yield of the three analyses is 12 events: Two dilepton candidates and ten SVX or SLT tagged lepton+jets events. We sum the three background estimates and subtract an expected mean of 0.26 SVX-SLT overlaps (see Sec. VI B 3) to give a combined total of $5.7^{+0.49}_{-0.44}$ expected background events. Using Poisson statistics convoluted with a Gaussian smearing to account for systematic uncertainties on the mean number of expected background events, we define $\mathcal{P}_{\text{combined}}$ as the probability of observing 12 or more events when $5.7^{+0.49}_{-0.44}$ are expected. We find $\mathcal{P}_{\text{combined}}=1.6\%$. This procedure, however, overestimates $\mathcal{P}_{\text{combined}}$ because three of the ten SVX or SLT candidates events are tagged by both SVX and SLT. A tag in an event tagged by both SVX and SLT is approximately six times more likely to contain heavy flavor than a mistag (see Sec. VI B 3). The effective background for the three double-tagged events is therefore considerably smaller than for the other seven events because they are less likely to be mistags. Provided that we understand potential correlations in the SVX-SLT double-tagging probability, it is appropriate in calculating $\mathcal{P}_{\text{combined}}$ to sum the total number of SVX and SLT tags, counting an event twice if it is tagged by both SVX and SLT. This procedure gives additional weight to the double-tagged events, since the background for these events is significantly smaller than the background for single tagged events.

There are two ways in which correlations can influence $\mathcal{P}_{\text{combined}}$. If the SVX and SLT tagging rates were highly

correlated on some source of background, whether it be real heavy flavor or otherwise, the probability for getting two tags from a single event in this category would be underestimated by the product of the individual probabilities and thus $\mathcal{P}_{\text{combined}}$ underestimated. On the other hand, even for those backgrounds for which the SVX and SLT tagging probabilities are completely *un*correlated, $\mathcal{P}_{\text{combined}}$ must take into account overlaps in the sources of the backgrounds. If the number of events from some common background source, such as $Wb\bar{b}$, fluctuates up from the expected mean before the b-tagging algorithms are applied, then *both* the SVX and SLT backgrounds will fluctuate up as well, despite the fact that the tagging probabilities are uncorrelated. The sources of backgrounds for the dilepton, SVX and SLT analyses are enumerated in Secs. IV C, V B 3, and V C 2, respectively. Our understanding of SVX-SLT double tags is the subject of the next section.

2. SVX-SLT double tags

We have studied tagging correlations between the SVX and SLT by measuring the individual tagging rates and the rate of SVX-SLT double tags in a generic jet sample. This sample, which was described in Sec. V B 3, consists of 67 021 jets (in 31 922 events) with $E_T > 15$ GeV and $|\eta| < 2.0$, selected so that the event vertex is inside the SVX fiducial volume. Table XXVIII shows the observed SVX, SLT, and SVX-SLT tags in this sample. The $-L_{xy}$ SVX tagged sample is not expected to be significantly enriched in heavy flavor relative to generic jets (as the $+L_{xy}$ tags are) and provides a dataset in which we can study mistag correlations between SVX and SLT. Applying the SLT tag-rate parametrization measured from generic jets (Sec. V C 2) to the $-L_{xy}$ tagged events yields the predictions shown in the table. Including a $\sqrt{N}$ uncertainty for the number of observed double tags, the observed-minus-predicted rate differs from zero by $+1.3\sigma$ for double-tagged jets and $+1.0\sigma$ for double-tagged events. We note that an observed-minus-predicted double mistag rate of exactly zero is not an indication that the mistag probabilities of SVX and SLT are uncorrelated, but rather that any correlations that exist are accounted for by the tag-rate parametrization. This can be seen by noting that the double-tag predictions, which result from applying the SLT tag rate parametrization event by event, are approximately a factor of 2 higher than we would predict by multiplying the to-

tal number of jets or events by the product of the *average* SVX and SLT tag rates. This mistag correlation results from the fact that both taggers favor jets containing many tracks. The observed-minus-predicted rates are consistent with zero, and we conclude that mistag correlations are well accounted for by the tag rate parametrizations from generic jets, although it is possible that a small additional correlation exists. We discuss the implications of such an additional correlation in Sec. VI B 5.

The predictions given by applying the tag-rate parametrizations to the $+L_{xy}$ SVX tagged events are labeled "prediction I" in Table XXVIII, and are significantly below the observed number. This is a result of the fact that the $+L_{xy}$ SVX-tagged events are enriched in heavy flavor relative to the generic jet sample. If we assume that the $+L_{xy}$ excess, given by the number of $+L_{xy}$ tags minus the number of $-L_{xy}$ tags, is from heavy flavor, then we predict a number of additional double tags given by the $+L_{xy}$ excess times the SLT tagging efficiency for SVX-tagged heavy-flavor jets or events. This efficiency has been measured with a Monte Carlo program to be $(4.7\pm1.2)\%$ per jet and $(7.5\pm1.5)\%$ per event, yielding an expectation of 26 ± 7 additional double-tagged jets and 39 ± 8 additional double-tagged events. The total number of observed double-tags is expected to be given by the sum of this number and the prediction from the parametrization. The result is labeled "prediction II" in Table XXVIII, and is in good agreement with the observed numbers. We conclude that the correlation in the double mistag rate in the $-L_{xy}$ sample is properly modeled by the tag-rate probabilities and that the *apparent* correlation on the $+L_{xy}$ sample is understood as resulting from the heavy-flavor content of that sample.

Our calculation of the predicted number of $+L_{xy}$ double tags assumes that the probability of finding a SLT tag in a heavy-flavor event tagged by SVX is given simply by the SLT tagging efficiency for that class of events, i.e., there are no SVX-SLT correlations on real heavy-flavor tags. We have tested this assumption on a sample of top Monte Carlo events with $M_{\text{top}} = 150$ GeV/c^2. In this sample we indeed find that the fraction of events with both tags is given by the simple product of individual efficiencies. We assume that this holds for W+heavy flavor as well.

3. Combined result counting SVX+SLT tags

Armed with the understanding of the SVX-SLT tagging correlations described in the preceding section, we

TABLE XXVIII. Observed SVX, SLT, and SVX-SLT tags in generic jets.

	Number of jets	Number of events
Before tagging	67 021	31 922
$+L_{xy}$ SVX tags	818	795
$-L_{xy}$ SVX tags	275	274
SLT tags	1065	1051
$-L_{xy}$ SVX and SLT	14	22
$-L_{xy}$ overlap prediction	9±1	17±2
$+L_{xy}$ SVX and SLT	44	66
$+L_{xy}$ overlap prediction I	20±2	38±4
$+L_{xy}$ overlap prediction II	46±7	77±9

can calculate $\mathcal{P}_{combined}$ based on the total number of observed "counts." There are a total of 13 SVX+SLT tags and two dilepton candidates giving 15 counts with $5.96^{+0.49}_{-0.44}$ expected from background. In Fig. 43 we show the combined total of SVX and SLT tags (counting twice an event tagged by both) and the sum of the SVX and SLT method-1 background estimates. We calculate $\mathcal{P}_{combined}$ for this result using a Monte Carlo program, which includes the inherent coupling of SVX and SLT background fluctuations due to the common W + heavy-flavor background. The Monte Carlo method consists of performing a large number of "background experiments." We begin by calculating the parent populations of $Wb\bar{b}$, $Wc\bar{c}$, Wc, and W+jets without heavy flavor, in the sample of 52 events with a lepton and three or more jets. This is done using the Monte Carlo estimates of these backgrounds as described in Sec. V B 3, and scaling up to a total equivalent to the SVX method-1 background estimate. In each experiment, these parent populations are used as mean values and the actual number for that experiment is drawn from a Poisson distribution. The total number of W + 3 or more jet events for each experiment is constrained to be 52. For the W + heavy-flavor events, the efficiencies of each of the tagging algorithms are applied to determine how many of these events are tagged and double tagged. The possibility of mistagging real heavy-flavor is included. For the W+jets events that do not contain heavy flavor, the mistag probabilities are applied to determine the number of tagged and double-tagged events in this category. As discussed above, applying the mistag parametrizations to generic jet events results in a predicted double SVX-SLT mistag rate approximately a factor of 2 larger than the product of the individual *average* mistag probabilities. This mistag correlation is included in the Monte Carlo calcula-
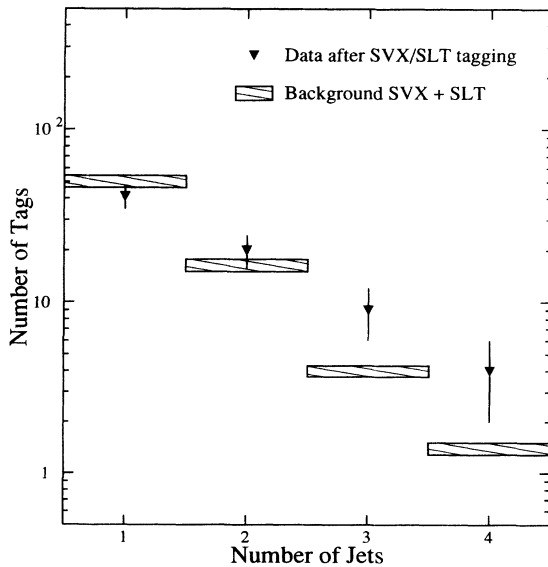

FIG. 43. The sum of SVX and SLT tags observed in the W+jets data (solid triangles). Events tagged by both algorithms are counted twice. The shaded area is the sum of the method-1 background estimates for SVX and SL, with its error.

tion. Finally, the remaining background contributions listed in Tables XXI and XXIV, $b\bar{b}$, $Z \to \tau\tau$, and dibosons, are included by sampling a Poisson distribution. Uncertainties on parent populations and tagging probabilities are incorporated into the Monte Carlo program by smearing the Poisson means with Gaussian distributions.

The dilepton backgrounds are treated independently, and a Poisson-distributed number of events for each background experiment is added to the number of SLT+SVX tags to give the total number of counts for that experiment. $\mathcal{P}_{combined}$ is the fraction of experiments with 15 or more total counts.

Using the W + heavy-flavor content consistent with the method-1 background estimates in Table XXI, we find $\mathcal{P}_{combined} = 2.6 \times 10^{-3}$. This is to be compared with 1.6×10^{-3}, which results from the simple calculation of the probability for observing 15 or more when $5.96^{+0.49}_{-0.44}$ are expected, a calculation which assumes that SVX and SLT are completely uncorrelated and have no overlap. Although we continue to rely on the more conservative method 1 background estimates, it is interesting to compare with the result obtained using a W + heavy-flavor content consistent with the method-2 backgrounds of Table XXI. In this case $\mathcal{P}_{combined} = 2.6 \times 10^{-4}$, an order of magnitude smaller than the method-1 result. The method-2 equivalent background for the SLT resulting from this exercise is 2.4 events. We note that for a Gaussian probability function, which we do not have here, $\mathcal{P}_{combined} = 2.6 \times 10^{-3}$ or 2.6×10^{-4} would correspond to a 2.8σ or 3.5σ excess, respectively.

The Monte Carlo technique also allows us to calculate the mean number of double tags from the background. We find that the average number of SVX-SLT double tags for all background experiments is 0.26 (0.23 from W + heavy-flavor and 0.035 from mistags). The average number of SVX-SLT double tags for that subset of experiments with ≥ 13 SVX+SLT tags is 1.3. The observed number of three SVX-SLT double tag is more than we expect from background, even under the assumption that the entire observation is due to a background fluctuation.

4. Consistency with a mixture of $t\bar{t}$ and background

Using the same Monte Carlo technique as in Sec. VI B 3, we can estimate $\mathcal{P}_{combined}$ under the hypothesis that the data contain a mixture of $t\bar{t}$ and background. We evaluate $\mathcal{P}_{combined}$ as a function of M_{top}, where the mean number of $t\bar{t}$ events in the parent population for a given mass is given by the theoretical cross section from Ref. [10] times the integrated luminosity. For each Monte Carlo experiment this mean is smeared by a Gaussian of width 30%, corresponding to the theoretical uncertainty in the calculation, and then the number of $t\bar{t}$ events is drawn from a Poisson distribution. From this parent population, the number of lepton + jets events and the number of dilepton events are drawn according to the acceptances of each analysis. The efficiencies of the SVX and SLT algorithms are applied to the lepton + jets events to determine the number of $t\bar{t}$ tags. Mistags of $t\bar{t}$ events are allowed. Tagging of the background component of

TABLE XXIX. Expected and observed SVX-SLT double tags. Expectations are calculated with $\sigma_{t\bar{t}}=13.9$ pb (see Sec. VII).

No. of Jets	Double tags, no top	Double tags, with top	Double tags, data
1	0.54	0.64	0
2	0.63	0.88	3
≥ 3	0.26	1.0	3

the data proceeds exactly as in the background-only Monte Carlo described above. In the case of an admixture of $t\bar{t}$, the parent populations of W+heavy-flavor events are rescaled to account for the fraction of $t\bar{t}$ events in the 52 W+3 or more jet events. We find $\mathcal{P}_{\text{combined}}$ for 15 or more counts in a mixture of $t\bar{t}$ plus background to be 60% for $M_{\text{top}}=140$ GeV/c^2 ($\sigma_{t\bar{t}}=16.9$ pb), 20% for $M_{\text{top}}=160$ GeV/c^2 ($\sigma_{t\bar{t}}=8.2$ pb), and 4.5% for $M_{\text{top}}=180$ GeV/c^2 ($\sigma_{t\bar{t}}=4.2$ pb). We conclude that the data are consistent with the $t\bar{t}$+background hypothesis.

The number of double tags expected in the W+3 or more jets sample, under the assumption that it contains both top (with $\sigma_{t\bar{t}}=13.9$ pb, see Sec. VII) and the expected background mixture, is compared with the number observed in Table XXIX. The average number of double tags expected for our W+3 or more jet sample is 1.0. This is less than we observe and similar to the expectation under the assumption of an upward fluctuation of the background. As mentioned above, the three double tags are unlikely to come from a source other than heavy flavor. However, because the predicted number of double tags is similar if we interpret our data as top+background or if we interpret it as all background, there is no additional discrimination between $t\bar{t}$ and background provided by the double tags, beyond that already provided by the excess of total counts. In the W+1 and 2 jet samples there are three observed double tags with an expectation of 1.5, again a slight excess. We note, however, that one of the double-tagged W+2 jet events is a dilepton candidate event (see Sec. VI C). Under the assumption that this is a real top event, at least part of the excess in the two jet bin is due to an upward fluctuation of the expected top signal.

5. Checks of the combined result

We can test the sensitivity of the result of Sec. VI B 3 to possible further correlations in the double-tagging rate that have not been accounted for in our simulation. We do this by including additional correlations in the Monte Carlo program and comparing the result to the nominal case above, where the double-tag probability for heavy flavor is the product of the individual probabilities and the double-mistag probability is twice the product of the individual mistag probabilities. Taking the double mistag probability to be four times the product and the double heavy-flavor tag probability to be two times the product of the individual probabilities changes $\mathcal{P}_{\text{combined}}$ from 2.6×10^{-3} to 3.7×10^{-3}. With these correlations, one would predict approximately 36 double-tagged events in the $-L_{xy}$ tagged generic jet sample, where only 22 are

observed. Similarly the prediction in the $+L_{xy}$ tagged sample would be approximated 100 double-tagged events, where only 66 are observed.

Because the three observed SVX-SLT double tags are more than the 1.0 expected on average (see Table XXIX), we have checked if the observation is consistent with the expectation for the events actually in hand, under the assumption that they are a mixture of $t\bar{t}$ and background. To do this we have asked if the observed number of SVX tags in the seven SLT tagged events is consistent with what we expect for those events. The SVX tagging efficiency in $t\bar{t}$ events is strongly dependent on the features of the event such as track multiplicity and the total number of SVX-fiducial jets. We use the ISAJET $t\bar{t}$ Monte Carlo programs to parametrize the SVX tagging efficiency as a function of a single variable and then test the dependence on the choice of this variable by trying three different choices: the number of good SVX tracks in the event, the maximum number of good SVX tracks in a jet, and the total number of taggable jets. Interpreting all seven SLT tagged events as $t\bar{t}$, leads to a double-tag prediction of 1.9–2.1 events, depending on which parametrization is chosen. However, the seven SLT events contain some background. As discussed in Sec. VII, under the assumption that the 52 events contain a $t\bar{t}$ component, the background estimate must be rescaled, yielding an SLT background of 1.5 ± 0.7 events. Including all uncertainties and randomizing the choice of which events are background and which are $t\bar{t}$, we estimate the number of double-tagged events expected to be 1.8 ± 1.3, where the uncertainty includes both statistical and systematic uncertainties. The probability for observing three or more double-tagged events is 30%. We conclude that the three observed double-tagged events are consistent with expectations for these events under the assumption that they contain a mix of $t\bar{t}$ and background.

Our model of background fluctuations assumes that the systematic uncertainty on the expected mean number of events is described by a Gaussian distribution. The data can be used to test if this assumption covers possible large deviations of the $Wb\bar{b}$ background from our expectations. We use as the test sample SVX and SLT tagged events containing a W or Z plus one or two jets. This gives the best statistics in a sample, which should contain heavy-flavor jets and yet have very little top contamination. There are 67 tags in this sample. The combined SVX and SLT background estimate (method 1) is 72.4, of which 22.7 is due to W or Z plus a heavy quark pair. There is good agreement between the prediction and the observation. To see how large the heavy-flavor background could reasonably be, we use the data as an estima-

TABLE XXX. Expected background, expected signal, and observed tags when different jet E_T thresholds are used to select events.

Jet threshold	Background	160-GeV/c^2 top	Observed counts
Nominal	6.0	6.2	15
Nominal +5 GeV	3.6	5.2	11
Nominal −5 GeV	12.7	7.1	19

tor. We find that the background is less than 80.4 at the 95% confidence level. That value is eight tags larger than the background estimate of 72.4. If we ascribe this excess entirely to anomalous $W/Z + b\bar{b}$ production, this source would be about 35% larger than our estimate of 22.7. Applying that fractional increase to the signal region ($W + 3$ or more jets) increases the total SVX background from 2.3 to 2.7 and the total SLT background from 3.1 to 3.3. The former is a 1.5σ increase in the mean SVX background, while the latter is less than a 1σ increase in the mean SLT background. Such an excess of $Wb\bar{b}$ production is fully covered by the Gaussian fluctuations in the mean background that are included in the Monte Carlo program described above.

As an example of the sensitivity of our result to changes in the event selection criteria, we have varied the minimum E_T requirement for jets. Table XXX shows the expected background, expected signal for a 160-GeV/c^2 top mass, and the number of observed counts for the nominal jet thresholds, described in Secs. IV A and V A, as well as 5 GeV above and below nominal. For the dilepton analysis, 5 GeV below nominal would be a 5-GeV jet threshold. In this case, the dilepton jet requirement was removed completely, since the systematic uncertainty in the 5-GeV jet detection efficiency is large. Within the statistics of the measurement, the data behave as expected when the jet E_T threshold is varied.

C. Tags in the dilepton sample

We have applied the b-tagging algorithms to the two $e\mu$ candidates. The first $e\mu$ event contains a jet (jet 1 in event I of Table VII), which is tagged by both the SVX and SLT algorithms. There are no b tags in the second $e\mu$ event (event II of Table VI). In addition, as mentioned in Sec. V C, there is a $W + 3$ jet candidate tagged by both SLT and SVX, which passes all the dilepton selection requirements, except that the electron candidate fails two of the electron identification requirements (E_{had}/E_{EM} and strip χ^2). Although such cases are properly accounted for in the acceptance calculations, in many ways this event is more consistent with being a tagged dilepton event than it is a double-tagged lepton+jets event. The expected number of b-tagged top dilepton events is given in Table XXXI. If, as in Sec. VI B 5, we ask what is the expected number of SVX tags for *these* two events, under the assumption that they are both $t\bar{t}$, we find an expectation of 0.7 events, compared to the average value of 0.24 events for $M_{top} = 160$ GeV/c^2, which is listed in Table XXXI. Similarly the expected number of double-tags for these events is 0.13 compared

to the average value of 0.05 events.

Jets in nontop (i.e., background) dilepton events arise from the hadronization of gluons or light quarks. Events from $b\bar{b}$ production constitute one source of dilepton background; however, in these events the two b quarks decay semileptonically, and the additional jets will not be b jets. The tag in these events is required to be away from the leading leptons, so we can obtain an estimate of the expected number of falsely b-tagged dilepton events by applying the SVX and SLT tag-rate parametrizations described in Secs. V B 3 and V C 2 to the jets in the two $e\mu$ events. For the double-tag prediction from background, we multiply the prediction from the tag-rate parametrizations by two to take into account the enhanced heavy-flavor content of SVX-tagged events, consistent with the difference between prediction I and prediction II in Table XXVIII. The results of this calculation are also given in Table XXXI in the row labeled "background." Note that this estimate assumes that the two observed dilepton events are both background. An *ab initio* calculation of the number of double-tagged background events, beginning from the 0.56 event dilepton background before tagging, results in an estimate, which is more than an order of magnitude smaller than that shown in Table XXXI. It is difficult to draw quantitative conclusions based on a single event, but a dilepton candidate event with both a SVX tag and a SLT tag is more likely to be due to $t\bar{t}$ than background. The existence of a tagged dilepton event, together with the observed excess of tagged W+multijet events from the SVX and SLT analyses, provides evidence for an excess of both $Wb\bar{b}$ and $WWb\bar{b}$ production, as expected from $t\bar{t}$ decays. Because the b tagging is an *a posteriori* check of the dilepton data and not an *a priori* requirement, we do not include these tags in the calculation of $\mathcal{P}_{combined}$ described in Sec. VI B 3.

D. Alternate hypotheses

Under the assumption that the excess of candidate events is not due to an upward fluctuation of the known backgrounds, the data finds a natural interpretation in terms of standard model $t\bar{t}$ production and decay. However, our data cannot exclude more exotic phenomena, which could provide alternate explanations. We, therefore, briefly survey here some possible alternate hypotheses, though the list is by no means exhaustive.

We begin by considering the possibility that a heavy quark other than the top quark is being detected. The simplest example would be a fourth generation quark with weak isospin $-1/2$ (b'). The production cross section for such an object is the same as for a top quark of the same mass. We will, therefore, assume that the b' is lighter than the top. In this case the b' could either decay to Wc, or via a loop-induced flavor changing neutral current process [49] to $V + b$ (V=gluon, photon, or Z). The relative branching ratio of the different decay modes depends on the value of the Cabibbo-Kobayashi-Maskawa (CKM) matrix element describing the coupling of the fourth generation to the second one. If the charged current decay were favored, our excess of events would indicate a production cross section at least a factor

of 3 larger than what we evaluate under the top hypothesis. This is because both the SVX and SLT tagging efficiencies for charm hadrons are significantly smaller than for bottom hadrons. The mass estimate derived in Sec. IX, however, would not change. This result would therefore not be consistent with the expected production cross section. If the neutral current decays were favored, no signals would be manifest in the channels we considered. It is perhaps interesting, though, that this possibility is not inconsistent with the slight excess of tags in the Z + multijet sample discussed in Sec. V D.

The excess of b tags in our sample suggests that we consider other phenomena rich in b quarks. One such example would be the production of a standard model Higgs boson with a mass less than about 150 GeV/c^2, a region where the branching ratio to $b\bar{b}$ is of order 1. Associated production of $W + H$ pairs would provide signatures qualitatively similar to those observed. In the mass region $M_{\text{Higgs}} = 60$–80 GeV/c^2, the expected production cross section is of order 1 pb [50]. However, inclusion of semileptonic branching ratios, detection efficiencies, and acceptances will reduce the observable rate by approximately two orders of magnitude, leaving us with only a fraction of an event expected. Nevertheless, this would become an interesting alternative if production mechanisms other than what is currently assumed were active. These might also increase the expected rate of $Z + H$ production. Future higher statistics studies, which will allow reconstruction of the $b\bar{b}$ invariant mass by tagging of both the b and $\bar{b}$ jets will allow us to test this possibility.

Even under the assumption that we are observing $t\bar{t}$ production, our current statistics are too limited to test the production and decay mechanisms in any detail. One may consider, for example, nonstandard model production channels in addition to QCD, such as new resonances strongly coupled to top [51,52]. This model could be probed with future increases in statistics by looking for a peak in the invariant mass distribution of the $t\bar{t}$ pair. The presence of additional decay modes of the top quark, such as the decay to a charged Higgs boson [53], might be indirectly probed by comparing the rate of single lepton to dilepton final states. Again, at the current time the statistics are too poor to either exclude or support this possibility.

VII. $t\bar{t}$ PRODUCTION CROSS SECTION

A. Likelihood technique and results

Using the observed number of candidate events and the acceptances tabulated in Secs. IV and V we calculate the

TABLE XXXI. Numbers of dilepton events expected with single and double b tags from $t\bar{t}$ and background sources.

	SVX	SLT	SVX-SLT
Signal, $M_{\text{top}} = 140$ GeV/c^2	0.44	0.37	0.09
Signal, $M_{\text{top}} = 160$ GeV/c^2	0.24	0.20	0.05
Background	0.08	0.10	0.014
Data	1	1	1

cross section for $t\bar{t}$ production in $\bar{p}p$ collisions at $\sqrt{s} = 1.8$ TeV. In Tables XXXII and XXXIII we summarize the acceptances, theoretical cross sections, and number of events expected as a function of M_{top}.

The cross sections are calculated by maximizing the following likelihood function:

$$L = \exp\left[-\frac{\left[\int \mathcal{L}\, dt - \overline{\int \mathcal{L}\, dt}\right]^2}{2\sigma_{\mathcal{L}}^2} \right] L_{\text{dil}} L_{\text{SVX}} L_{\text{SLT}}$$

where each of the individual likelihoods is of the form

$$L_i = G(\epsilon_i, \bar{\epsilon}_i, \sigma_{\epsilon_i}) G(b_i, \bar{b}_i, \sigma_{b_i})$$

$$\times P\left[\left\{ \epsilon_i \sigma_{t\bar{t}} \int \mathcal{L}\, dt + b_i \right\}, n_i \right] .$$

Here $G(x, \bar{x}, \sigma)$ is a Gaussian in x, with mean $\bar{x}$ and variance σ^2, and $P(\mu, n)$ is a Poisson probability for n with mean μ. In each of these likelihoods, $\bar{\epsilon}_i$ and σ_{ϵ_i} are the total acceptance and its uncertainty, $\bar{b}_i$ and σ_{b_i} are the expected background and its uncertainty, n_i is the number of observed candidate events, $\sigma_{t\bar{t}}$ is the $t\bar{t}$ production cross section, and $\int \mathcal{L}\, dt = 19.3$ pb^{-1} is the integrated luminosity, with $\sigma_{\mathcal{L}}$ its 3.6% uncertainty. For the SVX and SLT terms, the total acceptance is split into two parts, the acceptance for the lepton plus jets selection, described in Sec. V, and the tagging efficiencies, described in Secs. V B and V C. The uncertainty on the common lepton plus jets acceptance is treated as 100% correlated between the two analyses.

To calculate the cross section from an individual analysis, the individual likelihood functions are used, in which case the maximum likelihood solution for $\sigma_{t\bar{t}}$ is just

$$\sigma_{t\bar{t}} = \frac{n - \bar{b}}{\bar{\epsilon} \int \mathcal{L}\, dt} .$$

TABLE XXXII. Summary of top acceptance and the theoretical production cross section of Ref. [10].

M_{top}	120 GeV/c^2	140 GeV/c^2	160 GeV/c^2	180 GeV/c^2
$\sigma_{t\bar{t}}$ (pb)	$38.9^{+10.8}_{-5.2}$	$16.9^{+3.6}_{-1.8}$	$8.2^{+1.4}_{-0.8}$	$4.2^{+0.6}_{-0.4}$
ϵ_{SVX}	1.0 ± 0.3 %	1.5 ± 0.4 %	1.7 ± 0.5 %	1.8 ± 0.6 %
ϵ_{SLT}	0.84 ± 0.17 %	1.1 ± 0.2 %	1.2 ± 0.2 %	1.3 ± 0.2 %
ϵ_{dil}	0.49 ± 0.07 %	0.66 ± 0.06 %	0.78 ± 0.07 %	0.86 ± 0.07 %

TABLE XXXIII. Numbers of $t\bar{t}$ events expected, assuming the theoretical production cross sections shown in Table XXXII, and the numbers of candidate events observed with expected backgrounds.

Channel	SVX	SLT	Dilepton
Expected No. events $M_{top} = 120$ GeV/c^2	7.7±2.5	6.3±1.3	3.7±0.6
Expected No. events $M_{top} = 140$ GeV/c^2	4.8±1.7	3.5±0.7	2.2±0.2
Expected No. events $M_{top} = 160$ GeV/c^2	2.7±0.9	1.9±0.3	1.3±0.1
Expected No. events $M_{top} = 180$ GeV/c^2	1.4±0.4	1.1±0.2	0.68±0.06
Expected background	2.3±0.3	3.1±0.3	$0.56^{+0.25}_{-0.13}$
Observed events	6	7	2

The uncertainties on the measured cross-section values are calculated as the $\Delta \ln L = \frac{1}{2}$ points of the likelihood function.

Before maximizing the likelihood function to find $\sigma_{t\bar{t}}$, we make two corrections, one to the SVX and SLT tagging efficiencies and a second to the SVX and SLT background estimates. A correction of the tagging efficiencies is required because Monte Carlo does not correctly model the processes, which lead to mistags of real $t\bar{t}$ events, and therefore the SVX and SLT acceptances in Table XXXII are underestimates of the true acceptance. We correct the tagging efficiencies by

$$\epsilon^{cor}_{tag} = \epsilon_{tag} + (1 - \epsilon_{tag})P_{mistag}$$

where P_{mistag} is the probability of mistagging a top event. We estimate $P_{mistag} = (1.5 \pm 0.8)\%$ for the SVX from the $-L_{xy}$ tag rate in the $W + 3$ or more jet sample, and $P_{mistag} = (3.3 \pm 0.9)\%$ for the SLT from the fakes $+ Wb\bar{b} + Wc\bar{c}$ background in Table XXIV, after subtracting the expected heavy-flavor content.

The second correction is a result of the way the SVX and SLT backgrounds are calculated. As discussed in Secs. V B and V C, the method-1 SVX and SLT backgrounds for mistags, $Wb\bar{b}$, and $Wc\bar{c}$ are calculated by assuming that the entire parent sample of 52 events contains no top. Parametrizations of tagging probabilities are applied event by event to get the total background. If the 52 events contain a $t\bar{t}$ component, this procedure would overestimate the background. We correct the backgrounds, iteratively, using the SVX and SLT tagging efficiencies. This procedure has potentially large systematic uncertainties associated with it because the backgrounds vary by large factors from event to event, and we do not know which events are top. To estimate this uncertainty we calculate the number of top events expected in the 52 event sample, $N_{t\bar{t}}$, based on the corrected mean background and the tagging efficiencies. We find $N_{t\bar{t}} = 19.6 \pm 9.5$ events from the SVX result and $N_{t\bar{t}} = 29.0 \pm 11.5$ from the SLT result. Random samples of $52 - N_{t\bar{t}}$ events are chosen from the $W + 3$ or more jet events, and the backgrounds from the generic jet parametrizations for these events are summed. The width of the distribution of summed backgrounds is used as the systematic uncertainty on the procedure. We estimate 1.6 ± 0.7 and 1.5 ± 0.7 events for the SVX and SLT backgrounds, respectively (cf. the original backgrounds of 2.3

and 3.1 events). The corrected backgrounds and tagging efficiencies used in the cross-section calculation are shown in Table XXXIV.

The calculated cross sections from the individual SVX, SLT, and dilepton results, as well as the combined result (labeled $\sigma^{all}_{t\bar{t}}$) are shown in Table XXXV. In Fig. 44 we plot the calculated combined cross section as a function of mass, and the theoretical expectation from Ref. [10]. Because the acceptance depends on M_{top}, four points are shown corresponding to measured values of the acceptance. Had we chosen to use the method-2 background estimate for SVX, and an equivalent estimate for SLT, the $t\bar{t}$ cross-section measurement would have shifted upward by 11%. We also note that an alternate method of calculating the cross section, based on the total number of observed events, gives a result approximately 12% lower with comparable uncertainties.

B. W + jet rates

Assuming that the excess of events seen in the analyses presented in Secs. IV and V is due to $t\bar{t}$ production, we have computed the top cross section. In Table XVI we compared the number of W + jets events in the data with expectations from the VECBOS W + jets Monte Carlo program. We can now subtract from the data the estimated number of top events as a function of jet multiplicity in the $W + 1$, 2, 3, and 4 jets samples and repeat the comparison.

As we will show in Sec. IX, if the excess of events over background obtained from the analyses discussed in Secs. IV and V is interpreted as due to $t\bar{t}$ production, then $M_{top} = 174 \pm 16$ GeV/c^2, and $\sigma_{t\bar{t}} = 13.9^{+6.1}_{-4.8}$ pb. In estimating the number of top events, we will use the cross

TABLE XXXIV. Corrected tagging efficiencies and backgrounds used in the cross-section calculation.

	SVX	SLT
$\epsilon^{cor}(M_{top} = 120$ GeV/c^2)	0.21±0.05	0.193±0.027
$\epsilon^{cor}(M_{top} = 140$ GeV/c^2)	0.23±0.06	0.187±0.026
$\epsilon^{cor}(M_{top} = 160$ GeV/c^2)	0.23±0.06	0.180±0.025
$\epsilon^{cor}(M_{top} = 180$ GeV/c^2)	0.23±0.06	0.187±0.026
Corrected background	1.6±0.7	1.5±0.7

TABLE XXXV. $t\bar{t}$ production cross sections calculated from the individual analyses and from the combination of the three analyses.

M_{top}	120 GeV/c^2	140 GeV/c^2	160 GeV/c^2	180 GeV/c^2
$\sigma_{t\bar{t}}^{\text{SVX}}$ (pb)	$21.5^{+17.2}_{-11.3}$	$14.9^{+12.2}_{-7.9}$	$13.0^{+10.6}_{-6.9}$	$12.4^{+10.0}_{-6.5}$
$\sigma_{t\bar{t}}^{\text{SLT}}$ (pb)	$28.9^{+18.5}_{-13.3}$	$22.7^{+14.3}_{-10.4}$	$20.4^{+12.7}_{-9.3}$	$18.8^{+11.7}_{-8.6}$
$\sigma_{t\bar{t}}^{\text{dil}}$ (pb)	$15.2^{+19.5}_{-12.2}$	$11.3^{+14.2}_{-9.0}$	$9.6^{+12.0}_{-7.6}$	$8.8^{+11.0}_{-7.0}$
$\sigma_{t\bar{t}}^{\text{all}}$ (pb)	$22.7^{+10.0}_{-7.9}$	$16.8^{+7.4}_{-5.9}$	$14.7^{+6.5}_{-5.1}$	$13.7^{+6.0}_{-4.7}$

section and acceptances calculated using this top mass.

In Table XXXVI we list, as a function of jet multiplicity, the number of events seen in the data, the number of estimated top events, and the number of background non-W events in the sample (see Sec. V A). The number of QCD W+jets events can then be obtained by subtracting from the data the number of top and background events. This is also shown in Table XXXVI.

In the one- and two-jet samples, the estimated number of top events is negligible compared to the number of QCD W+jets events. The estimated number of top events with ≥ 3 jets is obtained by multiplying the top cross section by the top acceptance (A_{top}), which is given as a function of top mass in Table XVII. For $M_{\text{top}} = 174 \pm 16$ GeV/c^2, $A_{\text{top}} = 0.080 \pm 0.003$, where the uncertainty is due to the top mass only (the other uncertainties are already included in the cross-section uncertainty). The fraction, F_4, of top events with ≥ 3 jets, which have at least four jets is shown in Fig. 45 as a function of top mass, for different Monte Carlo assumptions. F_4 is strongly dependent on M_{top}, and on the modeling of initial-state gluon radiation. In Table XXXVI, we have taken $F_4 = 0.54$ from the HERWIG calculation (for
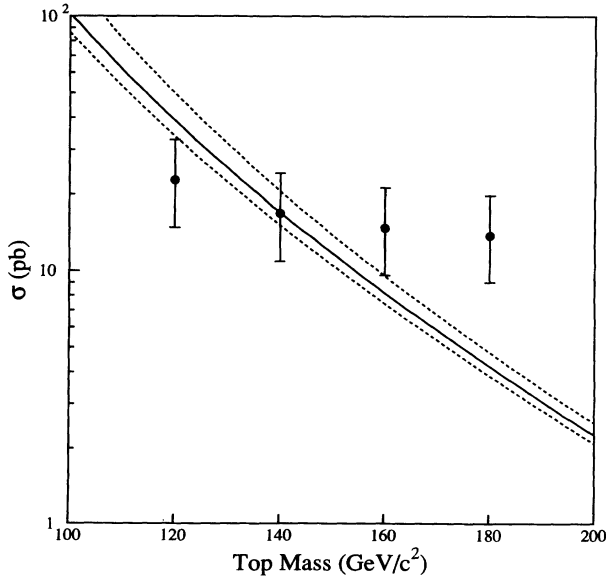
$M_{\text{top}} = 174$ GeV/c^2). The uncertainty on F_4 has three components: (1) an M_{top} dependence, (2) an uncertainty due to the 10% energy scale uncertainty, and (3) an uncertainty due to the modeling of gluon radiation. The first two uncertainties are ± 0.05 and ± 0.03, respectively; we estimate the uncertainty due to gluon radiation to be ± 0.05, which is the difference between the values of F_4 obtained using the HERWIG and ISAJET models.

In Table XXXVII we compare the number of QCD W+jet events from Table XXXVI with expectations from the VECBOS Monte Carlo program (see Sec. V A, and Table XVI). The calculation in VECBOS is a leading-order QCD calculation, and there are large uncertainties in its predicted rates. The VECBOS predictions in Table XXXVII are obtained using a Q^2 scale choice of $Q^2 = \langle P_T \rangle^2$. An equally reasonable choice of $Q^2 = M_W^2$ would have led to significantly lower predictions (see Sec. V A and Ref. [35]). After accounting for the background and top contributions, the $W+1$, 2, and 3 jet rates are in reasonable agreement with the VECBOS predictions. There seems to be a deficit of $W+4$ jet events, since the expected top contribution saturates the number of $W+4$ jet events that we observe. Given the uncertainties on the VECBOS prediction, it is hard to quantify the significance of this deficit.

We can also compare W+jets data with Z+jets data. Since W+jets and Z+jets are very similar processes, most theoretical uncertainties in the cross-section predictions cancel when taking the ratio of the number of $W+N$ jets to the number of $Z+N$ jets. The VECBOS Monte Carlo program predicts that the ratio of $W+N$
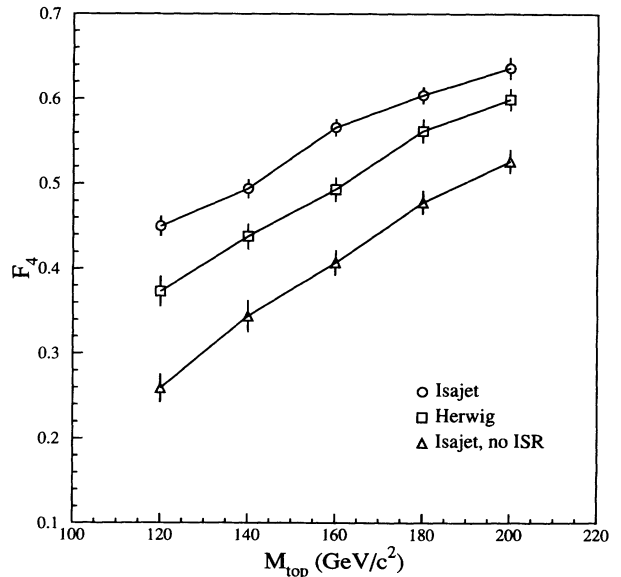

FIG. 44. Combined $t\bar{t}$ production cross section vs M_{top} from data (points) and theory [10]. The dashed lines are estimates of the theoretical uncertainty quoted in Ref. [10].

FIG. 45. Fraction (F_4) of top events with ≥ 3 jets, which have at least four jets as a function of top mass for three Monte Carlo calculations: (1) ISAJET and detector simulation (2) HERWIG, and detector simulation (3) ISAJET without initial-state gluon radiation (ISR) and detector simulation. The error bars are from Monte Carlo statistics.

TABLE XXXVI. Number of events in the data, number of expected top events, assuming the top cross-section measurement from Sec. VII A, and number of background events. The number of QCD W+jets events is obtained by subtracting from the data the top and non-W background contributions. For W+4 or more jets, this subtraction yields the unphysical value $-4.5^{+5.4}_{-6.4}$. The value $0^{+3.5}_{-0.0}$ given in the table is obtained by imposing the constraint that the number of QCD W+4 or more jets should be ≥ 0.

Jet multiplicity	Data	Top	Other backgrounds	QCD W+jets
1 jet	1713	$1.1^{+0.5}_{-0.4}$	284 ± 89	1428 ± 98
2 jets	281	$5.0^{+2.3}_{-1.7}$	54 ± 15	222 ± 23
3 jets	43	$10.0^{+4.8}_{-3.9}$	8.9 ± 2.5	$24.1^{+8.0}_{-8.5}$
≥ 3 jets	52	$21.6^{+9.8}_{-7.6}$	10.8 ± 3.1	$19.6^{+10.9}_{-12.6}$
≥ 4 jets	9	$11.6^{+5.6}_{-4.5}$	1.9 ± 0.6	$0^{+3.5}_{-0.0}$

jets to $Z+N$ jets cross sections is constant to better than 10% for $1 \leq N < 4$ (unfortunately no $Z+4$ jet calculation is available). The ratio of W and Z acceptances, as a function of jet multiplicity, is also constant to better than 5%.

The number of Z+jets events, as a function of jet multiplicity, is given in Table XXVI. Unfortunately, the statistics of the Z sample are limited. There are three $Z+3$ jet events, and two $Z+4$ (or more) jet events in our data. Given that the QCD boson+jets cross section as a function of jet multiplicity is expected to fall by a factor of ≈ 4–8 for each additional jet, it is likely that we are seeing a statistical fluctuation in the $Z+3$ and 4 jet samples, or that there is a source of $Z+4$ jets events in addition to standard QCD production.

The number of W and Z+jet events, and their ratio (R_{WZ}) as a function of jet multiplicity, is given in Table XXXVIII. For the 1 and 2 jet samples, the ratio is consistent with being constant, and the weighted average is $R_{WZ}=8.4\pm0.4$. The ratio for the ≥ 3 jets sample is low by 1.7 standard deviations. The number of W+4 jet events is much lower than the prediction from the number of $Z+4$ jet events. However, as mentioned above, it is likely that the two $Z+4$ jets events observed in our data constitute an upward statistical fluctuation. We have attempted to quantify the apparent discrepancy between the W and Z+4 jet rates. From (1) the expected rate of top events, (2) the non-W background prediction, (3) the assumption that $R_{WZ}=8.4\pm0.4$, independent of

N, and (4) estimating $\sigma(Z+4$ jets) from the two data events under the assumption that $\sigma(Z+3$ jets)$\geq 4\sigma(Z+4$ jets), we compute the probability to find less than or equal to the observed nine W+4 jets candidates in our data to be 2.7%. For a Gaussian probability distribution, a probability of 2.7% would correspond to 2.0σ.

If the deficit of W+3 or more jets, and especially W+4 or more jets, is not a statistical fluctuation, then possible sources for the discrepancy are as follows: (a) Our measured $t\bar{t}$ cross section is too large. This could happen if the excess events described in Sec. VI were not due to top quark production. It could also happen if our assumed tagging efficiency for top events is too small. The tagging efficiencies are calculated from Monte Carlo data and are used in this paper only to calculate the $t\bar{t}$ cross section. They do not enter into the significance calculation presented in Sec. VI. (b) The ratio F_4, also obtained from Monte Carlo data, is too large. This number is used nowhere else in this paper. (c) The two $Z+4$ jet events are either a large statistical fluctuation or are produced by a process other than QCD vector boson+jet production. In this regard we note, as mentioned in Sec. V D, that both of these events have a jet which is b tagged.

VIII. KINEMATICS OF THE 52 $W+ \geq 3$ JETS EVENTS

The search for $t\bar{t}$ production and decay in the lepton+jets mode described in Sec. V yields 52 events with W candidates plus three or more jets, of which 10 events are tagged by at least one b-tagging algorithm (SVX, SLT, or both). If the excess of tagged events discussed in Sec. VI is due to top-quark production, then we

TABLE XXXVII. Comparison of QCD W+jet yields from Table XXXVI with expectations from the VECBOS Monte Carlo program. The first uncertainty on the VECBOS prediction is due to Monte Carlo statistics, the second to the jet energy scale and lepton identification efficiency uncertainties, and the third to the uncertainty on the luminosity normalization. The additional uncertainty related to the choice of the Q^2 scale in the VECBOS Monte Carlo program is discussed in the text. The VECBOS predictions include the $W \to \tau\nu$ contribution.

Jet multiplicity	QCD W+jets	VECBOS ($Q^2=\langle P_T\rangle^2$)
1 jet	1428 ± 98	$1571\pm82^{+267}_{-204}\pm55$
2 jets	222 ± 23	$267\pm20^{+77}_{-53}\pm9$
3 jets	$24.1^{+8.0}_{-8.5}$	$39\pm3^{+11}_{-9}\pm2$
≥ 4 jets	$0^{+3.5}_{-0.0}$	$7\pm1^{+3}_{-2}\pm0.2$

TABLE XXXVIII. W+jets and Z+jets event rates from Tables XXXVI and XXVI as a function of jet multiplicity. R_{WZ} is the ratio of the number of W and Z events.

Jet multiplicity	W+jets	Z+jets	R_{wz}
1 jet	1428 ± 98	176	8.1 ± 0.9
2 jets	222 ± 23	21	10.6 ± 2.6
3 jets	$24.1^{+8.0}_{-8.5}$	3	$8.0^{+4.3}_{-4.7}$
≥ 3 jets	$19.6^{+10.9}_{-12.6}$	5	$3.9^{+2.4}_{-2.6}$
≥ 4 jets	$0^{+3.5}_{-0.0}$	2	$0^{+1.5}_{-0.0}$

would expect roughly one half (19.6±9.5 events estimated from the number of SVX tags and 29.0±11.5 events estimated from the number of SLT tags) of the 52 $W+3$ or more jet events to be from $t\bar{t}$ production. We expect a further 12±3 events from sources that are not QCD $W+\geq3$ jet production (see Table XV). The remaining events are expected to arise from QCD production of $W+3$ or more jets.

In this section we present distributions of some simple kinematic quantities for the 10 tagged and 42 untagged $W+3$ ore more jet events. Jets from top-quark decay are expected to have transverse energies characteristic of the parent top-quark mass. Therefore, if the top quark is sufficiently massive, the distribution of jet transverse energies in $t\bar{t}$ events is expected to be harder than the corresponding distribution predicted for QCD $W+3$ or more jet background events. We therefore compare observed distributions of jet transverse energies with predictions for $t\bar{t}$ production and decay, and predictions for the background arising from QCD production of $W+3$ or more jets.

To improve the kinematic reconstruction of our $W+3$ or more jet events, we have corrected the measured jet energies to take account of instrumental effects. The jet energy corrections are described in Sec. III D. In Sec. VIII A we give relevant details of the VECBOS Monte Carlo program used to simulate the QCD $W+$jet background, and discuss the reliability of the VECBOS Monte Carlo predictions. In Sec. VIII B distributions of kinematic quantities are compared with expectations for signal and background.

A. VECBOS $W+$jets predictions

We have used the VECBOS Monte Carlo program [26] to predict the properties of background events arising from QCD production of $W+3$ or more jets. The VECBOS program generates Monte Carlo events in which the incoming partons have interacted to produce a W boson plus a definite number of additional partons in the final state. VECBOS uses the leading-order QCD matrix
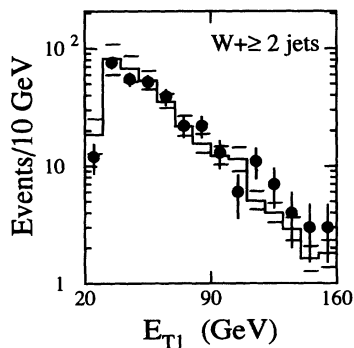
elements, which are calculated for up to four additional final-state partons [30]. Infrared and collinear singularities are regulated by requiring that the additional final-state partons have a transverse momentum exceeding a cutoff value $P_T^{\min}$, and that the final-state partons are separated in (η,ϕ) space by more than $R_{\min}$ $[R=\sqrt{(\Delta\phi)^2+(\Delta\eta)^2}]$. In our calculation we have chosen a $P_T^{\min}$ of 8 GeV/c and an $R_{\min}$ of 0.4. Our VECBOS predictions are made using the Martin-Roberts-Stirling set D0 (MRSD0) structure functions [54] with a Q^2 equal to the square of the average P_T of the outgoing partons. After evolution and hadronization of the initial- and final-state partons, the response of the CDF detector to the resulting final-state particles has been simulated, and jets have been reconstructed using the CDF jet algorithm. This enables the sample of VECBOS Monte Carlo events to be subjected to the same cuts applied to the data. In this section, all VECBOS distributions are normalized to have the same area as the data.

To test whether VECBOS correctly describes QCD $W+$multijet production, we begin by comparing predicted and observed distributions for a sample of $W+2$ or more jet events. Note that the contribution to the $W+2$ or more jet data sample from $t\bar{t}$ production is expected to be small (5% for $M_{\mathrm{top}}=160$ GeV/c^2). In the following, E_{T_n} is defined as the transverse energy of the nth-highest E_T jet in the event. VECBOS is seen to give a reasonable description of the measured E_{T1} distribution (Fig. 46), and the measured E_{T2} distribution (Fig. 47). VECBOS also gives a fair description of the jet pseudorapidity distribution (Fig. 48).

We next compare VECBOS predictions with observed distributions for a sample of events with $Z+2$ or more jets and $Z+3$ or more jets. Only five Z events pass our selection with three or more jets with uncorrected $E_T>15$ GeV. Therefore, to improve the statistics of the $Z+3$ or more jet data sample, we define the jet multiplicity in our Z events by counting jets with $|\eta|<2.4$ and corrected $E_T>15$ GeV. Note that, on average, the jet

FIG. 46. Distribution of transverse energies for the highest E_T jets in $W+2$ or more jet events. Data (points) are compared with VECBOS predictions (histogram) normalized to the data. The short horizontal error bars show the statistical uncertainty on the VECBOS predictions. There are eight data events with highest jet $E_T>160$ GeV.
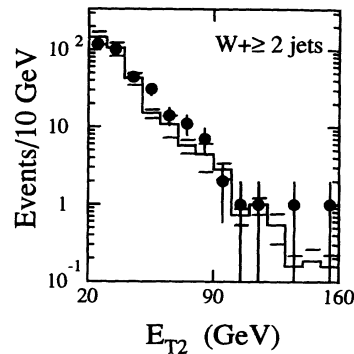

FIG. 47. Distribution of transverse energies for the next-to-highest E_T jets in $W+2$ or more jet events. Data (points) are compared with VECBOS predictions (histogram) normalized to the data. The short horizontal bars show the statistical uncertainty on the VECBOS predictions. There is one data event with next-to-highest jet $E_T>160$ GeV.
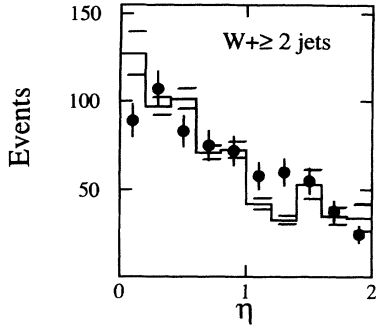
FIG. 48. Distribution of pseudorapidities of the highest and next-to-highest E_T jets in $W+2$ or more jet events. Data (points) are compared with VECBOS predictions (histogram) normalized to the data.

FIG. 50. E_{T2} for Z events having ≥ 2 jets with corrected $E_T > 15$ GeV (points) compared with the VECBOS prediction (histogram) normalized to the data.

energy corrections increase jet energies, and, therefore, by requiring corrected $E_T > 15$ GeV rather than uncorrected $E_T > 15$ GeV, we have in effect relaxed the uncorrected jet E_T threshold by about 5 GeV. There are then 112 $Z+2$ or more jet events and 22 $Z+3$ or more jet events. The distributions of E_{T1} and E_{T2} for the $Z+2$ or more jet sample are shown in Figs. 49 and 50, respectively. These distributions appear to be consistent with the VECBOS predictions. However, there is one event with $E_{T2} > 100$ GeV, where VECBOS predicts a fraction of an event. This event may be due to either a statistical fluctuation or may indicate a contribution from processes other than QCD $Z+3$ or more jet production.

Finally, of relevance to our discussion of the $W+3$ or more jet kinematic distributions will be the quantity $(E_{T2}+E_{T3})$ and the distribution of events in the (E_{T2},E_{T3}) plane. In Fig. 51 VECBOS is shown to give a reasonable description of the measured $(E_{T2}+E_{T3})$ distribution for the sample of $Z+3$ or more jet events. Note that the five Z events with three or more jets with uncorrected $E_T > 15$ GeV, discussed in Sec. V D, are the five events with the largest values of $(E_{T2}+E_{T3})$ in Fig. 51. The distribution of $Z+3$ or more jet events in the (E_{T2},E_{T3}) plane is shown in Fig. 52. Our VECBOS $Z+3$ or more jet calculation for Z events with three or more
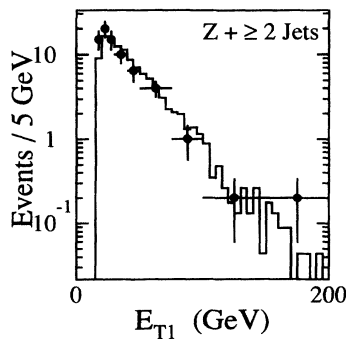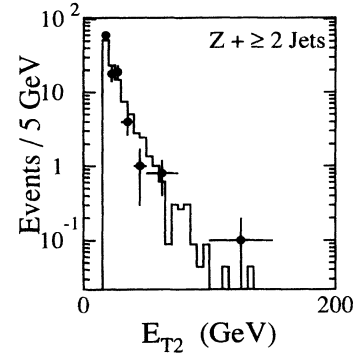
jets with corrected $E_T > 15$ GeV predicts that 50% of the events should have $(E_{T2}+E_{T3}) < 48$ GeV. Of the 22 $Z+3$ or more jet events we observe 13 events with $(E_{T2}+E_{T3}) < 48$ GeV.

We conclude that the VECBOS Monte Carlo predictions give a reasonable description of the jet transverse energy distributions arising from QCD $W+2$ or more jet production, $Z+2$ or more jet production, and $Z+3$ or more jet production.

B. Kinematic distributions of the 52 $W + \geq 3$ jet events

To choose simple kinematic variables that discriminate well between $t\bar{t}$ events and the QCD $W+$jets background, we have made a Monte Carlo study in which HERWIG $t\bar{t}$ predictions have been compared with VECBOS predictions for a large number of potentially interesting variables. One variable, which we find gives good discrimination between signal and background, is the quantity $E_{T2}+E_{T3}$. Measured and predicted $W+3$ or more jet event densities in the (E_{T2},E_{T3}) plane are shown in Fig. 53. The VECBOS prediction for the $W+3$ or more jets QCD background [Fig. 53(a)] is peaked at low values of E_{T2} and E_{T3}. The broken line in Fig. 53(a), which shows the function $E_{T2}+E_{T3}=71$ GeV, divides the plane
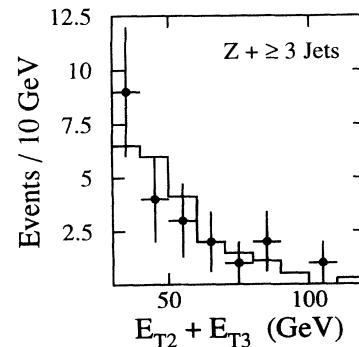

FIG. 49. E_{T1} for Z events having ≥ 2 jets with corrected $E_T > 15$ GeV (points) compared with the VECBOS prediction (histogram) normalized to the data.

FIG. 51. $E_{T2}+E_{T3}$ for Z events having ≥ 3 jets with corrected $E_T > 15$ GeV (points) compared with the VECBOS prediction (histogram) normalized to the data.
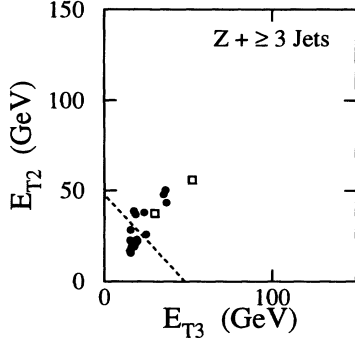
FIG. 52. Distribution of E_{T2} vs E_{T3} shown for the 22 Z events with ≥ 3 jets having corrected $E_T > 15$ GeV. The broken line shows the function $E_{T2}+E_{T3}=48$ GeV. The two events shown as boxes have a b tag.

into two regions such that 50% of the VECBOS events lie below the line. The HERWIG $t\bar{t}$ Monte Carlo calculation predicts broader distributions of E_{T2} and E_{T3} [Figs. 53(b) for $M_{top}=140$ GeV/c^2 and 53(c) for $M_{top}=160$ GeV/c^2]. Furthermore, the predicted E_{T2} and E_{T3} distributions get broader with increasing top-quark mass. With a top-quark mass of 140 GeV/c^2 (160 GeV/c^2) only $17\pm1\%$ ($7\pm1\%$) of the $t\bar{t}$ Monte Carlo events have $E_{T2}+E_{T3}<71$ GeV. Figure 53(d) shows the distribution of our 52 $W+3$ or more jet events in the (E_{T2},E_{T3}) plane. The observed distribution appears to be broader than the VECBOS prediction. There are 13 events with
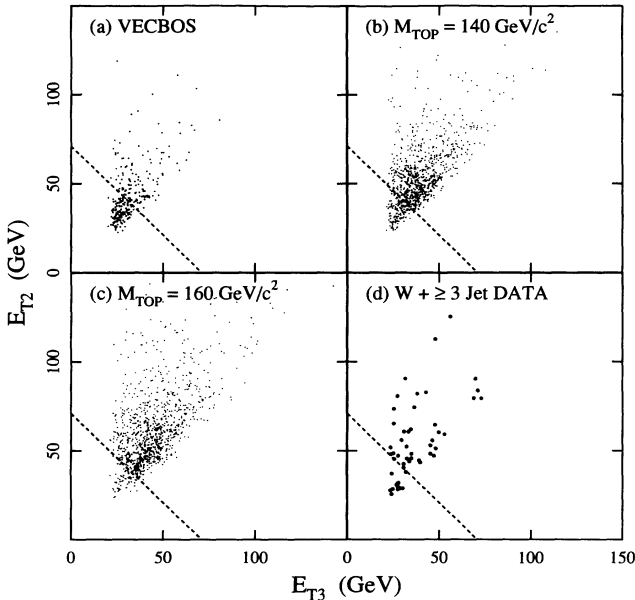
$E_{T2}+E_{T3}<71$ GeV. If we assume that these 13 events all arise from QCD $W+3$ or more jet production, then we observe an excess of 26 ± 7 events with $E_{T2}+E_{T3}>71$ GeV that are not predicted by VECBOS. This excess of events at large $E_{T2}+E_{T3}$ is also seen in Fig. 54, which compares the shape of the $(E_{T2}+E_{T3})$ distribution for the 52 $W+3$ or more jet events with VECBOS predictions.

To interpret the excess of events with large $(E_{T2}+E_{T3})$, we first consider the contribution to the event sample from background processes other than QCD $W+3$ or more jet production, which we will refer to in the following as non-W backgrounds. The non-W backgrounds are described in Sec. V of this paper. The estimated contributions from some of the non-W background processes scale with the number of QCD $W+3$ or more jet events in the sample. In the absence of a contribution from $t\bar{t}$ production (the null hypothesis) we estimate that there are 12.2 ± 3.1 non-W background events in our $W+3$ or more jet sample (see Table XV). If, on the other hand, 50% of the 52 events arise from $t\bar{t}$ production, then we estimate that there are 10.6 ± 3.0 non-W background events in our $W+3$ or more jet sample. If we relax the requirement on the second lepton in the Z removal algorithm, and we relax the requirements on the opposite-sign partner track in the conversion removal algorithm, two of the 52 events are identified as leptonic Z decay candidates, and the electrons in three of the 52 events are identified as photon conversion candidates. These observations are consistent with our expectations

FIG. 53. Distribution of E_{T2} vs E_{T3} shown for (a) VECBOS QCD $W+\geq 3$ jet prediction, (b) $t\bar{t}$ production with a top mass of 140 GeV/c^2, (c) $t\bar{t}$ production with a top mass of 160 GeV/c^2, and (d) the 52 $W+\geq 3$ jet events. The normalizations of the Monte Carlo samples are arbitrary. The broken lines show the function $E_{T2}+E_{T3}=71$ GeV, chosen because 50% of the VECBOS events have $E_{T2}+E_{T3}>71$ GeV.
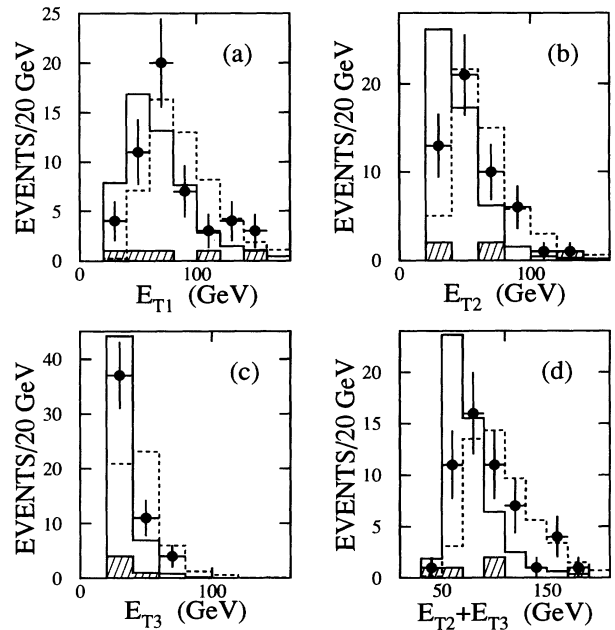

FIG. 54. Jet transverse energy distributions for the 52 $W+3$ or more jet events (points) compared with VECBOS QCD $W+3$ or more jet predictions (histogram) and HERWIG $t\bar{t}$ predictions for $M_{top}=160$ GeV/c^2 (broken histogram). The Monte Carlo predictions are normalized to the data. The hatched subhistograms show the location of the five events discussed in the text, which are identified as non-W backgrounds.
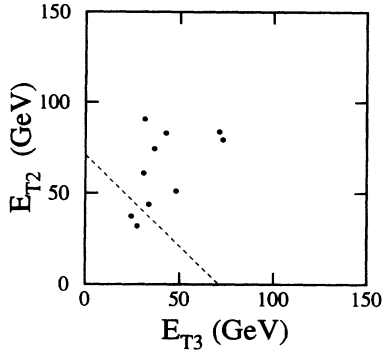
FIG. 55. Distribution of E_{T2} vs E_{T3} shown for the ten tagged $W + \geq 3$ jet events. The broken line shows the function $E_{T2} + E_{T3} = 74$ GeV, chosen such that 50% of the VECBOS events have $E_{T2} + E_{T3} > 74$ GeV. Not that the line $E_{T2} + E_{T3} > 74$ GeV is slightly different than the corresponding line in Fig. 53. The difference takes into account the bias towards more central higher-E_T jets resulting from the b tagging.

for non-W backgrounds. Two of the identified non-W background events have $E_{T2} + E_{T3} < 71$ GeV [Fig. 54(d)]. After subtracting the identified non-W background events, we are left with an excess of 25 ± 7 events with $E_{T2} + E_{T3} > 71$ GeV. To subtract the remaining unidentified non-W background events we assume the worse case, namely, that these events are all in the region $E_{T2} + E_{T3} > 71$ GeV and that the total non-W background is 12.2 ± 3.1 events. Thus, after subtracting the non-W backgrounds, we conclude that there is an excess of 17.8 ± 7.5 events with $E_{T2} + E_{T3} > 71$ GeV. Provided the
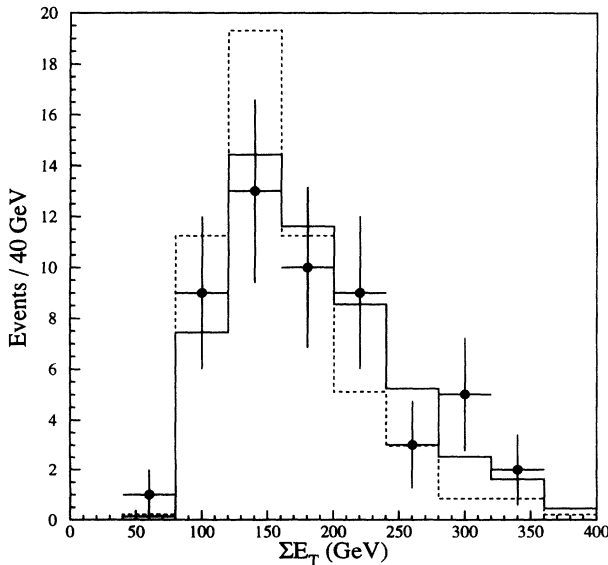

FIG. 56. Total transverse energy distribution for the 52 $W + \geq 3$ jet events (points) compared with the Monte Carlo prediction for a mixture of 50% $t\bar{t}$ production ($M_{top} = 160$ GeV/c^2) plus 50% QCD $W + \geq 3$ jet production (solid line histogram), and the prediction for 100% QCD $W + \geq 3$ jet production (broken-line histogram). The predictions are normalized to the data.

top quark is massive, this excess is consistent with a sizable contribution to our $W + 3$ or more jet sample arising from $t\bar{t}$ production.

If the excess of events at large $(E_{T2} + E_{T3})$ is due to $t\bar{t}$ production then we would expect the 10 $W + 3$ or more jet events containing a b tag to also have larger values of $(E_{T2} + E_{T3})$. This is indeed the case (see Fig. 55).

In Fig. 54, measured jet transverse energy distributions for the 52 $W + 3$ or more jet events are compared with VECBOS predictions and with HERWIG $t\bar{t}$ predictions. In Fig. 56 VECBOS and HERWIG predictions are compared with the measured distribution of total transverse energies $\sum E_T$, where the sum is over all jets with corrected $E_T > 15$ GeV. The measured distributions of E_{T1}, E_{T2}, E_{T3}, $E_{T2} + E_{T3}$, and $\sum E_T$, which are shown in Figs. 54 and 56, all tend to be harder than the VECBOS predictions. Thus, the observed jet transverse energy distributions for the 52 $W + 3$ or more jet events are qualitatively consistent with a sizable contribution from $t\bar{t}$ production with a massive top quark. However, systematic uncertainties on the measured and predicted distributions are substantial. Work is currently in progress to significantly reduce the systematic uncertainties on the kinematic analysis of $W + 3$ or more jet events and to optimize the selection [55] of the event sample to reduce the contribution from non-W backgrounds. Results will be described in a future paper. In the present analysis we have reduced the systematic uncertainties by making a kinematic fit to each event in which constraints are imposed on the candidate t and $\bar{t}$ decay products ($M_{top} = M_{\overline{top}}$) and on the candidate W decay products (mass $= M_W$). These constraints reduce the systematic uncertainties due to the jet energy scale and on the kinematics of events arising from background processes. The results from this fitting procedure are described in Sec. IX.

IX. DIRECT DETERMINATION OF THE TOP MASS

Given the hypothesis that the excess of b-tagged events, described in the preceding sections, is due to $t\bar{t}$ production, we can estimate the top mass directly from these events using a constrained-fitting technique. In order to determine a value of M_{top} event by event, we require each event to have four jets. This allows a one-to-one matching of the jets to the quarks in the process

$$t\bar{t} \rightarrow l\nu_l b_1 + q\bar{q}' b_2 \ .$$

To increase the acceptance for the $t\bar{t}$ events in the b-tagged $W + 3$ or more jet sample described in Sec. V, the selection criteria for the fourth jet are relaxed to uncorrected $E_T > 8$ GeV, $|\eta| < 2.4$. Monte Carlo studies made using the HERWIG generator indicate that for a top quark of mass 170 GeV/c^2, 60% of the events having at least three jets also have a fourth jet passing the standard criteria, while 86% have a fourth jet passing the relaxed criteria. This gain in acceptance is deemed necessary given the small statistics of the sample. The same Monte Carlo studies show that with the relaxed criteria, the fraction of events where the fourth jet is a jet from gluon radiation increases from 21 to 25%. This point will be addressed in Sec. IX B when we discuss the effects of

gluon jets. Of the ten b-tagged events, seven pass these selection criteria. We estimate the background for the seven events passing the four-jet selection to be $1.4^{+2.0}_{-1.1}$. We obtain this estimate with a Monte Carlo program, which computes the probability of tagging seven events out of the sample of 27, which pass the four-jet selection, as a function of the number of $t\bar{t}$ events in the sample. This technique produces a probability distribution for the number of tagged events coming from background. We used this probability distribution to determine the most probable value for the background and its uncertainty. This is significantly smaller than the $t\bar{t}$ background reported in Sec. VII primarily due to the smaller event sample satisfying the fourth jet requirement.

A. Fitting method

The method that we have adopted to fit the events to the $t\bar{t}$ process is straightforward. We use the measured energy and angle of each of the four jets to infer the 4-momenta of the primary partons. The known detector response and measurement uncertainties are taken into account, as discussed in more detail below. We have used a kinematic fitting program [56] to reconstruct the entire event. To describe the process

$$\bar{p}p \rightarrow t\bar{t} + X$$

the following subprocesses are kinematically constrained:

Vertex	Process
1	$\bar{p}p \rightarrow t_1 + t_2 + X$
2	$t_1 \rightarrow b_1 + W_1$
3	$t_2 \rightarrow b_2 + W_2$
4	$W_1 \rightarrow l + v$
5	$W_2 \rightarrow j_1 + j_2$

In this five-vertex system we have assumed that the initial $\bar{p}p$ system has a net momentum of zero and an energy of 1.8 TeV. We further assume that t_1 and t_2 have the same mass. As described at the end of Sec. IX A, we obtain measurements of l, b_1, b_2, j_1, and j_2 from the reconstructed leptons and jets passing our selection criteria. The quantity X represents the system recoiling against the $t\bar{t}$ pair. Information on X comes from the measured vector transverse energy E_T^{total} ($E_T^{\text{total}} = -\boldsymbol{E}_T$), with its invariant mass and the third component of its momentum left as unknowns. We measure the x and y components of the momentum of X by subtracting from E_T^{total} the four jets that we use in the fit, b_1, b_2, j_1, and j_2, and the energy measured in the calorimeter for the electron or muon in the event. All measured quantities are corrected for detector response. Unclustered calorimeter energy is scaled by 1.6 to correct on average for detector non-linearities, reduced calorimeter response at boundaries between modules, and detector-dependent energy thresholds (see Sec. III E). The v momentum is left as an unknown in the fit, and it is determined from the kinematical constraints. However, because we do not measure the longitudinal component of the total energy, there are two possible solutions for the P_Z of the neutrino. This leads

to two solutions for M_{top} that quite often are very close in mass. The one corresponding to the best fit (lowest fit χ^2) is chosen. The W boson mass is required to be $M_W = 80.2$ GeV/c^2, with an uncertainty assigned to the W mass in the fit consistent with the W width of 2.1 GeV/c^2 [57]. The overall kinematic fit is over constrained (20 equations and 18 unknowns), thus allowing a mass measurement.

To reduce the combinatoric possibilities, only the four highest-E_T jets are used in forming invariant masses. The fit is made for all jet configurations, subject to the constraint that the tagged jet in the event must be one of the b quarks. In this case the number of possible combinations of the four jets is six, which gives 12 configurations when we add the two neutrino solutions for P_Z. If there were no jet tagged as a b, the number of configurations would be 24. Of course, the best case would be when two jets in the same event are tagged because only four combinations would be allowed. The best overall kinematic fit is chosen, and the W-b invariant mass obtained for this configuration gives the top mass for the event. The seven events with four jets pass a loose χ^2 requirement ($\chi^2 < 10$) on the best fit, and we use them to estimate M_{top}.

We have checked the results with other procedures used to perform kinematic fits. One method consists of minimizing the χ^2 formed by the constraints described above and allowing the momenta to vary, leaving the angles fixed. Other methods are based on calculating, for each event, the likelihood for points in the parameter space allowed by the errors on the measured quantities and then choosing the more likely solution [58]. All of these methods give top mass values, which agree within a few GeV/c^2. The results reported here come from the complete kinematic fitting of the events as described above.

To define the momentum vector for electrons, we use the energy measured in the CEM and the direction from the reconstructed electron track. For muons, the momentum vector is defined by the reconstructed track constrained to originate from the primary vertex. Uncertainties on the measured quantities are assigned according to the detector resolutions, as summarized in Sec. II.

In order to infer the quark momenta from the measured jet energies, it is necessary to make use of jet energy corrections. The correction functions discussed in Sec. III D were developed for QCD jet studies. In the determination of the top mass, we make use of an improved set of corrections, which are more appropriate for top events. These new corrections account for the energy sharing between different jets in top events, and for the presence in each event of b jets, which require corrections specific for semileptonic decays.

The improved set of correction functions has been generated by comparing the jet E_T with the parton P_T in top Monte Carlo events using the HERWIG generator. In this study the jet E_T is already corrected for detector effects, as explained in Sec. III D. The corrections are modeled for four types of jets: (1) jets generated by the light quarks from the W decay, (2) generic b jets, of interest for SVX b tags, (3) b jets containing a decay $b \rightarrow evX$, and (4)
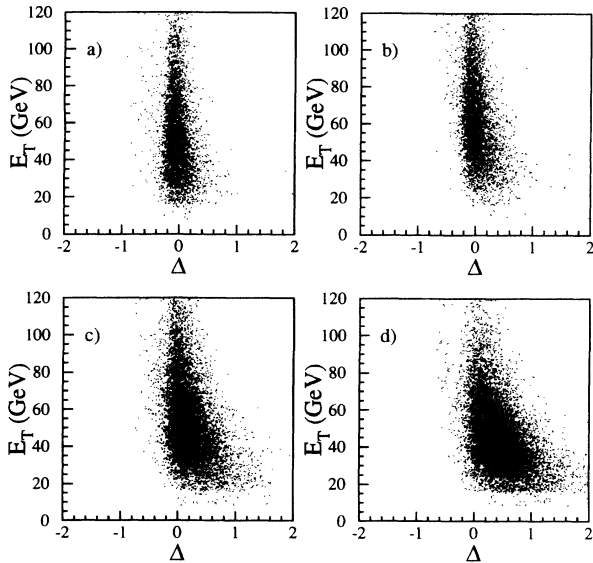
FIG. 57. Scatter plots of jet E_T corrected with standard jet corrections vs Δ for the four jet types: (a) light quarks, (b) generic b jets, (c) $b \to evX$ jets, and (d) $b \to \mu vX$: $\Delta = [P_T(\text{parton}) - E_T(\text{jet})]/E_T(\text{jet})$. The Monte Carlo events have been generated with HERWIG at $M_{\text{top}} = 170$ GeV/c^2.

b jets containing a decay $b \to \mu vX$, both of interest for SLT b tags. Figure 57 shows the E_T of the jet vs $\Delta(E_T)$ for the four jet templates, where $\Delta(E_T) = [P_T(\text{parton}) - E_T(\text{jet})]/E_T(\text{jet})$. Each scatter plot has been finely sliced in E_T. The projections of the slices on the $\Delta(E_T)$ axis give the average value for jet corrections and the energy resolution as a function of jet E_T. All jets in this
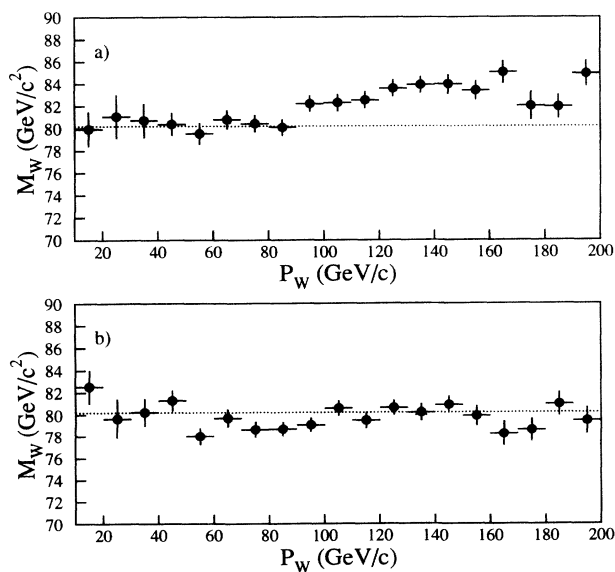
analysis have been corrected according to this prescription.

One effect of the physics model used to generate the corrections can be seen in Fig. 58, which shows the invariant mass of the two jets from the W decay as a function of the W momentum. The study is done using top Monte Carlo events generated at $M_{\text{top}} = 170$ GeV/c^2 and both sets of jet corrections. The average value of the W mass is improved, and the fact that the overlap between the two jets increases with the momentum of the W is correctly taken into account.

The improvement due to the correction for semileptonic b decays is illustrated in Fig. 59. The invariant mass of the three jets coming from a 170-GeV/c^2 top decay is shown for the cases where the b jet contains a $b \to \mu vX$ decay. Using $b \to \mu$ specific jet corrections, the fitted mean of the distribution is within 1 GeV/c^2 of the expected value.

To allow the study of the systematic uncertainties on the fitted mass due to the modeling of the jet corrections, separate sets of correction functions have been obtained using different Monte Carlo generators, HERWIG (Sec. III F and [25]) and ISAJET [23], and different values for the top mass (see Sec. IX C 3).

B. Test of the method on Monte Carlo events

Application of the corrections and fitting method described above to top Monte Carlo events ($M_{\text{top}} = 170$ GeV/c^2), generated with HERWIG and processed through the CDF detector simulation program, gives the reconstructed top mass spectrum shown in Fig. 60. This distri-
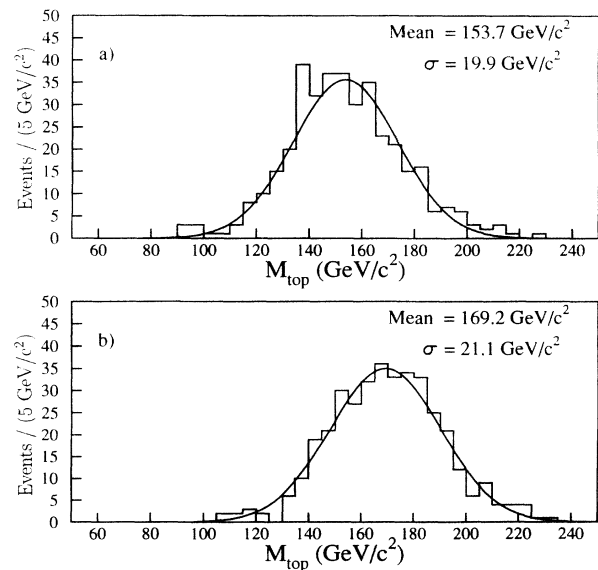

FIG. 58. Mass of the W calculated using the four-momenta of the jets as a function of the W momentum. The jet momenta are corrected with standard jet corrections (top plot) and with the jet corrections used in the mass analysis (bottom plot). The events plotted are generated with HERWIG at $M_{\text{top}} = 170$ GeV/c^2.

FIG. 59. Invariant mass of the b jet and the two jets from the W decay when the b jet contains a semileptonic decay to muon and neutrino. The jet momenta are corrected with standard jet corrections (top plot) and with the jet corrections used in the mass analysis (bottom plot). The events plotted are generated with HERWIG at $M_{\text{top}} = 170$ GeV/c^2.
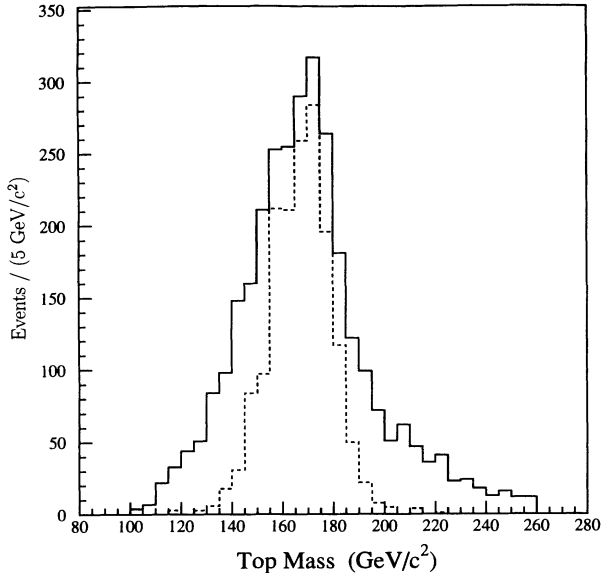
FIG. 60. Reconstructed top mass distribution for Monte Carlo events generated with $M_{\text{top}} = 170$ GeV/c^2. The full histogram corresponds to the best fit obtained by the fitting program when requiring that one of the b jets is a b in the fit. The dashed histogram refers to the fit with the correct assignment for each of the jets.

FIG. 61. Reconstructed mass distribution for W+multijet Monte Carlo events.

bution comes from the best fit obtained when we require the tagged jet to be a b in the fit. The peak is centered at 168 GeV/c^2 and has a σ of 23 GeV/c^2. For comparison the distribution obtained with the correct parton assignments is shown as a dashed histogram. This distribution has $\sigma = 12$ GeV/c^2. The fitting method leads to the correct assignments of the four jets only 31% of the time. The long tail and the widening of the mass distribution are due to two effects: (a) 22% of the events have the correct jets, but the wrong jet assignment is chosen, and (b) 47% of the events have a mismatch between a jet and its corresponding parton direction by $\Delta R > 0.5$. This mismatch can be due to gluon radiation altering the direction of the parton from the top decay, or to assigning an emitted gluon as one of the quark jets. About one half of these jets are among the three with the highest E_T. Detailed studies of these events show the distributions of fitted M_{top} to be wider and sometimes asymmetric, but the peak value of the reconstructed mass is not significantly altered. Similar results are obtained for other choices of M_{top}. Note that the distribution of Fig. 60 is cut at 260 GeV/c^2. Since this experiment is not expected to have sensitivity to very high top masses, we have arbitrarily rejected any solution with $M > 260$ GeV/c^2 and chosen the next best solution. This cut affects 1.6% (4.8%) of the events for $M_{\text{top}} = 170$ (210) GeV/c^2. In these cases, the next best solution is found to have the same mass distribution as the events for which the best solution was below 260 GeV/c^2. One out of the seven b-tagged events has a solution at $M = 285$ GeV/c^2. For this event the second best solution with $M = 166$ GeV/c^2 is chosen.

Studies of W+multijet events generated with the

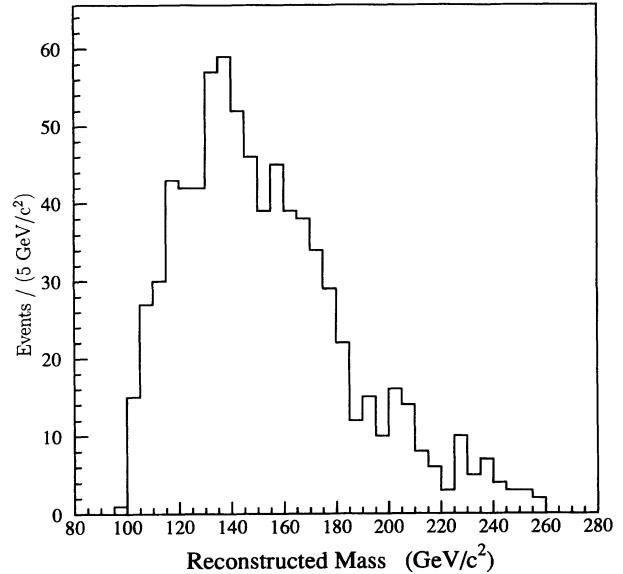VECBOS Monte Carlo program indicate that 83% of the events that pass our selection criteria yield solutions with good χ^2, presumably because of the rather large number of combinations of jet assignments. For comparison, for $M_{\text{top}} = 170$ GeV/c^2 we find that 94% of the events have a fit with $\chi^2 < 10$. Thus it is not possible to discriminate between signal and background on the basis of the χ^2 of a fit to the $t\bar{t}$ hypothesis. Fitting W+multijet events to the $t\bar{t}$ hypothesis yields a mass distribution with a very broad peak centered at about 140 GeV/c^2, as shown in Fig. 61. The events were generated using VECBOS, in conjunction with the HERWIG Monte Carlo generator for parton shower evolution and hadronization, and a CDF detector simulation program.

C. Results from fitting the data

We have applied the fitting technique discussed above to estimate a mass from each of the tagged events. The results are presented in Table XXXIX. We require the fitting program to assign the tagged jet as a b jet. For five of the events the fitter naturally finds this assignment as the minimum χ^2 solution, while for the other two it is the second best solution. Notice also that the signs of the leptons from top and the sequential decays in three out of four SLT tags agree with the hypotheses that the second lepton comes from b decays, whereas in the fourth event the second lepton is consistent with coming from a c decay. This is consistent with the calculation of Sec. V (2.3 and 1.7 events for the two hypotheses). While the number of events is relatively small, most of them are fit with masses greater than 160 GeV/c^2. This is inconsistent with expectation from QCD production of W+4 or more jets, as can be seen from Fig. 61. The uncertainties on the mass obtained from the fit range from 8 to 19 GeV/c^2, reflecting the uncertainties on the measured jet energies. Uncertainties on other quantities, such as the

TABLE XXXIX. Characteristics of the seven candidate events: run and event number, lepton type, tagging algorithm (including sign of lepton for the SLT tagging algorithm), top combination that includes the tagged b, fitted mass and its uncertainty, and the χ^2 from the fit.

Nev	Run event	l	b tag	Top w. b tag	Mass (GeV/c^2)	χ^2
1	40 758–44 414	e^+	SVX	$j\ j\ b$	172±11	0.0
2	43 096–47 223	e^-	SVX	$e\ v\ b$	166±11	2.0
3	43 351–266 423	μ^-	SLT (μ^-)	$j\ j\ b$	158±18	6.1
4	45 610–139 604	μ^+	SVX	$j\ j\ b$	180±9	5.0
5	45 705–547 65	e^-	SLT (e^+)	$e\ v\ b$	188±19	0.4
6	45 879–123 158	μ^+	SLT (μ^-), SVX	$j\ j\ b$	169±10	2.2
7	45 880–31 838	e^-	SLT (e^-)	$j\ j\ b$	132±8	1.7

P_T of the top and the invariant mass of the $t\bar{t}$ system, are larger than this because of large uncertainties on the measured value of X, defined in Sec. IX A. Complete kinematic variables for the seven events, both before and after the constrained fitting, are given in Appendix A.

1. Extracting a mass from the b-tagged events

Using the techniques described earlier in this section for the sample of seven events, we estimate $1.4^{+2.0}_{-1.1}$ events to come from background. To extract the top mass, we fit the observed mass distribution of the seven events to the sum of the expected mass distributions of W+jets background and a top quark of mass M_{top}, using a maximum likelihood method. The likelihood function, L, is defined as

$$L = \frac{1}{\sqrt{2\pi}\sigma_b} e^{-(n_b - N_b)^2/2\sigma_b^2} \frac{e^{-(n_s + n_b)}(n_s + n_b)^N}{N!}$$

$$\times \prod_{i=1}^{N} \frac{n_b f_b(m_i) + n_s f_s(m_i, M_{top})}{(n_b + n_s)} ,$$

where n_b and n_s represent the number of background and signal events, respectively, N is the number of observed events (7), N_b is the calculated number of background events (1.4), and σ_b is the calculated background uncertainty, set equal to 1.6 for the Gaussian to approximate the asymmetric errors quoted above. The variable f_s is the normalized top Monte Carlo mass distribution (see, e.g., Fig. 60), and f_b is the normalized W+jet Monte Carlo mass distribution (see Fig. 61). The variable m_i is the top mass that gives the minimum χ^2 for the fit of the ith event.

To find the shape of the likelihood function as a function of M_{top}, we choose a value of M_{top} in the range 140–200 GeV/c^2, maximize the likelihood with respect to n_b and n_s for that M_{top} (note that $n_b + n_s$ is not constrained to be equal to N). The resulting $-\ln L$ for each M_{top} is shown in Fig. 62. We smooth these results by fitting $-\ln L$ to a cubic in M_{top} (to account for asymmetric errors) and find that the smoothed likelihood is maximized at $M_{top} = 174$ GeV/c^2. The vertical error bars reflect the uncertainty on the value of the likelihood due to the finite statistics of the Monte Carlo samples used to estimate f_b and f_s. The uncertainty on M_{top},

found by allowing ln L to decrease by 0.5 units, is 9 GeV/c^2. Folding in the uncertainty due to Monte Carlo statistics we obtain $M_{top} = 174 \pm 10$ GeV/c^2. Since each point of $-\ln L$ in Fig. 62 corresponds to a local minimum in n_b and n_s, the correlated uncertainties in these quantities are included.

At the most likely value of the top mass, the best value of the background fraction, $\alpha = n_b/N$, is found to be $0.16^{+0.16}_{-0.14}$. This agrees well with the estimate of 0.20 (1.4/7.0), though the fit value is, of course, constrained by the Gaussian term in the likelihood function. We have studied alternate ways of dealing with the background fraction. One extreme is to remove the Gaussian constraining term in the likelihood function, equivalent to ignoring our background estimate, and refit for n_b, n_s, and M_{top}. This results in the same value for the top mass and $\alpha = 0^{+0.38}_{-0}$. The other extreme consists of fixing n_b to our estimate of 1.4 and refitting for n_s and M_{top}. This results in a shift of -1.6 GeV/c^2 (0.9%) in M_{top}. We have also replaced the Gaussian term with the more complex function used to calculate the background value of $1.4^{+2.0}_{-1.1}$ events. The result obtained is well within the 1.6 GeV/c^2 shift quoted above.
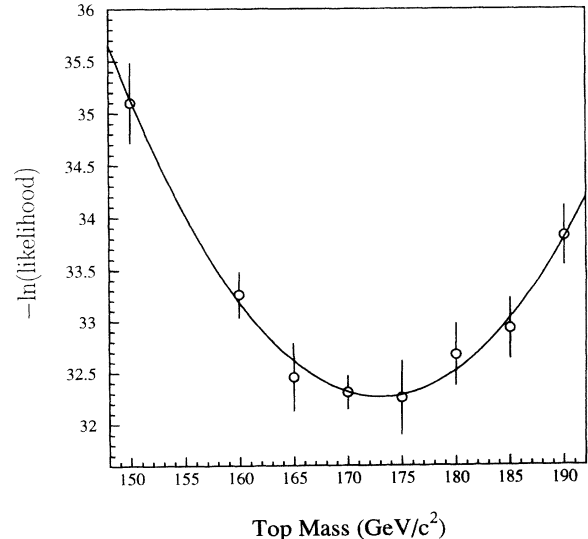

FIG. 62. Likelihood fit of the top mass.

Finally, we test the consistency of the observed mass spectrum (Table XXXIX) with the W+jets background spectrum (Fig. 61) by imposing $n_s = 0$ and removing the Gaussian term from the likelihood function. This hypothesis is 2.3 standard deviations away from the corresponding top+background hypothesis, or about 50 times less likely. The mass distributions of the data and Monte Carlo, with the appropriate fractions of background and signal events for $M_{top} = 175$ GeV/c^2, are shown in Fig. 63.

In order to check that the statistical error for the top mass is consistent with expectations for a sample of seven events, we have generated 1000 samples of seven events each, using the reconstructed Monte Carlo distributions for top and background events. We have taken, at random, two events from the W+jets reconstructed mass distribution (see Fig. 61) and five events from the top Monte Carlo reconstructed mass distribution for $M_{top} = 175$ GeV/c^2 with the one b-tag requirement, and performed the same likelihood fit used on the data.

First we examine the distribution of the mean value of the mass for the Monte Carlo seven event samples. The Gaussian fit gives a mean of 166 GeV/c^2 and $\sigma = 10$ GeV/c^2. The distribution of the rms of the mass fits for the seven event samples has a mean of 25.2 GeV/c^2 with $\sigma = 8.4$ GeV/c^2. These results are to be compared with the results of our experiment shown in Table XXXIX. The mean is $M = 166$ GeV/c^2 with a width of 17.0 GeV/c^2. The experimental value is in agreement with the Monte Carlo result within one standard deviation.

Next we examine the results of the likelihood fits on the 1000 samples. The median of the distribution, shown in Fig. 64, is $M_{top} = 174$ GeV/c^2 with $\sigma = 10$ GeV/c^2. Notice that the mean of the seven event samples differs
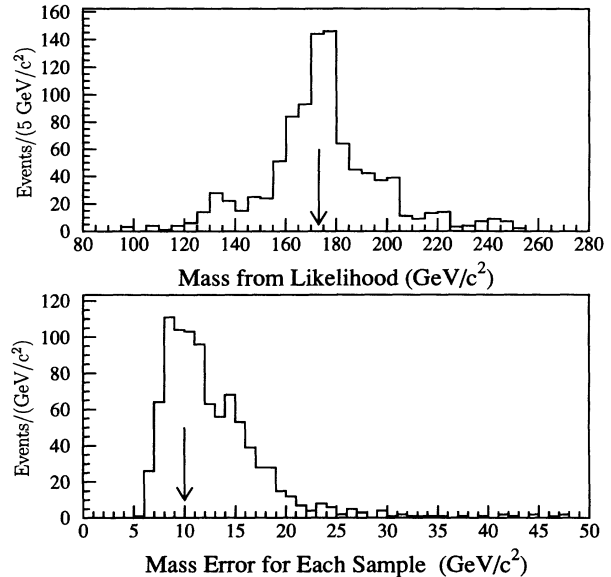
FIG. 64. Results of Monte Carlo simulated events. Top: mass obtained from the likelihood fit of the seven event samples; bottom: distribution of the uncertainty on the mass for each of the seven event samples. The arrows point to the mass and the uncertainty obtained in our experiment.

from the mass value obtained in the likelihood fits as expected: The mean value is shifted to lower masses due to the two background events in the samples. The distributions of the uncertainties obtained for each of the samples (see Fig. 64) shows that the most probable value of the uncertainty is about 10 GeV/c^2, consistent with the value measured from our sample of seven events. Finally, the distribution of $-\ln L$ for the samples also indicates that the value that we obtain in the data is within one standard deviation of the central value for these samples. All this information indicates that our experimental result is in good agreement with expectations from Monte Carlo studies done under the assumption of $t\bar{t}$ production.

2. Study of the events without b-tag information

There are 52 events in the lepton+jets sample that pass all the selection criteria discussed earlier. Of these 52, there are 27 that have a fourth jet with uncorrected $E_T > 8$ GeV and $|\eta| < 2.4$. For this sample the fractional background is expected to be larger than for the seven b-tagged events. The total amount of background in the 27 events is estimated to be $N_b = 13^{+7}_{-9}$ ($\alpha = 0.5^{+0.3}_{-0.4}$) using the Monte Carlo method mentioned previously in this section. The uncertainty on this estimate comes primarily from the uncertainty on the number of tagged events.

A mass fit of these events finds solutions for 26 events, one event fails the $\chi^2 < 10$ requirement. The seven events of Sec. IX C are included here, but the information on which jet is tagged as a b is not included in the fit. The top mass obtained for the 26 events is shown in Fig. 65. There are 13 events with a mass above 160 GeV/c^2, whereas the bin with masses between 140 and 150
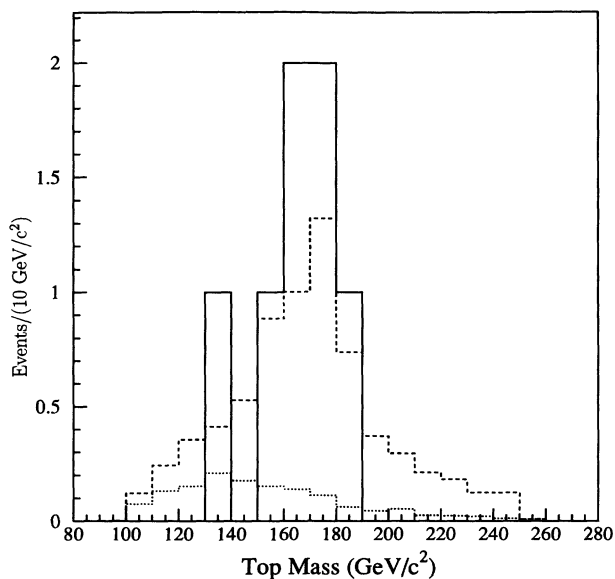

FIG. 63. Top mass distribution for the data (solid histogram) and the background of 1.4 events (dots) obtained from the W+multijets VECBOS events. The dashed histogram represents the sum of 5.6 $t\bar{t}$ Monte Carlo events (from the $M_{top} = 175$ GeV/c^2 distribution) plus 1.4 background events.
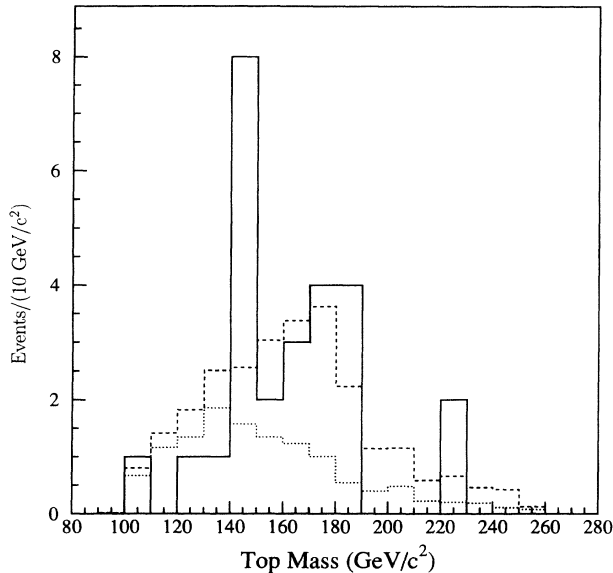
FIG. 65. Top mass distribution for 26 events in the $W+3$ or more jet sample (solid histogram) and the background of 13 events (dots), obtained from the VECBOS $W+4$ jets Monte Carlo distributions. The dashed histogram represents the sum of 13 $t\bar{t}$ Monte Carlo events for $M_t = 175$ GeV/c^2 plus the 13 background events.

TABLE XL. Systematic uncertainties in the top mass measurement.

Systematic uncertainties	(%)
(a) Jet energy scale (detector effects)	1.8
(b) Gluon radiation effects on parton energy	4.4
(c) Different backgrounds	$^{+5.3}_{-4.4}$
(d) Effects due to tagging algorithms	1.4
(e) Different likelihood fits	1.1

GeV/c^2 has eight events. We assume the mass combinations in the (140–150)-GeV/c^2 bin represent a statistical fluctuation, since their width is narrower than expected for a top signal. Using the same Monte Carlo technique discussed in the previous section, in 1000 samples of 26 events (13 events from the top Monte Carlo events and 13 events from background), we find that 5.4% of them have one bin with eight or more events.

We have performed on these events the same likelihood analysis that was described in Sec. IX C 1. For the top mass distributions from Monte Carlo simulation, we use those obtained without the requirement of a b tag in the final fit. For the $W+$multijet background we use the distribution of Fig. 61, as before. We find a value for M_{top} of 167 ± 10 GeV/c^2 for a fit without constraining the background and of 172 ± 11 GeV/c^2 for a fit with the background fraction fixed at 50%. These values are consistent with those obtained with the tagged sample.

3. Systematic errors on the mass determination

Systematic effects in the estimation of the top mass arise from uncertainties that can be categorized as follows: (1) Uncertainties in the parton-energy assignment, (2) uncertainties in the background shapes, (3) systematic shifts of the E_T spectra of signal and background due to possible systematic shifts introduced by the SVX and SLT tagging criteria, and (4) uncertainties due to the likelihood method used. The uncertainties from these sources are summarized in Table XL.

The uncertainty on the parton-energy assignment contains several contributions: The absolute energy scale of the calorimeter, and the relative energy scale of the plug

to the central calorimeter (see Sec. III D). The absolute energy-scale uncertainty varies from $\pm 10\%$ at 8 GeV to $\pm 3\%$ at 100 GeV. The relative energy scale is known to 2%. By reconstructing Monte Carlo events after shifting the calorimeter energy scale by these amounts we determine the uncertainty on the top mass from this source to be 1.8%. Apart from detector effects, there is an uncertainty due to the assignment of energies to partons in the presence of gluon radiation, as discussed in Sec. III D. Here we treat this effect as an independent 10% uncertainty, which leads to a 4.4% uncertainty in the top mass determination. As a further check of the effects of gluon radiation, we have compared the results obtained using both HERWIG and ISAJET Monte Carlo generators. When we apply our procedure to a sample of ISAJET $t\bar{t}$ events the reconstructed mass is 0.5% different than the input 170 GeV/c^2 top mass. This is much smaller than the 4.4% uncertainty due to gluon radiation.

To study the systematic uncertainty associated with the shape of the background we have used events generated with VECBOS and used different forms of fragmentation and evolution by using either ISAJET or HERWIG. Our standard Monte Carlo sample has events obtained with the $W+3$ jets VECBOS matrix element followed by the HERWIG parton shower Monte Carlo program. This procedure provides the fourth jet in the event. We also use the $W+4$ jets VECBOS matrix element followed by HERWIG. Finally, we use a flat background. The masses that the likelihood fit finds with these four types of background agree within 1.6 GeV/c^2 (0.9%). However, a substantial fraction of the background originates from processes for which we have not modeled the mass distribution (see Tables XXI and XXIV in Sec. V). Since this background shape is an unknown at this time, we have to exercise caution in the interpretation of these results. A conservative approach is to assume that the background events are randomly distributed in mass. Therefore, we eliminate two random events from the sample of seven, calculate the mean of the remaining five events and take the maximum spread of the averages as a systematic uncertainty. This procedure gives a systematic error of $+5.2\%$ and -4.3%, which added in quadrature with the 0.9% from the known background variation gives the systematic error shown in row (c) of Table XL.

The tagging algorithms may introduce a bias in the E_T of the tagged b jets, which can alter the reconstructed top mass distribution in several ways: (a) The SLT- and SVX-tagged b jets may produce shifts in the reconstructed mass, (b) we may mistag a non-b jet as a b jet in a real top event, and (c) the $W+$jets background events may be

falsely tagged (mistagged) and alter the background shape. We have studied cases (a) and (b) with the top Monte Carlo data at $M_{\text{top}} = 170$ GeV/c^2 and found a variation on the top mass of 1.4%. To study (c) we have applied our mistag probability functions to the W+jets background and obtained a new shape which resulted in a change of the mass obtained by the likelihood fit by <0.1%. The total systematic uncertainty due to these sources is 1.4%.

Finally, there are additional contributions to the uncertainty from the different methods of performing the likelihood procedure (0.9%, see Sec. IX C 1), and from varying the mass range in the likelihood fit (0.7%). Combining these uncertainties in quadrature yields a final value for the top mass of

$$M_{\text{top}} = 174 \pm 10^{+13}_{-12} \text{ GeV}/c^2$$

where the first error is statistical and the second is systematic.

Using the acceptances for a top of mass 174 GeV/c^2 we repeat the calculation described in Sec. VII and find

$$\sigma_{t\bar{t}}(M_{\text{top}} = 174 \text{ GeV}/c^2) = 13.9^{+6.1}_{-4.8} \text{ pb} .$$

This cross section is somewhat higher than the theoretical calculation [10] for the same mass. We address here the mutual compatibility with a χ^2 analysis on our measured mass, our cross section as a function of mass, the theoretical cross section vs mass (see Fig. 44), and their respective uncertainties. We find that the three results are compatible at a confidence level of 13%. We note, however, that the QCD uncertainties on the top cross sections can be larger [59] than those reported in Ref. [10].

X. CONCLUSIONS

The standard model predicts that for top quark masses in excess of ≈ 85 GeV/c^2, $t\bar{t}$ decays should give rise to two W bosons and two b-flavored hadrons. In this paper we have reported on a search for events with ee, $e\mu$, and $\mu\mu$ pairs in association with large $\not{E}_T$ and at least two jets. Such events are expected from $t\bar{t}$ decays in which both W bosons decay leptonically. We observe two events with $0.56^{+0.25}_{-0.13}$ expected from background. In addition, we have reported the results of our search for $t\bar{t}$ using two b-tagging methods in the lepton plus jets mode, in which only one of the W bosons from $t\bar{t}$ decay subsequently decays to $e\nu$ or $\mu\nu$, while the other decays to a pair of quarks. Using secondary vertex information for b tagging, we observe six events with 2.3 ± 0.3 expected from background. With b tagging via the identification of additional leptons that would arise from semileptonic b hadron decays, we observe seven events with 3.1 ± 0.3 expected from background. The background predictions in the lepton plus jets searches come largely from the data, and are expected to be overestimates. The probability that the results in the dilepton and lepton+jets channels combined are due to a fluctuation of the expected backgrounds is estimated to be 0.26%. For a Gaussian distribution this would correspond to a 2.8σ excess. The statistics are too limited to firmly establish the existence

of the top quark.

Some features of the data do *not* support the $t\bar{t}$ hypothesis. We have tested our understanding of heavy-flavor production in association with a vector boson by applying the two b-tagging techniques to Z+multijet events. We find two tagged $Z+3$ or more jet events, both in the four-jet bin, with 0.64 expected. Although statistically limited, the excess of tagged $Z+3$ or more jet events could potentially signal a (non-$t\bar{t}$) source of heavy-flavor production in association with a vector boson, which exceeds our background predictions. It should be noted, however, that higher-statistics checks of b tagging in $W+1$ and 2 jet events are consistent with expectations. In addition, we have studied the consistency of our $t\bar{t}$ cross-section measurement and the expected rate of events from standard W+multijet production. We find that the measured $t\bar{t}$ cross section is large enough to saturate the number of $W+4$ jet events we observe, leaving a 1.5 to 2 standard-deviation deficit for (non-$t\bar{t}$) QCD W production, after accounting for non-W contributions.

Other features of the data *do* support the $t\bar{t}$ hypothesis. One of the dilepton candidate events is tagged by both b-tagging techniques. This, together with the observed excess of tagged W+multijet events from the two lepton plus jets analyses, provides evidence for an excess of both $Wb\bar{b}$ and $WWb\bar{b}$ production, as expected from $t\bar{t}$ decays. Proceeding under the assumption that we are observing $t\bar{t}$ production, a subset of b-tagged $W+4$ jet events can be fit to the standard model $t\bar{t}$ decay hypothesis with two constraints, to yield a top mass for each event. Using a maximum-likelihood technique to find the preferred value of the top mass based on the individual values from the event fits, the top-quark mass is found to be $174 \pm 10^{+13}_{-12}$ GeV/c^2. The likelihood technique prefers the $t\bar{t}$+background hypothesis over the background-only hypothesis by 2.3 standard deviations. Our measured mass under the $t\bar{t}$ hypothesis agrees with the top mass inferred from precision electroweak measurements [7]. The $t\bar{t}$ cross section at the measured mass is calculated to be $13.9^{+6.1}_{-4.8}$ pb. This cross section is somewhat higher than the theoretical calculation for the same mass ($5.1^{+0.8}_{-0.4}$ pb [10]). By performing a simple χ^2 analysis on our measured mass, measured cross section, and the theoretical prediction for the cross section as a function of M_{top}, we find that the three results are compatible at a confidence level of 13%. We have performed a kinematic analysis of the lepton plus jets event sample and shown that it can accommodate the top content implied by our measured cross section. However, systematic uncertainties in this kinematic analysis preclude a quantitative conclusion from it regarding the $t\bar{t}$ hypothesis at this time.

The data presented here give evidence for, but do not firmly establish the existence of, $t\bar{t}$ production in $\bar{p}p$ collisions at $\sqrt{s} = 1.8$ TeV. Work is continuing on kinematic analyses of the present data, and we anticipate an approximate fourfold increase in data from the 1994–1995 run.

APPENDIX A: CHARACTERISTICS OF THE EVENTS FOR MASS FITTING

The details of fit results for each event are given in the tables. For each object in the event (lepton, E_T, four jets, and the additional transverse energy X) we list the momentum vector before and after the fit, the corrected E_T and its error, and the parton-level assignment in the fit. The b-tagged jets are indicated along with the algorithm that gave the tag. We also list the mass of the hadronic W before the fit, and the best-fit top mass and χ^2. Finally, the η of the jets are calculated using the z-vertex position of the event.

TABLE AI. Run 40758, event 44414.

Object	η	Before fit ϕ (rad)	E_T (GeV)	Corr. E_T (GeV)	σ_{E_T} (GeV)	η	After fit; $\chi^2 < 0.1$ ϕ (rad)	E_T (GeV)	Ass't
Electron(+)	0.44	3.63	109.0	106.8	3.8	0.44	3.63	106.9	e^+
E_T		4.69	56.2	86.0		0.98	4.28	86.4	ν_e
Jet 1 (SVX)	−0.24	0.30	74.0	90.3	13.8	−0.24	0.30	89.8	b_j
Jet 2	0.30	1.91	64.1	78.8	10.9	0.30	1.91	79.2	W
Jet 3	0.62	0.80	51.9	66.1	9.5	0.62	0.80	66.9	W
Jet 4	1.46	5.66	20.2	37.7	10.7	1.46	5.66	39.0	b_l
X		2.82	4.4	7.1	5.7		2.81	7.1	X
				$M_W = 79.3$ GeV/c^2			Mass $= 172 \pm 11$ GeV/c^2		

TABLE AII. Run 43096, event 47223.

Object	η	Before fit ϕ (rad)	E_T (GeV)	Corr. E_T (GeV)	σ_{E_T} (GeV)	η	After fit; $\chi^2 = 2.0$ ϕ (rad)	E_T (GeV)	Ass't
Electron(−)	−0.81	0.77	33.1	30.3	1.4	−0.81	0.77	30.3	e^-
E_T		4.55	72.0	73.9		0.08	5.00	56.4	$\overline{\nu}_e$
Jet 1 (SVX)	0.02	0.91	101.4	127.2	18.1	0.02	0.90	105.1	b_l
Jet 2	1.35	2.74	57.2	76.2	12.5	1.35	2.75	80.6	b_j
Jet 3	1.02	4.87	47.4	67.8	9.7	1.02	4.87	70.8	W
Jet 4	2.02	3.53	26.5	37.5	7.2	2.02	3.54	34.9	W
X		2.68	4.9	7.8	5.7		2.77	7.7	X
				$M_W = 82.1$ GeV/c^2			Mass $= 166 \pm 11$ GeV/c^2		

TABLE AIII. Run 43351, event 266423.

Object	η	Before fit ϕ (rad)	E_T (GeV)	Corr. E_T (GeV)	σ_{E_T} (GeV)	η	After fit; $\chi^2 = 6.1$ ϕ (rad)	E_T (GeV)	Ass't
Muon(−)	−0.07	6.24	24.1	24.6	1.1	−0.07	6.24	24.3	μ^-
E_T		2.39	68.2	78.6		0.55	2.29	70.1	$\overline{\nu}_\mu$
Jet 1	1.18	5.68	99.8	132.8	17.8	1.23	5.68	126.4	W
Jet 2	−0.18	3.07	68.8	86.1	13.4	−0.18	3.07	103.9	b_l
Jet 3	0.23	5.56	22.0	33.1	6.9	0.18	5.55	41.2	W
Jet 4 (SLT)	0.38	1.67	11.9	36.3	10.0	0.38	1.67	28.0	b_j
X		1.84	8.6	13.7	8.4		2.01	14.8	X
				$M_W = 66.1$ GeV/c^2			Mass $= 158 \pm 18$ GeV/c^2		

TABLE AIV. Run 45 610, event 139 604.

Object	η	Before fit ϕ (rad)	E_T (GeV)	Corr. E_T (GeV)	σ_{E_T} (GeV)	η	After fit; $\chi^2=5.0$ ϕ (rad)	E_T (GeV)	Ass't
Muon(+)	−0.18	0.21	54.3	53.5	5.1	−0.19	0.21	53.5	μ^+
$\not{E}_T$		2.53	27.7	34.6		−1.32	1.40	45.2	ν_μ
Jet 1 (SVX)	−0.70	1.42	58.9	77.3	12.6	−0.70	1.42	79.0	b_j
Jet 2	−0.90	4.52	50.9	72.4	12.2	−0.90	4.52	70.7	b_l
Jet 3	−1.51	4.80	27.0	36.2	7.1	−1.52	4.81	45.9	W
Jet 4	0.07	3.58	10.8	21.3	5.7	0.09	3.57	30.7	W
X		3.32	22.3	35.7	8.8		3.31	35.6	X

$$M_W=58.2 \text{ GeV}/c^2 \qquad \text{Mass}=180\pm9 \text{ GeV}/c^2$$

TABLE AV. Run 45 705, event 54 765.

Object	η	Before fit ϕ (rad)	E_T (GeV)	Corr. E_T (GeV)	σ_{E_T} (GeV)	η	After fit; $\chi^2=0.4$ ϕ (rad)	E_T (GeV)	Ass't
Electron(−)	0.70	1.35	52.6	55.8	2.3	0.70	1.35	55.8	e^-
$\not{E}_T$		0.23	57.9	74.9		1.69	0.58	71.4	$\bar{\nu}_e$
Jet 1	0.81	3.73	74.0	90.0	12.2	0.80	3.72	86.5	W
Jet 2	−0.22	3.06	36.6	51.4	8.2	−0.22	3.07	47.9	W
Jet 3 (SLT)	0.68	4.98	33.9	57.0	13.2	0.68	4.98	60.1	b_l
Jet 4	1.94	6.00	17.4	33.3	10.3	1.95	6.00	31.0	b_j
X		1.43	10.7	17.2	7.2		1.42	17.0	X

$$M_W=85.8 \text{ GeV}/c^2 \qquad \text{Mass}=188\pm19 \text{ GeV}/c^2$$

TABLE AVI. Run 45 879, event 123 158.

Object	η	Before fit ϕ (rad)	E_T (GeV)	Corr. E_T (GeV)	σ_{E_T} (GeV)	η	After fit; $\chi^2=2.2$ ϕ (rad)	E_T (GeV)	Ass't
Muon(+)	−0.21	0.09	53.7	52.8	5.0	−0.21	0.09	47.0	μ^+
$\not{E}_T$		3.34	20.8	29.2		−1.14	2.60	30.2	ν_μ
Jet 1	−1.63	2.79	69.4	80.5	12.9	−1.62	2.78	75.0	b_l
Jet 2 (DBL)	−0.11	5.21	62.1	96.1	22.7	−0.11	5.21	104.8	b_j
Jet 3	0.13	0.66	28.8	42.1	7.5	0.13	0.68	40.4	W
Jet 4	−0.44	3.26	25.9	36.9	7.1	−0.44	3.25	39.7	W
X		1.22	16.2	25.9	6.9		1.27	26.3	X

$$M_W=79.5 \text{ GeV}/c^2 \qquad \text{Mass}=169\pm10 \text{ GeV}/c^2$$

TABLE AVII. Run 45 880, event 31 838.

Object	η	Before fit ϕ (rad)	E_T (GeV)	Corr. E_T (GeV)	σ_{E_T} (GeV)	η	After fit; $\chi^2=1.7$ ϕ (rad)	E_T (GeV)	Ass't
electron(−)	0.16	4.48	27.3	25.8	1.3	0.16	4.48	25.8	e^-
$\not{E}_T$		2.34	68.3	67.9		1.16	2.47	63.6	$\bar{\nu}_e$
Jet 1	−0.20	6.21	84.2	98.3	13.2	−0.20	6.21	91.7	W
Jet 2	1.09	4.27	39.6	60.9	11.6	1.09	4.28	59.3	b_l
Jet 3 (SLT)	0.38	1.14	20.8	43.3	11.9	0.38	1.15	45.1	b_j
Jet 4	−0.59	3.70	15.9	26.0	6.3	−0.59	3.70	18.7	W
X		2.31	12.4	19.8	8.9		2.30	20.0	X

$$M_W=98.1 \text{ GeV}/c^2 \qquad \text{Mass}=132\pm8 \text{ GeV}/c^2$$

[1] S. L. Glashow, Nucl. Phys. **22**, 579 (1961); S. Weinberg, Phys. Rev. Lett. **19**, 1264 (1967); A. Salam, in *Elementary Particle Theory: Relativistic Groups and Analyticity (Nobel Symposium No. 8)*, edited by N. Svartholm (Almqvist and Wiksell, Stockholm, 1968), p. 367.

[2] S. L. Glashow, J. Illiopoulos, and L. Maiani, Phys. Rev. D **2**, 1285 (1970); M. Kobayashi and M. Maskawa, Prog. Theor. Phys. **49**, 652 (1973).

[3] F. Abe *et al.*, Phys. Rev. Lett. **68**, 447 (1992); F. Abe *et al.*, Phys. Rev. D **45**, 3921 (1992).

[4] S. Abachi *et al.*, Phys. Rev. Lett. **72**, 2138 (1994).

[5] F. Abe *et al.*, Phys. Rev. Lett. **73**, 220 (1994).

[6] J. Alitti *et al.*, Phys. Lett. B **277**, 194 (1992).

[7] LEP Electroweak Working Group, B. Pietrzyk, Laboratoire de Physique des Particules Report No. LAPP-EXP-94.07, 1994 (unpublished).

[8] P. Nason, S. Dawson, and R. K. Ellis, Nucl. Phys. **B303**, 607 (1988); W. Beenakker, H. Kuijf, W. L. van Neerven, and J. Smith, Phys. Rev. D **40**, 54 (1989); G. Altarelli, M. Diemoz, G. Martinelli, and P. Nason, Nucl. Phys. **B308**, 724 (1988).

[9] E. Laenen, J. Smith, and W. L. van Neerven, Nucl. Phys. **B369**, 543 (1992).

[10] E. Laenen, J. Smith, and W. L. van Neerven, Phys. Lett. B **321**, 254 (1994).

[11] R. K. Ellis and S. Parke, Phys. Rev. D **46**, 3785 (1992); D. O. Carlson and C.-P. Yuan, Phys. Lett. B **306**, 386 (1993).

[12] J. M. Benlloch, N. Wainer, and W. T. Giele, Phys. Rev. D **48**, 5226 (1993); F. Abe *et al.*, Fermilab Report No. Fermilab-Conf-94/152-E, 1994.

[13] M. L. Mangano, Nucl. Phys. **B405**, 536 (1993).

[14] F. Abe *et al.*, Nucl. Instrum. Methods Phys. Res. A **271**, 387 (1988).

[15] F. Abe *et al.*, Fermilab Report No. Fermilab-Pub-94/024-E, 1994 (unpublished).

[16] Pseudorapidity, η, is defined as $\eta = -\ln[\tan(\theta/2)]$ with θ measured assuming a z-vertex position of zero unless otherwise noted.

[17] F. Abe *et al.*, Phys. Rev. D **44**, 29 (1991).

[18] F. Abe *et al.*, Phys. Rev. D (to be published); *ibid.* (to be published); *ibid.* (to be published).

[19] F. Abe *et al.*, Phys. Rev. D **45**, 1448 (1992).

[20] F. Abe *et al.*, Phys. Rev. D **47**, 4857 (1993).

[21] F. Abe *et al.*, Phys. Rev. Lett. **70**, 1376 (1993).

[22] F. Abe *et al.*, Phys. Rev. D **43**, 2070 (1991).

[23] F. Paige and S. D. Protopopescu, BNL Report No. 38034, 1986 (unpublished).

[24] P. Avery, K. Read, and G. Trahern, Cornell Internal Note CSN-212, 1985 (unpublished).

[25] G. Marchesini and B. R. Webber, Nucl. Phys. **B310**, 461 (1988); G. Marchesini *et al.*, Comput. Phys. Commun. **67**, 465 (1992).

[26] F. A. Berends, W. T. Giele, H. Kuijf, and B. Tausk, Nucl. Phys. **B357**, 32 (1991).

[27] R. Field and R. Feynman, Nucl. Phys. **B136**, 1 (1978).

[28] J. Benlloch, in *The Fermilab Meeting*, Proceedings of the Division of Particles and Fields of the APS, Batavia, Illinois, edited by C. H. Albright *et al.* (World Scientific, Singapore, 1993), p. 1091.

[29] J. Ohnemus *et al.*, Phys. Rev. D **44**, 1403 (1991); S. Frixione, Nucl. Phys. **B410**, 280 (1993).

[30] J. Gunion and Z. Kunszt, Phys. Lett. **161B**, 333 (1985); R. Kleiss and W. J. Stirling, Nucl. Phys. **B262**, 235 (1985); K.

Hagiwara and D. Zeppenfeld, *ibid.* **B313**, 560 (1989); F. A. Berends, W. T. Giele, and H. Kuijf, *ibid.* **B321**, 39 (1989); F. A. Berends *et al.*, *ibid.* **B357**, 32 (1991).

[31] F. Abe *et al.*, Phys. Rev. Lett. **67**, 3351 (1991).

[32] J. Ohnemus, Phys. Rev. D **44**, 3477 (1991); S. Frixione, P. Nason, and G. Ridolfi, Nucl. Phys. **B383**, 3 (1992).

[33] B. Mele, P. Nason, and G. Ridolfi, Nucl. Phys. **B357**, 409 (1991); J. Ohnemus, Phys. Rev. D **43**, 3626 (1991).

[34] F. Abe *et al.*, Phys. Rev. D **45**, 3921 (1992).

[35] F. Abe *et al.*, Phys. Rev. Lett. **70**, 4042 (1993).

[36] F. Abe *et al.*, Phys. Rev. Lett. **69**, 28 (1992).

[37] G. Watts, Ph.D. thesis, University of Rochester, 1994.

[38] D. Buskulic *et al.*, Phys. Lett. B **313**, 535 (1993).

[39] F. Abe *et al.*, Phys. Rev. Lett. **71**, 2296 (1993).

[40] S. Dell'Agnello, Ph.D. thesis, University of Pisa, 1993.

[41] F. Abe *et al.*, Phys. Rev. Lett. **71**, 3421 (1993).

[42] W. Venus, in *Lepton and Photon Interactions*, Proceedings of the XVI International Symposium, Ithaca, New York, 1993, edited by P. Drell and D. Rubin (AIP, New York, 1994).

[43] M. L. Mangano and P. Nason, Phys. Lett. B **285**, 160 (1992); A. H. Mueller and P. Nason, Nucl. Phys. **B266**, 265 (1986).

[44] These estimates are derived using the next-to-leading order calculation described in M. L. Mangano, P. Nason, and G. Ridolfi, Nucl. Phys. **B373**, 295 (1992).

[45] U. Baur *et al.*, Phys. Lett. **318B**, 544 (1993).

[46] H. Plothow-Besch, Comp. Phys. Commun. **75**, 396 (1993); J. Botts *et al.*, Phys. Lett. B **304**, 159 (1993); A. D. Martin, W. J. Stirling, and R. G. Roberts, Phys. Rev. D **47**, 867 (1993).

[47] F. Abe *et al.*, Phys. Rev. Lett. **68**, 1104 (1992).

[48] I. Hinchliffe, "Papageno Parton Level Monte Carlo," Argonne National Laboratory, 1993 (unpublished); B. van Eijk and R. Kleiss, in *Proceedings of the ECFA Large Hadron Collider Workshop*, Aachen, Germany, 1990, edited by G. Jarlskog and D. Rein (CERN Report No. 90-10, Geneva, Switzerland, 1990), Vol. II, p. 183.

[49] P. Agraval, S. D. Ellis, and W.-S. Hou, Phys. Lett. B **256**, 289 (1991); W.-S. Hou and R. G. Stuart, Nucl. Phys. **B349**, 91 (1991).

[50] A. Stange, W. Marciano, and S. Willenbrock, Phys. Rev. D **49**, 1354 (1994).

[51] C. T. Hill and S. J. Parke, Phys. Rev. D **49**, 4454 (1994).

[52] E. Eichten and K. Lane, Phys. Lett. B **327**, 129 (1994).

[53] J. Gunion *et al.*, *The Higgs Hunter's Guide* (Addison-Wesley, New York, 1990); F. Abe *et al.*, Phys. Rev. Lett. **72**, 1977 (1994); F. Abe *et al.*, Phys. Rev. D **44**, 29 (1991); J. Alitti *et al.*, Phys. Lett. B **276**, 354 (1991); C. Albajar *et al.*, *ibid.* **253**, 503 (1991).

[54] A. D. Martin, W. J. Stirling, and R. G. Roberts, Phys. Rev. D **47**, 867 (1993).

[55] M. Cobal, H. Grassmann, and S. Leone, Nuovo Cimento **107A**, 75 (1994).

[56] O. Dahl, T. Day, F. Solmitz, and N. Gould, Lawrence Berkeley Lab, Group A Programming Note P-126, 1968 (unpublished).

[57] Review of Particle Properties, K. Hikasa *et al.*, Phys. Rev. D **45**, S1 (1992).

[58] K. Kondo, J. Phys. Soc. Jpn. **60**, 836 (1991); G. R. Goldstein, K. Sliwa, and R. H. Dalitz, Phys. Rev. D **47**, 967 (1993).
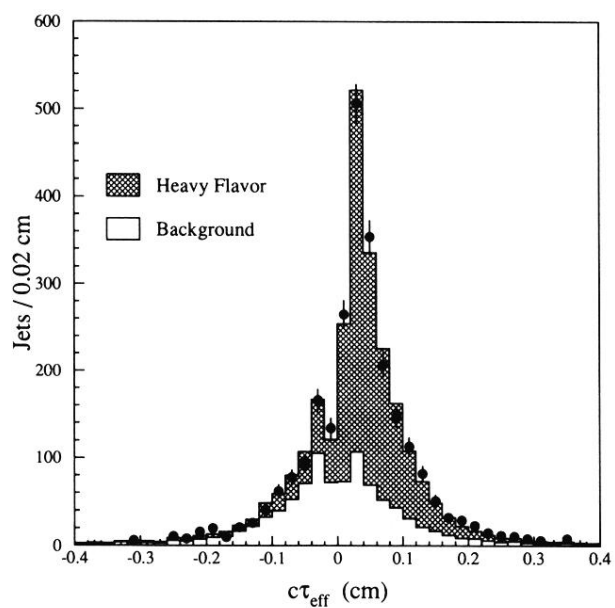
[59] R. K. Ellis, Phys. Lett. B **259**, 492 (1991).

FIG. 23. The $c\tau_{\mathrm{eff}}$ distribution for jets with a secondary vertex in the sample collected with a 50-GeV jet trigger (points). The distribution is fit to a combination of heavy flavor (b decays and c decays; shaded) and background (histogram). The fit gives the relative fractions of positive L_{xy} tags from heavy flavor and background to be approximately 75% and 25%, respectively.
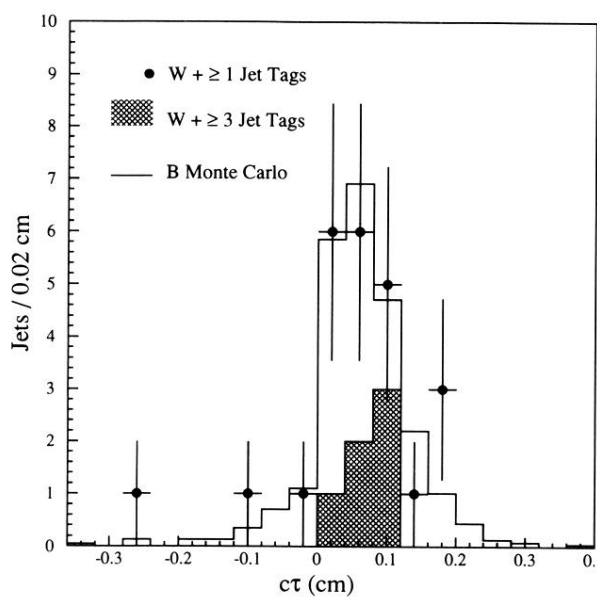
FIG. 29. The $c\tau_{\mathrm{eff}}$ distribution for jets with a secondary vertex in the $W+$jets data (points with errors) compared to b quark jets from Monte Carlo $t\bar{t}$ events (histogram normalized to data). The shaded histogram is the $W+\geq 3$ jets tags in the data. A $W+2$ jet event with a $c\tau_{\mathrm{eff}}=1.2$ cm and a $W+1$ jet event with a $c\tau_{\mathrm{eff}}=-0.41$ cm are not shown.
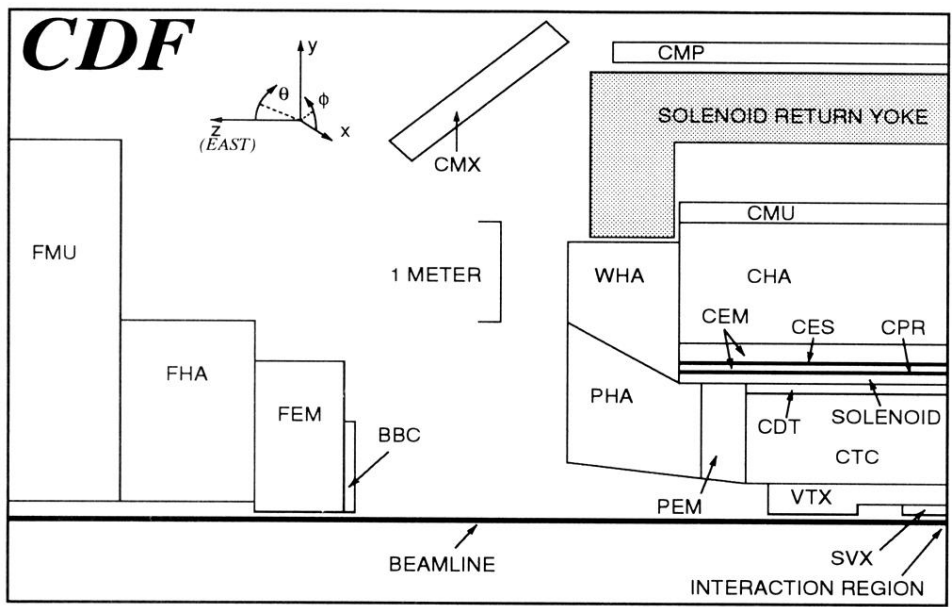
FIG. 3. A side-view cross section of the CDF detector. The detector is forward-backward symmetric about the interaction region, which is at the lower-right corner of the figure. See text for detector component definitions.
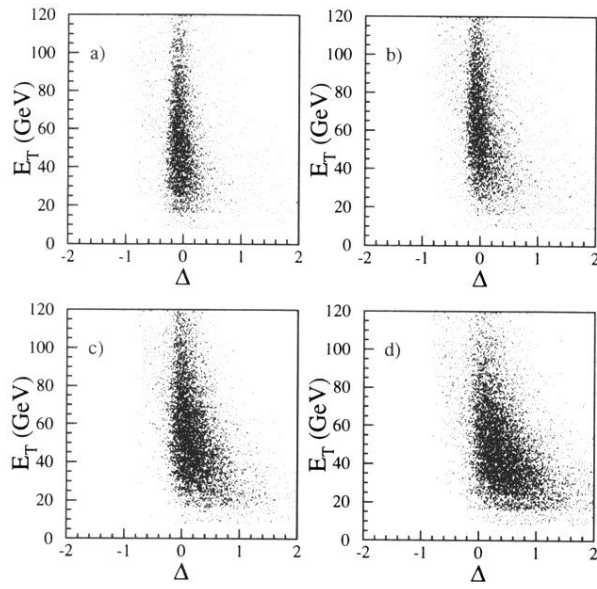
FIG. 57. Scatter plots of jet E_T corrected with standard jet corrections vs Δ for the four jet types: (a) light quarks, (b) generic b jets, (c) $b \rightarrow e\nu X$ jets, and (d) $b \rightarrow \mu\nu X$: $\Delta = [P_T(\text{parton}) - E_T(\text{jet})]/E_T(\text{jet})$. The Monte Carlo events have been generated with HERWIG at $M_{\text{top}} = 170$ GeV/c^2.